TAMPERE UNIVERSITY OF TECHNOLOGY

ANA MARÍA SOTO DE LA CRUZ

PRESSURE SENSORS FOR PRESSURE GARMENT APPLICATION

Master of Science Thesis

Examiner: Professor Jukka Lekkala
Examiner and topic approved by the Faculty Council of the Faculty of Science and Enviromental Engineering meeting on 4 May 2011

ABSTRACT

TAMPERE UNIVERSITY OF TECHNOLOGY
Master of Science (Technology) in Science and Bioengineering
SOTO DE LA CRUZ, ANA MARÍA : Pressure Sensors for Pressure Garment Application
Master of Science Thesis, 86 pages, 8 Appendix pages
December 2011
Major: Biomeasurements
Examiner: Professor Jukka Lekkala
Instructor: Timo Salpavaara, MSc.
Keywords: Pressure sensor, pressure garments, passive resonance sensor, capacitive sensor

Pressure garments, also called compression garments, are used for the treatment of hypertrophic scars, venous insufficiency, lymphoedema and other illnesses. The beneficial influence of pressure on the treatment of hypertrophic scars has not been scientifically proven. For other illnesses such as venous diseases, there exists an international disagreement on the optimal level of pressure to be applied in order to obtain beneficial results. The reason for these is the difficulties in measuring the interface pressure between the pressure garment and the skin.

This work focused in the enhancement and study of the structure of an inductively coupled pressure sensor for pressure garment application. A three-dimensional model of the sensor using finite element analysis (FEA) was constructed. The model served to study the behavior of the sensor with different membrane dimensions and to study the influence of the mechanical properties of the materials in the sensor results. Three different membrane designs were developed and constructed. The sensor prototypes were tested and they behaved similarly to the constructed model. A bossed membrane made of transparency film was found to have a linear behavior and a measurement range from 0 to 65 mmHg. These results lead to future reduction in size and enhancement of the behavior of the inductively coupled pressure sensor.

PREFACE

This thesis work was related to the KUMO project (Kompressiopaineen ja sen kudosvaikutusten monitorointi), and was funded by the Industrial Research Fund at Tampere University of Technology. The work was performed at Tampere University of Technology in The Department of Automation Science and Engineering between November 2010 and December 2011. The thesis work was performed under the supervision of Professor Jukka Lekkala and M.Sc Timo Salpavaara.

I would like to thank Professor Jukka Lekkala for the advice, teaching and guidance received. Also, I am thankful to Timo Salpavaara for his time and guiding.

Finally, I would like to thank Enrique, my family, Luis, Lyly and Poppea for their company, support and love during the development of this work.

Ana María Soto de la Cruz
Tampere, December 2011

Finninmäenkatu 4 H 84
33710 Tampere, FINLAND
+358 466 268 130
ana.sotodelacruz@tut.fi

TABLE OF CONTENTS

ABBREVIATIONS AND NOTATION

α_1,α_2	Electrostriction Constants
α_{ij}	Coefficient of Thermal Expansion Tensor
γ	Shear Strain
Δ	Increment
δ_{ik}	Unit Tensor
ϵ	Normal Strain
ϵ_0	Free Space Permittivity
ϵ_r	Relative Permittivity
ϵ_{ik}	Dielectric Tensor
ϵ_d	Dielectric Constant
θ	Change in Temperature
ν	Poisson's Ratio
ρ	Space Charge Density
σ, s	Stress
$\sigma_{ij}, \mathbf{F}_A, \mathbf{T}^n$	Cauchy Stress Tensor
ω	Diaphragm Deflection
ω_c	Deflection of the Center of the Diaphragm
Ω_d	Gap between electrodes
ω_f	Angular Frequency
$\nabla\cdot$	Divergence Operator
C_{ijkl}	Stiffness Tensor
E	Young's Modulus
$\mathbf{n}$	Unit vector

CMOS	Complementary Metal-Oxide-Semiconductor
CVD	Chemical Vapor Deposition
DC	Direct Current
DRIE	Deep Reactive Ion Etching
EDP	Ethylenediamine Pyrocatechol
FEA	Finite Element Analysis
FEP	Fluorinated Ethylene Propylene Copolymer
LCP	Liquid Crystal Polymer
LIGA	Lithography, Electroplating and Molding
LTCC	Low-temperature Co-fired Ceramic
MEMS	Microelectromechanical Systems
PCB	Printed Circuit Board
PDEs	Partial Differential Equations
PDMS	Polydimethylsiloxane
PTFE	Polytetrafluoroethylene
RAL	Reichsausschuss Für Lieferbedingungen
RF	Radio Frequency
RIE	Reactive Ion Etching
SIGat	Sigvaris Interface-pressure Gauge Advanced Tester
SOI	Silicon On Insulator
UV	Ultraviolet Light

1. INTRODUCTION

This work is related to the KUMO project. The KUMO project aims are to develop an inductively coupled pressure sensor for pressure garment application, investigate the pressure effects on tissues and the associated measurement technologies and to research the behavior of electrode-skin interface when subject to pressure. This thesis work is only focused on the first mentioned project aim, for the enhancement and the study of the structure of the inductively coupled pressure sensor for the pressure garment application.

This work is divided in twelve chapters. After the introduction, Chapter 2 introduces the pressure garments and presents the concept of pressure treatment and its medical applications. In the Chapter 3 is introduced the concept of pressure sensors and types, focusing in capacitive pressure sensors. The silicon based processes and polymers processes used for the manufacturing of capacitive pressure sensors are described in Chapter 4 as well as some polymers materials used for the fabrication of microsensors. In the Chapter 5 the concepts of subdermal and interface pressures are described and commercially available pressure sensors for pressure garments are presented and compared. Chapter 6 introduces passive resonance sensors and presents previous works done with passive resonance pressure sensors. In addition, a comparison between these previous works is presented. In Chapter 7 the simulations models are described and results are presented. The operation principle of the sensor design is explained and the constructed sensors designs are described and presented in Chapter 8. In the Chapter 9 the measurement set up and results for the constructed sensors are showed. In Chapter 10 a comparison between the results of each constructed sensor of each design and a comparison with the model results of each design are presented. Finally, in the Chapter 11 the results are discussed and final conclusions are presented.

2. PRESSURE GARMENT APPLICATIONS

2.1 Pressure garments

Pressure garments, also called compression garments, have been used for the treatment of burn scars, venous insufficiency, lymphoedema and other illnesses, which are mentioned later [1]. Pressure garments are custom-made garments which are elastic and tight fitting and they are used to exert pressure over the skin [1].

Pressure garments are tailor-made to fit the patient and are worn regularly and removed only for washing and personal hygiene [1]. Pressure garments are often made of an elastic fabric containing Lycra [2]. The use of different kinds of Lycra enables the development of fabrics with different degrees of elasticity and thus making it possible to apply different amounts of pressure to the skin [2].

Furthermore, because pressure treatment is used for many conditions, several types of pressure garments exists in order to support and to exert pressure over different parts of the body as shown on Figure 2.1 [1].

Moreover, there is not a common pressure standard for pressure garments internationally, nor in Europe, specifically for lymphatic disorders and venous diseases. In Europe, for example, there are a German and a British standard and in America there is a US standard. The classification of pressure garments in these standards varies as shown on table 2.1.

Table 2.1: *Classification of pressure garments by different standards*

Comparision of pressure classes standards for venous diseases and lymphatic disorders				
Compression class	Compression intensity	Pressure German standard (RAL) (mmHg) [3]	Pressure British standard (mmHg) [4]	Pressure US Standard (mmHg) [5]
I	Low	18 to 21	up to 20	8-15
II	Moderate	23 to 32	21-30	15-20
III	High	34 to 46	31-40	20-30
IV	Very high	49 and higher	41-60	40

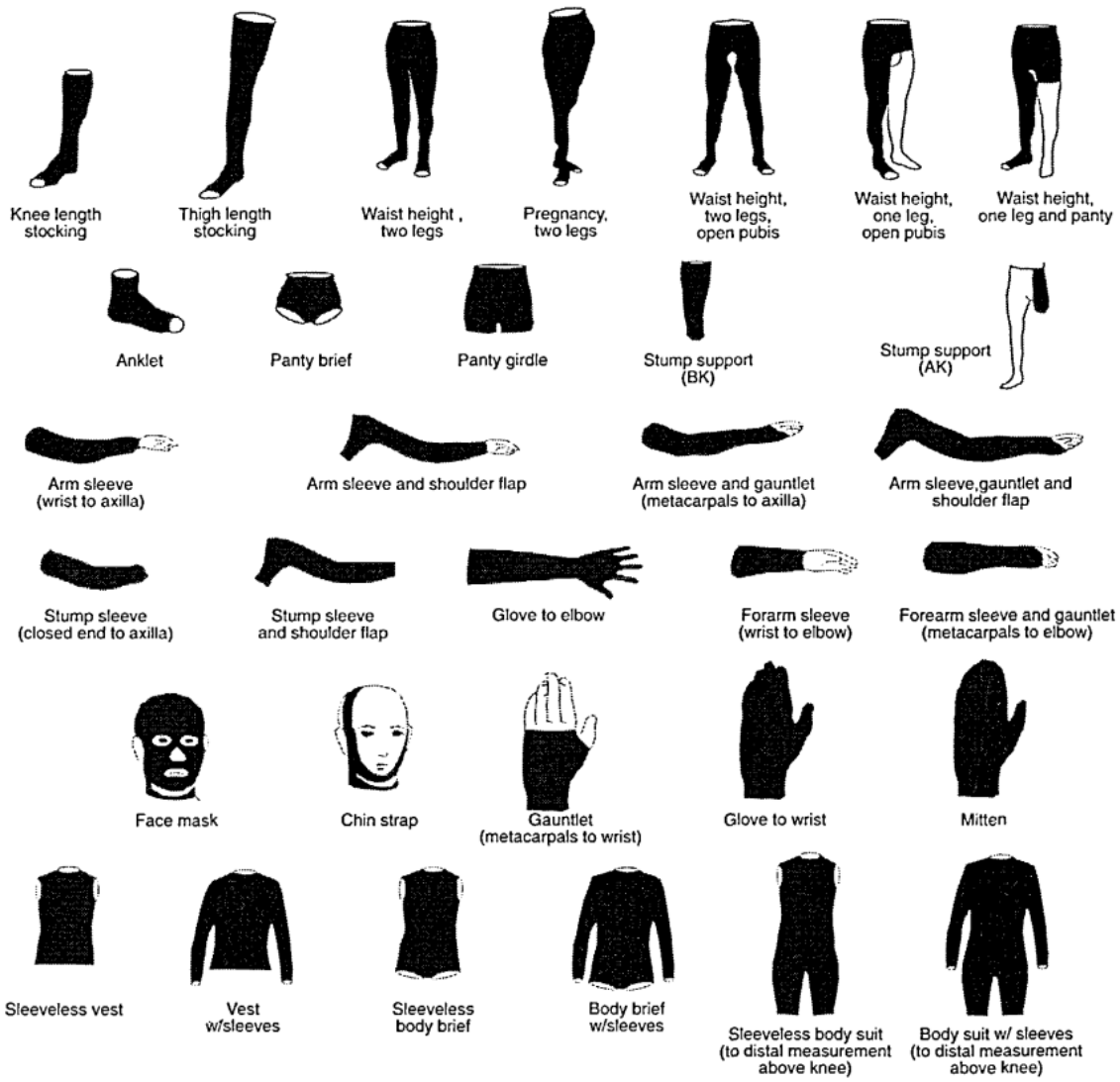

Figure 2.1: *Pressure garment types [1]*

2.2 Pressure treatment

Pressure garments are used for the treatment of hypertrophic scars and prevention of scars on wounds which require more than 10-14 days to heal or injuries requiring grafts [6]. They are also used to treat chronic venous insufficiency, venous ulcers, oedema, deep venous thrombosis, varicose veins [7–10], and to reduce oedema in limbs after amputation [11]. Other applications of pressure garments include the employment of pressure for better cosmetic results after surgery, for softening scars, for the prevention of skin contractures and for the reduction of problems related to itch and skin hypersensitivity [12].

However, the beneficial influence of pressure on the treatment of hypertrophic scars has not been scientifically proven, since only clinical evidence exists [6]. One of the reasons is the difficulty of measuring the pressure produced by the garment [13].

Beneficial evidence has been reported by Thomson in 1974. He studied the favorable effect of compression over hypertrophic scars on 100 patients using bandages and splints. He concluded that the compression and occlusion (blockage of blood vessels) improved the scarring in most of the patients (72 out of 100) [14]. Another study made in 1975 by Isherwood found that the shape and hardness of the place where the pressure is applied affects the amount of pressure exerted by the pressure garment. For that reason is not convenient to rely on the manufacturer's calculations and there is a needed for a method to measure the pressure directly [14]. This suggests that there is a necessity for the development of an accurate method that is able to measure the pressure applied by pressure garments.

Furthermore, it is believed that pressure applied by garments is beneficial for treatment of hypertrophic scars and particularly for burn scars because when pressure is applied to the tissue, the blood supply is limited, consequently, the delivery of oxygen and nutrients to the tissue is reduced. This decreases the production of collagen, promotes collagen lysis and additionally the realignment of collagen bundles in the tissue [6, 15].

For the other applications where pressure garments are used, such as venous diseases and lymphatic disorders there exists an international disagreement on the optimal level of pressure to be applied in order to obtain beneficial results [10]. Compression is used in these diseases to reduce capillary filtration and enhance the reabsorption of interstitial fluid [4]. In addition, it also improves the return of venous blood and reduction of lymphatic fluid in tissues [4].

Therefore, quantifying compression in these treatments is desired in order to be able to correlate different results between clinical trials, control the amount of compression applied, determine how much pressure is needed for each application and to prove the benefits of these treatments [16].

3. PRESSURE SENSORS TYPES

Pressure sensors convert force into an electrical signal [17]. As known, pressure is defined as force per unit area. Thus, the principle operation of most of the pressure sensors is that when force is applied to the sensor this causes a change in its geometry. Hence, the amount of deformation can be quantified in order to measure the pressure exerted on the sensor [18].

Nowadays micromachined pressure sensors are very successful because they have applications in different areas such as automotive, industrial and military [19]. Pressure sensors are particularly employed in the biomedical field for example for measuring arterial, intraocular and intracranial pressures [17, 19].

As mentioned above, most pressure sensors in use are made using silicon processing technologies [17] which are used in the fabrication of integrated circuits [20]. These pressure sensors are called microelectromechanical pressure sensors. Microelectromechanical system (MEMS), also called microsystem, has been defined by Gardner [20] as "A device that has a sensing element with a physical dimension on the sub-millimetre ($\leq$100 μm) scale". MEMS pressure sensors offer good solutions for medical applications where the pressures values are very small. These good characteristics are their small size, high repeatability, low hysteresis, low costs and power consumption [17, 19].

The most common transducers used for pressure sensors are the capacitive and piezoresistive. Both methods are diaphragms-based [19] where the deflection of the membrane is transduced into an electrical signal. In industry, the most common type of pressure sensor is the piezoresistive pressure sensor. This is mainly due to their low cost of fabrication, good performance and ease of integration and fabrication [17,19].

Even though they are not so common in industry, capacitive sensors have certain advantages compared to piezoresistor sensors. Capacitive sensors are less sensitive to temperature, are smaller in size and have lower power consumption than piezoresistive sensors [21]. On the other hand, capacitive sensors are non-linear, requiring more complicated electronic interface circuit than piezoresistive sensors [22]. In addition, the circuit interface needs to be placed very close to the sensor chip or be integrated in the sensor to avoid the effects of stray capacitance [22].

Furthermore, a way to categorize pressure sensors is by the reference used to measure pressure. The different references used for measuring pressure are gauge,

differential and absolute or vacuum gauge [17]. The gauge pressure is the pressure measured relative to the atmospheric pressure, differential pressure measures the pressure difference between two points and absolute or vacuum gauge measures the pressure relative to a vacuum [17].

3.1 Piezoresistive sensors

As mentioned above, piezoresistive sensors are the most common kind of pressure sensors mainly due to the simplicity of their interface circuitry and manufacturing processes [19]. However, they are sensitive to temperature, suffer from drift and are not appropriate for measuring small pressure differences accurately due to their low sensitivity [22].

Piezoresistivity is the change in resistivity of a material due to strain. The gauge factor is defined as the ratio of resistance change to dimensional change [19]:

$$GF = \frac{\Delta R/R}{\Delta l/l} = \frac{\Delta R}{\epsilon R}, \tag{3.1}$$

where R is the resistance, l is the length and ϵ is the strain.

Silicon is widely used as a piezoresistive material due to its high gauge factor which is 100 times than of the metal films [17, 19]. Additionally, monocrystalline silicon membranes do not deform permanently and suffer less from hysteresis and fatigue than metal membranes [22].

Usually the piezoresistors are created by ion implantation into silicon and the diaphragm is formed by etching. The sensitivity is determined by the diaphragm thickness, but it does not follow a linear relationship [17]. Normally, the piezoresistors are connected in a Wheatstone bridge configuration to obtain a near linear response [19]. In this configuration, two of the resistors increase with pressure while the other two decrease their resistance [17].

Because piezoresistivity is dependent on temperature,the use of Wheatstone bridge configuration helps to reduce this variation, because the dependence of each resistor cancel each other if all have the same value, as shown in the equation below [19].

$$\Delta V \approx \left(\frac{\Delta R_1 - \Delta R_2 + \Delta R_3 - \Delta R_4}{4R} \right) V_s \tag{3.2}$$

where ΔR is the amount of change of the resistors, R_1 to R_4 are the four resistors forming the bridge with the same value R and Vs is the supply voltage.

3.2 Capacitive sensors

Capacitive pressure sensors are diaphragm based. The diaphragm acts as a movable electrode, the deflection of the electrode produces a change in the value of the

capacitor [19].

The capacitance of the transducer is defined as [19]:

$$C = \frac{\epsilon_0 \epsilon_r A}{d} \tag{3.3}$$

where A is the area of the capacitor, d is the separation between the electrodes, ϵ_0 is the permittivity of the free space and ϵ_r is the relative permittivity.

Even though the change in area of the capacitor would result in a linear response, most of the capacitor sensors use the change in distance between plates to sense pressure [19], one of the reasons is that fabrication and assembly are easier [23]. The plates of the capacitor sensor usually do not move in parallel, this means that only one of the plates is deformed. The model for the value of the capacitor is:

$$C = \int\int \frac{\epsilon_0 \epsilon_r}{d - w} dxdy, \tag{3.4}$$

where ω is a function of x and y which models the diaphragm deflection [19, 23].

To overcome the non linearity of the capacitive pressure sensors, there are different configurations other than the simplest one, which only has one deformable flat diaphragm as one of the electrodes. These are touch mode configuration, sandwich configuration and a configuration with a stiff portion in the diaphragm called boss [19, 22] all these shown in Figure 3.1.

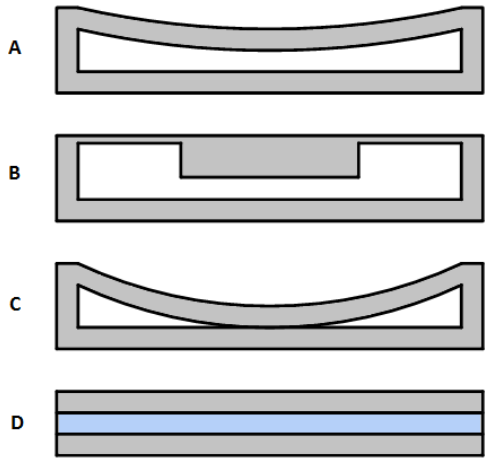

Figure 3.1: *Different configurations of capacitive pressure sensors: A)Flat diaphragm design; B)Bossed diaphragm design; C)Touch mode diaphragm design; D)Sandwich structure design.*

3.2.1 Flat diaphragm design

The change in capacitance caused by a variation of the gap between the electrodes is given by [24]:

$$\frac{\Delta C}{C} = -\frac{\Delta d}{d} \tag{3.5}$$

In this statement it is assumed that the dielectric constant does not change, this is only valid when the air or fluid inside the cavity can be released during deformation. It is assumed that the electrodes are rigid, thus there is not variation in their area [24]. Thus, the bending of the electrodes is not taking into account in this equation.

3.2.2 Bossed diaphragm design

In this configuration, the diaphragm contains a stiff portion called boss, see Figure 3.2, in order to obtain the same deflection in the central part of the diaphragm [25]. This occurs because the thicker portion increase the rigidity in the location of the boss [18]. The membranes with a boss structure suffer from more stress when are deflected, for this reason boss diaphragms are appropriate for sensing small pressures [18].

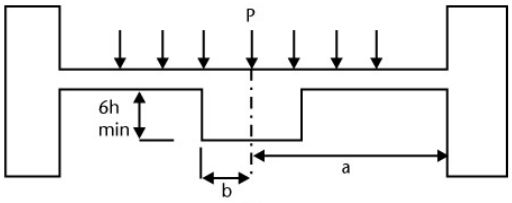

Figure 3.2: *Bossed diaphragm scheme [18]*

In order to achieve a bossed diaphragm behavior, the boss thickness should be in minimum six times thicker than the diaphragm thickness, and the ratio b/a, see Figure 3.2, needs to be greater than 0.15 [18].

When the diaphragm contains a boss the capacitance is given by [22]:

$$C = \frac{\epsilon_0 \epsilon_r A_{boss}}{d - \Delta d} \tag{3.6}$$

Where Δd is the deflection of the boss and A_{boss} is the surface area of the boss. The reciprocal value of the capacitance is linearly dependent on the deflection of the membrane and for small deflections is linearly dependent on the pressure [22]. Nevertheless, in real sensors this linearity is disturbed by a parasitic capacitance C_p as shown in equation 3.7 [22].

$$C = \frac{\epsilon_0 \epsilon_r A_{boss}}{d - \epsilon_0 \epsilon_r d} + C_p \tag{3.7}$$

Ettouhami *et al.* [25] developed a bossed capacitive pressure sensor which consisted of two capacitors. This configuration was chosen in order to obtain a linear and sensitive response. In this configuration, shown in Figure 3.3. , one capacitor acts as the reference and its change in capacitance value is opposite to the change in value of the sense capacitor. This increases the linearity of the sensor response [25].

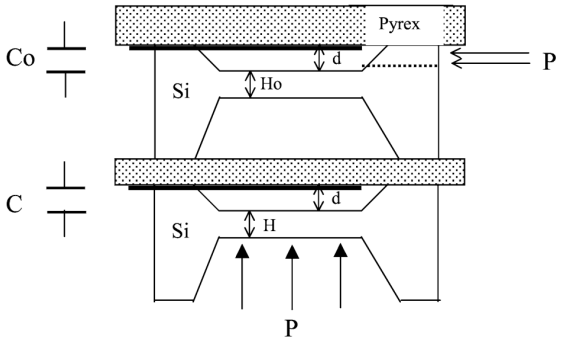

Figure 3.3: *Two capacitor configuration [25]*

The linearity is calculated as follows [25]

$$S_T = \frac{\Delta C}{\Delta P} + \frac{|\Delta C_0|}{\Delta P} = S + S_0 \tag{3.8}$$

where S is the sensitivity of the sense capacitor and S_0 is the sensitivity of the reference capacitor. The slope of the response curve is the sum of the slope of the sense capacitor and reference capacitor. Then, the sum of both sensitivities results in an increment in the final slope that remains almost constant [25].

This group justifies the use of the boss because the sensitivity of the sensor is increased when the diaphragm is closer to the bottom electrode. Additionally, they found that a maximum sensitivity was achieved when the size of the central boss cover 16% to 25% of the diaphragm area. This is when the ratio of the boss edge length to the diaphragm edge length is between 0.4 to 0.5 [25].

From their results, see Figure 3.4, they found that with a ratio value of 2 of the boss thickness to the diaphragm thickness, the sensitivity increase and the response was almost linear with an error of non linearity of 2.7% [25].

3.2.3 Sandwich structure design

Another structure with high sensitivity is the sandwich structure. In this structure the capacitor is formed by three layers, two layers of conductive material forms the electrodes and the third layer located between the electrodes is made of a elastic

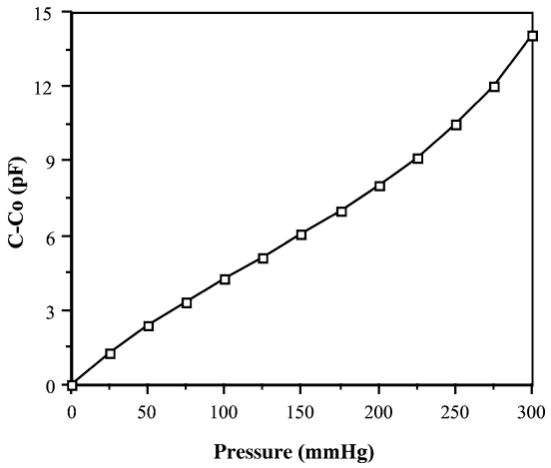

Figure 3.4: *Sensor response with ratio between boss edge and diaphragm edge of 0.4 [25]*

dielectric material [24]. The response of the sensor is determined by the properties of the dielectric material, i.e. Young´s modulus and Poisson´s ratio, and does not depend in the elastic properties of the electrodes and membrane as in the basic capacitor design with a cavity [24]. The dielectric material enhance the value of the capacitance because have higher dielectric constant than air and reduce the effect of parasitic capacitances [24].

Moreover, the design of this structure reduce the difficulties in manufacturing a cavity between electrodes and with this the cost of the sensor is also reduced [24,26]. Additionally, this design is less fragile than capacitor with cavities, because can withstand higher forces without damaging the membrane [24].

The properties of the dielectric material are affected by the humidity, temperature and chemical vapor, for that reason, it is important to select materials which have low sensitivity to these variables [24]. The capacitance change in the sandwich or solid state capacitor structure is given by [24]:

$$\frac{\Delta C}{C} = -\frac{\Delta d}{d} + \frac{\Delta A}{A} + \frac{\Delta \epsilon_d}{\epsilon_d} \tag{3.9}$$

where $\frac{\Delta d}{d}$ is the variation in the gap between the electrodes, $\frac{\Delta A}{A}$ is the variation of the electrodes area and $\frac{\Delta \epsilon_d}{\epsilon_d}$ is the variation of the dielectric constant under the deformation [24].

The term $\frac{\Delta \epsilon_d}{\epsilon_d}$ is the deformation effect on the dielectric constant. This effect is not present in capacitors where the air or liquids can escape from the cavity when the electrodes are deformed [24]. In the sandwich structure, this term cannot be ignored and can in fact increase the sensor response to deformation [24].

When an isotropic dielectric material deforms it becomes anisotropic [24]. The dielectric tensor of the deformed material is [24]

$$\epsilon_{ik} = \epsilon_d \delta_{ik} + \alpha_1 u_{ik} + \alpha_2 u_{kk} \delta_{ik} \tag{3.10}$$

where ϵ_d is the relative dielectric constant of the undeformed material, δ_{ik} is the unit tensor, α_1 (effect of shear deformation on the dielectric properties) and α_2 (effect of volume deformation on the dielectric properties) are the electrostriction constants and u_{ik} is the strain tensor [24].

Chiang *et al.* [27] developed a sensor with sandwich structure intended for neural engineering. In this application a cuff electrode is used to detect neural signals. It is known that the nerve can be damaged if the cuff applies a pressure greater than 20 mmHg. For that reason, the sensor is intended for measuring the interface pressure between the electrode cuff and nerve trunk. Thus, the sensor is placed around the nerve trunk and the electrode cuff around the sensor, see Figure 3.5. In that way, the sensor can measure the interface pressure between the electrode cuff and the nerve trunk and prevent the damage of the nerve trunk.

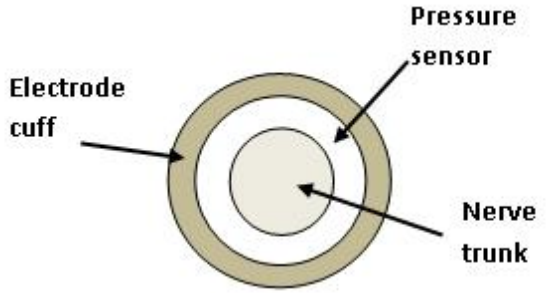

Figure 3.5: *Diagram of the pressure sensor located between the nerve trunk and electrode cuff*

The sensor was fabricated using surface micromachining techniques and the structure consisted of parallel electrodes with insulating layers and a dielectric layer located between the electrodes. The materials used were Polyimide (PI, Durimide 7320) as insulating layers, polydimethylsiloxane (PDMS, Sylgard 184) as dielectric layer and gold for the electrodes [27].

In order to improve the mechanical sensitivity of the sensor, slots between the sensing structure are produced to permit the horizontal expansion of the PDMS due to the pressure applied in the perpendicular direction [27]. The sensor structure is shown in Figure 3.6.

From the in vitro test results they obtained a sensitivity of 0.0452 pF/mmHg from a pressure range between 3 mmHg to 37 mmHg [27].

Another interesting structure was developed by Zhou *et al.* [28]. Their design combined a sandwich structure and a capacitive cavity structure, to enhance the sensitivity of the pressure sensor. The pressure applied to the sandwich structure produces a deflection on the membrane and causes a change in the area of the

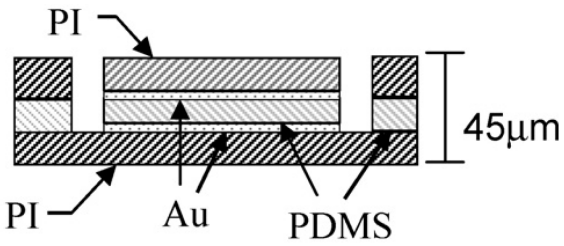

Figure 3.6: *Chiang et. al [27] sandwich pressure sensor*

dielectric layer. The change in area of this layer produces a change on the capacitance value. Further, the bending of the triple layer membrane varies the distance with the electrode on the substrate, producing a change in the capacitive value. These structure is showed on Figure 3.7 (a).

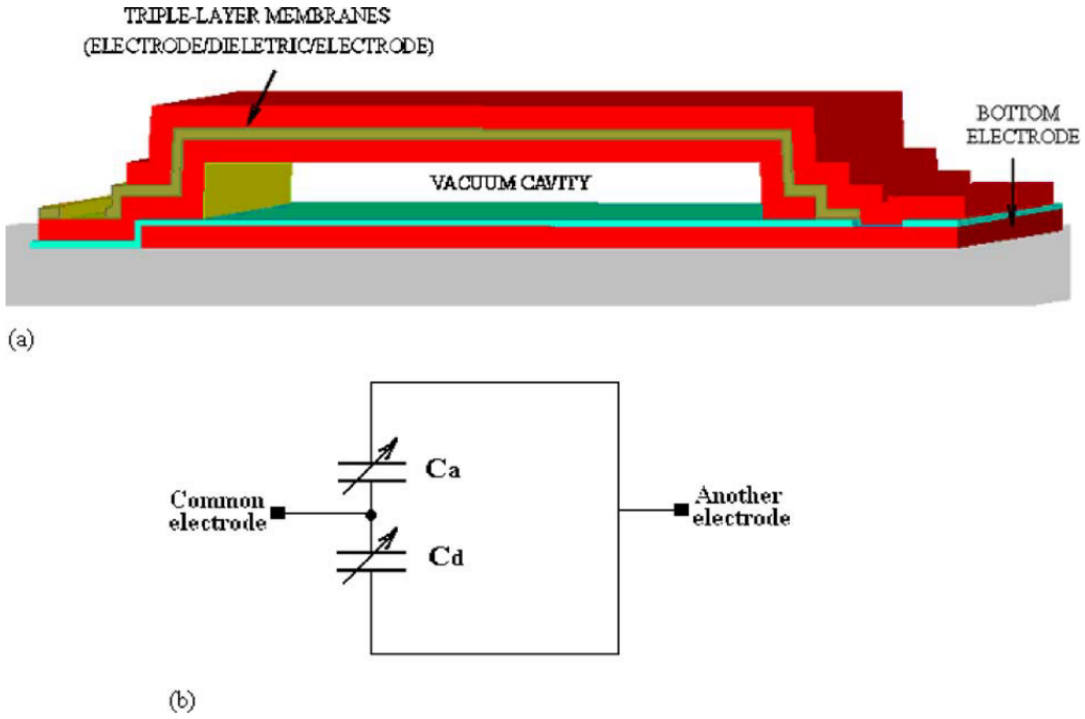

Figure 3.7: *Zhou et al. [28] simplified sandwich structure: a) cross section of the sensor; b) equivalent circuit of the sensor*

Furthermore, their sensor consists of two different capacitors showed in the equivalent circuit on Figure 3.7 (b). Both capacitors share the same electrode, so the capacitive output is the sum of the change in area of the dielectric layer (capacitor C_a) and the change in distance between the triple layer and the bottom electrode (capacitor C_d), improving in this way the sensitivity of the pressure sensor. Also, the sensitivity is greater because it is possible to fabricate a very thin dielectric layer with thickness smaller than the gap of the normal capacitive pressure sensor, then the change in capacitance in the sandwich structure is greater than in the

cavity capacitor when applying the same pressure. Furthermore, the linearity is enhanced due to the greater permittivity of the dielectric material in the sandwich structure [28].

The materials used for this design were for the dielectric layer silicon oxide or silicon nitride and for the electrodes they used doped polysilicon. The composite membrane was form of polysilicon/silicon nitride/polysilicon. For manufacturing they used surface-micromachining technology. In order to achieve a greater capacitive output value, an array of 100 sensors was fabricated. They tested the array of sensors in a chamber with cycled variable pressure range in the range from 0.01 to 0.12 MPa [28]. They found a sensitivity of 40 fF/mmHg , a nonlinearity of 0.32% full scale output and an absolute capacitance value greater than the expected due to the parasitic substrate capacitance [28].

3.2.4 Touch mode diphragm design

In the touch mode configuration the membrane touches the substrate while the pressure increase. In this way the value of the capacitance increase by increasing the surface touching area [29]. This configuration has two modes, the normal mode and the touch mode, a diagram of these modes are showed on Figure 3.8. In the touch mode configuration, there is an insulator layer between the electrodes, so the thickness of this insulator layer is the minimum gap between the electrodes. Then, if this thickness is very small and the dielectric constant of the isolation layer is large, the capacitance would be larger in the area where the membrane touches the insulator layer than that of the untouched area [29]. This increase in touching area is illustrated on Figure 3.9.

The principle of operation of touch mode capacitive pressure sensors was described by Ko and Wang [29]. The typical capacitive-pressure characteristic curve of a capacitive pressure sensor that has normal and touch mode has four different regions, i.e. normal or non-touch, transition or initial touch, linear or operating range and saturation regions, these are shown on Figure 3.10. The first region is the normal region where the sensor behaves as a normal capacitive pressure sensor, in this region the change in capacitance due to pressure applied is small [30]. The next region is called the transition region, it is the region where the diaphragm starts to touch the substrate. In this region the value of capacitance starts to increase [30]. The linear region corresponds to the touch mode or operating range, where the diaphragm touches the substrate. In this region the change in touch area is proportional to the applied pressure. In addition, in this region, the sensitivity is much higher than in normal mode [29]. The last region is the saturation region where the value of the capacitance saturates, so larger pressure values would not cause change in the value of the capacitance [30].

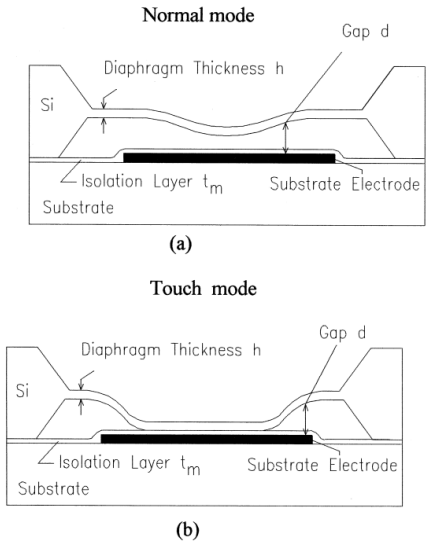

Figure 3.8: *Structure of touch mode capacitive pressure sensor. (a) Normal mode; (b) touch mode [29]*

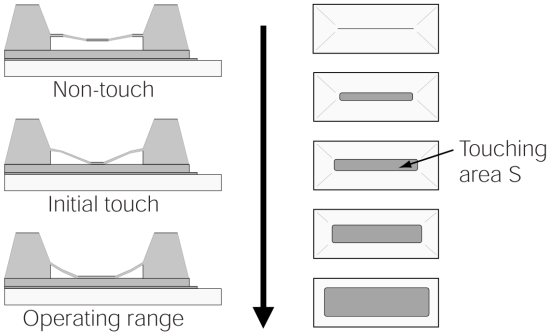

Figure 3.9: *Increase in touch area in touch mode capacitive pressure sensor [30]*

As in the other diaphragm based pressure sensors, the geometry of the diaphragm is closely related to the sensitivity of the sensor. As mentioned before, the circular diaphragm gives the maximum sensitivity because it does not have corners as rectangular and square diaphragm where the stress is larger [29].

Touch point pressure is the pressure needed for the diaphragm to touch the substrate. The material parameters and geometry of the sensor determines the touch point pressure and the sensitivity of the sensor. A small value of touch point pressure gives a great sensitivity, and the sensitivity increases by decreasing the diaphragm thickness [29].

Pedersen *et al.* [31] proposed a design that consisted of several hexagonal membranes inside a circular area as showed on Figure 3.11. These hexagonal structures form an array of capacitors thus, with this design the capacitance value is greater as well as the change in capacitance. Moreover, with higher capacitance values, the effect of parasitic capacitance is reduced. In addition, the pressure range sensed by

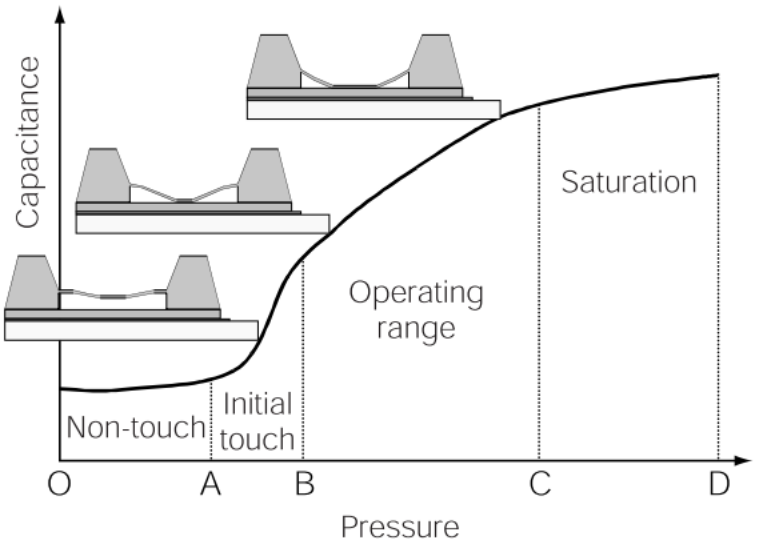

Figure 3.10: *Touch mode characteristic curve [30]*

the sensor can be adjusted by changing the dimension of the hexagonal structures.

The sensor was formed by three layers. The top and lower layers form the electrodes and were made of doped silicon. The intermediate layer was made of silicon dioxide and acted as an insulator. Also, the top layer has an insulation groove etched to form the circular silicon membrane. The sensor was fabricated using fusion bonding of silicon wafers to form the vacuum cavity and to manufacture the hexagonal structure Reactive Ion etch (Surface technology Systems) was used [31].

The sensor was tested by applying pressure using a Druck DPI 520 pressure controller. To measure the output they used two methods. In the first method they measured the capacitance with a HP 4294A Precision Impedance Analyzer and for the second method they converted the capacitance signal into voltage signal by using an AC bridge electronic circuit and measured the signal using a HP 54522A oscilloscope. They applied test pressure in steps of 26 mbar in the range from 250 mbar to 10.9 bar [31].

From the impedance measurements they found a perfect capacitor behavior in the range of frequencies from 100 Hz to 10 MHz, the capacitance value measured at 250 mbar was 137.6 pF and at 10.9 bar was 778.1 pF. This group identified the four different regions of touch mode as shown in Figure 3.12. According to them, the sensor operate in normal mode below 1.5 bar, the transition region was found between 1.5 and 1.9 bar, the touch mode region was identified from 1.9 to 6 bar and finally the saturation region was found above 6 bar. However, it is not clear why the authors chose this range for the saturation region, since according to their data, the capacitance is still changing above 6 bar. Furthermore, they claim that in the saturation region the sensitivity decrease when compared with the touch

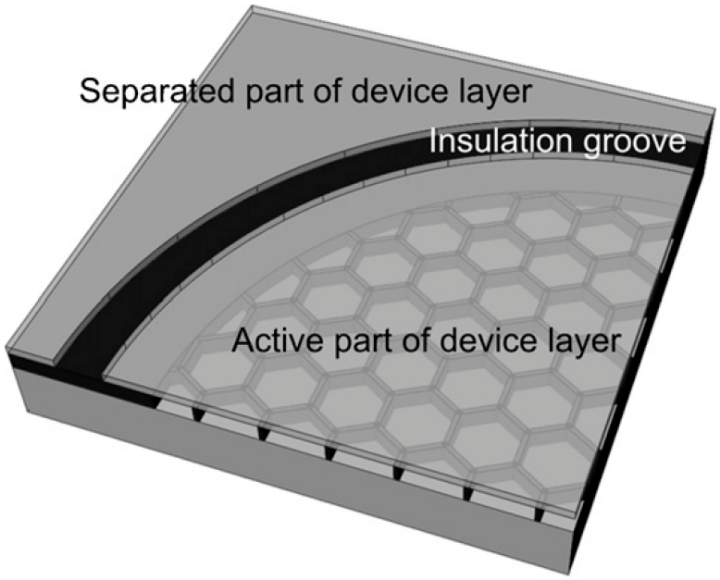

Figure 3.11: *Pedersen et. al [31] sensor schematic. A quarter of the sensor is showed, the thin silicon membrane is illustrated as transparent.*

mode region where the average sensitivity was 76 pF/bar. Further, in the touch mode region the behavior of the sensor was almost linear due to the nearly linear increase of contact area between the electrodes and, the sensitivity in this region is greater than in the normal mode region. In the transition region the sensitivity increase abruptly whereas in the saturation region the sensitivity decreases but is still greater than in the normal mode region [31].

In order to sense small variations in the value of the capacitance, the AC bridge is one of the most used analog circuits, mainly because has several advantages such as high resolution, immunity to stray capacitance, low baseline drift and simplicity on the design of the circuit [31]. They used this circuit to obtain the small variations of capacitance in the region from 1.75 to 2 bar, see Figure 3.12.

They evaluated hysteresis in their sensor by increasing and decreasing the pressure applied. They found that the decreasing pressure curve was higher than the increasing pressure curve, see Figure 3.12. This difference is attributed to adhesion forces between the membrane and the substrate, this adhesion forces tends to maintain the membrane in the higher pressure position, resulting in higher values of capacitance when decreasing the pressure. To avoid this, they applied a DC bias to the sensor, so the electrostatic force is larger than the adhesion forces, decreasing in this way the hysteresis. They found that at higher DC voltages values the hysteresis is smaller than in lower DC voltages. Also, they found that the sensor entered the touch mode region at lower pressures when applying DC bias. These effects are shown on Figure 3.13 [31].

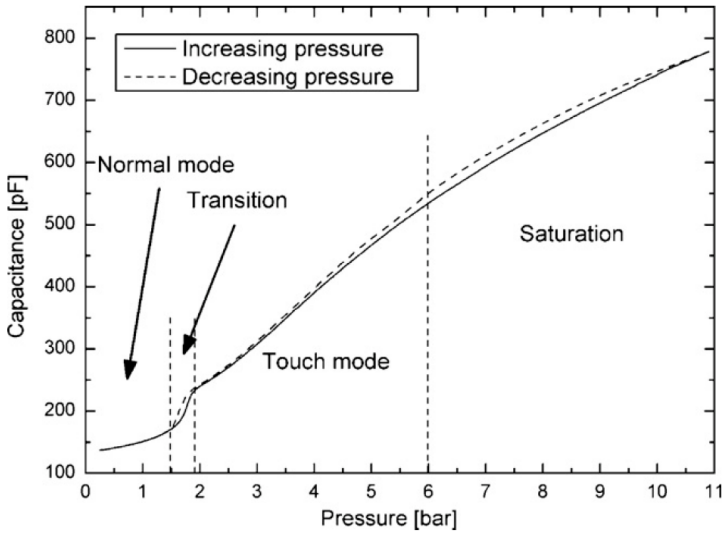

Figure 3.12: *Capacitance as function of pressure [31].*

3.3 Diaphragm mechanics

Most of the pressure sensor devices are based on the deflection of a diaphragm. The relation between the pressure applied to the diaphragm and its displacement can be modeled according to the geometry. Below, square and circular diaphragm mechanics are described [19].

3.3.1 Square diaphragm

The deflection of a square diaphragm can be modeled using the next equation [19]:

$$\Delta P = \frac{Eh^4}{(1-\upsilon^2)a^4}\left[4.20\frac{\omega_c}{h} + 1.58\frac{\omega_c^3}{h^3}\right] \tag{3.11}$$

where υ is the Poisson's ratio, E is the Young's modulus, ΔP is the pressure difference applied to the diaphragm, h and a are the thickness and half of the length of the diaphragm, respectively, and ω_c is the deflection of the center of the diaphragm [19]. In diaphragms with clamped edges the maximum deflection occurs in the center of the diaphragm [29]. The deflection at the center of the diaphragm is linear with deflections values smaller than the thickness. On the other hand, with greater deflections the response to pressure changes in the center of the diaphragm is of the third order [19].

3.3.2 Circular diaphragm

The model for the deflection of a circular diaphragm is [19]:

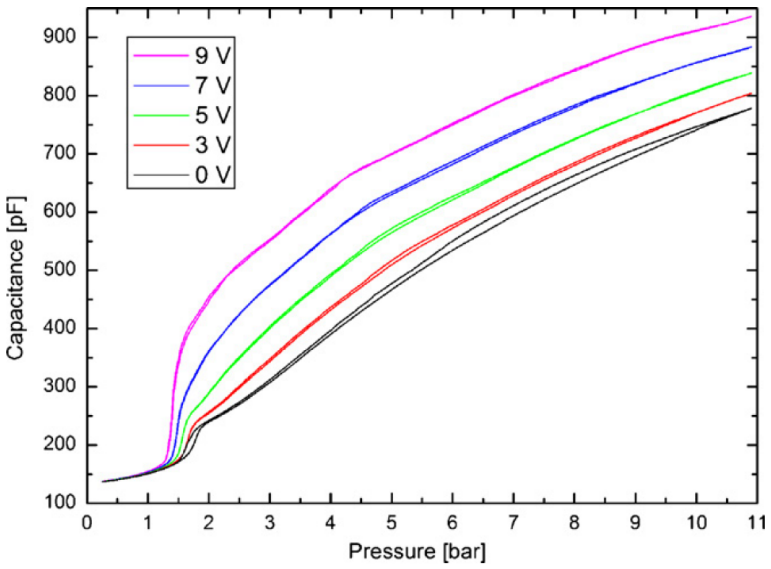

Figure 3.13: *Capacitance mesured as a function of pressure for different bias voltages [31]*

$$P = \omega(r)\frac{16Eh^3}{3a^4}\frac{1}{(1-\upsilon^2)}\frac{1}{\left[1-\left(\frac{r}{a}\right)^2\right]^2} \tag{3.12}$$

were $w(r)$ is the deflection of the diaphragm at a distance r from the center and a is the radius of the diaphragm.

For small deflection the model is simplified to:

$$P = \omega_c\frac{16Eh^3}{3r^4}\frac{1}{(1-\upsilon^2)} \tag{3.13}$$

were w_c is the deflection in the center of the diaphragm and r is the radius.

The stress is better distributed in circular diaphragms, since the corners of the square diaphragms are areas of high stress.

3.3.3 Bossed diaphragm

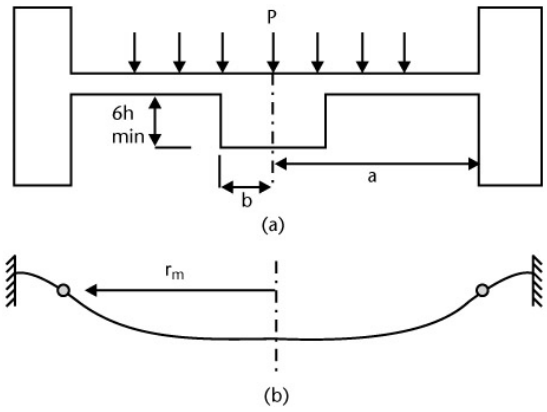

Figure 3.14: *(a) bossed diaphragm geometry, (b) the produced displacement of the membrane under uniform pressure [18]*

The equation which describes deflection of the membrane due pressure of the bossed diaphragm is [18]

$$P = \frac{Eh^3}{A_p a^4}(\omega) + B_p \frac{Eh^3}{a^4}\left(\omega^3\right) \tag{3.14}$$

$$A_p = \frac{3(1-\nu^2)}{16}\left(1 - \frac{b^4}{a^4} - 4\frac{b^2}{a^2} log\frac{a}{b}\right) \tag{3.15}$$

$$B_p = \frac{\frac{7-\nu}{3}\left(1+\frac{b^2}{a^2}+\frac{b^4}{a^4}\right) + \frac{(3-\nu)^2}{1+\nu}\frac{b^2}{a^2}}{(1-\nu)\left(1-\frac{b^4}{a^4}\right)\left(1-\frac{b^2}{a^2}\right)} \tag{3.16}$$

The normal stress of the diaphragm is maximum at the outer perimeter of the diaphragm, which is the region where the diaphragm is clamped. This stress is equal and opposite to the stress in the inner perimeter, where the boss begins. Thus, because of last there should be a middle point between the outer and inner perimeter (r_m in Figure 3.14 (b)) where the stress is equal to zero. Finally, the normal stress in the inner and outher perimeter is equal to [18]

$$\sigma_{outer} = \sigma_{inner} = \pm\frac{3P}{4h^2}\left(a^2 - b^2\right) \tag{3.17}$$

4. MANUFACTURING PROCESSES FOR CAPACITIVE SENSORS

The most common silicon based methods used for the fabrication of capacitive sensors are the use of etch stop or timed etch processes, deep reactive ion etching (DRIE) and wafer bonding [19]. In the first part of this chapter these processes are described briefly. Nowadays, polymers have been incorporated into sensing devices due to their properties. In the second part of this chapter these properties are described as well as some polymer processes and materials are explained.

4.1 Silicon based processes

4.1.1 Wet Etching

Wet etching is a process where material is removed using a chemical solution that dissolves the exposed region [32]. There are two processes, isotropic and anisotropic etching.

Isotropic etching

In this process the rate of material removal does not depend on orientation of the crystal lattice [32]. However, the etching depends on the type of substrate, the chemistry of the etchant, the material of the masking layer and its adhesion to the substrate to be etched, the temperature and the mixing conditions of the solution [32]. The isotropic etchants usually are composed of a mixture of nitric, hydrofluoric and acetic acids [33].

Anisotropic etching

Unlike isotropic etching, anisotropic etching rates depend on the crystal orientation [32] and on the doping level [33]. The most usually used anisotropic etchants are inorganic alkaline solutions such as KOH, LiOH, NaOH, CsOH and organic alkaline solutions which can be mixtures of ethylene diamine, pyrocatechol and water (EDP) or hydrazine (N2H4/H2O or NH4OH) [33].

4.1.2 Dry Etching

Dry etching involves techniques were reactive vapours or glow-discharge plasmas of reactive species are used to etch materials. These techniques are classified as vapour etching and plasma assisted etching respectively [32].

Vapor etching

This method is useful for surface micromachining in dry conditions. Xenon diflouride gas, XeF_2, is the most important commercially vapor etchant. This vapor etchant is highly selective for silicon, thus it does not etch metals, silicon dioxide or other materials [32].

Plasma-Assisted etching

Plasma etching offers the possibility to etch substrates anisotropically [22]. First, ions are produced in a low-pressure glow discharge plasma or an ion source [22]. When these ions are directed to the surface of the substrate they react with the materials in the surface and can also produce sputtering effects [22,32]. The chemical reactions effects means that the surface atoms are converted to volatile species, which can be removed with a vacuum pump and sputtering means that material is removed by direct ion-beam bombardment [32]. Reactive ion etching (RIE) is a plasma-assisted etching where low pressures and high degree of directionality is used [32].

Deep reactive ion etching (DRIE) is a variant of reactive ion etching. DRIE process exploits the formation of chemical crosslinking in the polymer due to glow discharge. Bosch Company developed a process where steps of reactive ion etching in an SF_6 plasma and deposition of polymer from C_4F_8 plasma are alternating [32]. With this process is possible to achieve deep features, this is because during the etching step the polymer is rapidly removed from the bottom but remains in the sidewalls, etching in this way the bottom but not the polymer protected walls. However, since the polymer eventually erodes, another polymer deposition step is needed [32].

4.1.3 Wafer bonding

Wafer bonding consists of bonding two wafers together to create a stacked wafer structure. The wafer bonding methods are: silicon fusion bonding or direct silicon bonding, anodic bonding or field-assisted bonding, and bonding with an intermediate layer [32].

Silicon fusion bonding

The direct silicon bonding is a difficult process since the needed microroughness of the silicon wafers must be less than 1 nm [22]. The process starts by the cleaning of the wafers to remove any particles that could create a gap between the wafers. The next step is the hydration of the wafers, which usually occurs during the cleaning step. Then, the hydrated surfaces are contacted and pressed together; the adhesion is possible using hydrogen bonding. Then the wafers are heated at high temperatures, on the order of 1000 °C, to fuse the wafers together. It is also possible to bond wafers with thermal oxide on them to form a structure known as silicon-on-insulator (SOI) and patterned wafers to form sealed cavities and other structures [32].

Anodic bonding

This method consists of the bonding of a metal plate or an electric conductor such as silicon, and a glass wafer [22]. Using silicon, the process starts by joining the silicon wafer with the glass. Next, the wafers are heated and a positive voltage is applied to the silicon. This causes the repulsion of sodium ions from the glass, which creates a negative charge in the glass surface, this process is depicted in Figure 4.1. Thus, the positive charged silicon is attracted by the negative charged glass; therefore the wafers are fuse at high temperatures. The bonding is monitored by measuring the current, which drops to zero when the bonding is completed [32].

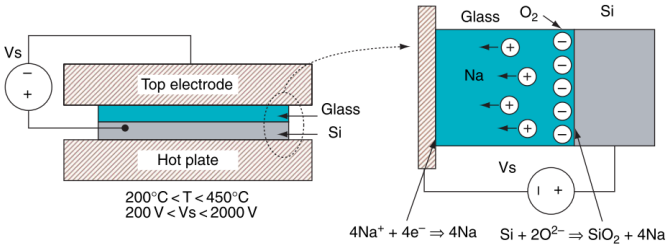

Figure 4.1: *Anodic silicon-glass bonding configuration [34]*

Bonding with an intermediate layer

This process consists of the use of adhesives or solders to bond material layers. The adhesives used should provide the cleanliness and thermal requirements of microfabrication. One method is to use polymeric adhesives include polyimides, silicones or epoxy resins. Another method is to use glass frits, in this procedure the glass frits is applied to one of the wafers and then the two wafers are contacted and annealed. Also, it is possible to use conventional solders and thermocompression bonding where gold layer is applied to the wafers and are pressed at a temperature about 300 °C [32].

4.1.4 Silicon based processes used to fabricate capacitive pressure sensors

The processes that can be used to fabricate capacitive pressure sensors are mentioned on Table 4.1. The most common process used to fabricate the diaphragm of capacitive sensors is anisotropic wet etching. Figure 4.2a shows the structure that results from this process. Using this method the thickness of the diaphragm can be controlled by timing, boron doping or electrochemical etch stop [18]. An example of the fabrication of a capacitive pressure sensor developed by Lee *et al.* [35] is showed in Figure 4.2b. This sensor was constructed using anisotropic etching of silicon and anodic bonding, to assemble a metalized Pyrex 7740 glass die with the silicon diaphragm [18]. Furthermore, to manufacture bossed diaphragms, anisotropic and isotropic etching can be employed [18].

Recently, in order to avoid parasitic capacitances sensors have been integrated in the electronics. By using bulk etching processes (described before) combined with CMOS circuitry researches have achieved this integration. However another common approach is the use of surface micromachining processes [18]. By using these processes, silicon on insulator (SOI) wafers can be employed making in this way possible to manufacture these structures [18].

Table 4.1: *Processes that can be used to fabricate capacitive pressure sensors [18, 19, 32]*

Structure	Processes
Diaphragm	Wet etching and dry etching techniques
Electrodes	Physical vapor deposition: evaporation (e-beam evaporation) and sputtering (more commonly used), electrodeposition and chemical vapor deposition (CVD)
Assembly of structures	Wafer bonding

The materials and processing methods that can be used to fabricate touch mode capacitive pressure sensors are mentioned in Table 4.2. By changing the parameters of the process this design can be used to measured pressures from 10^{-4} to 10^{3} psi [29]. Thus, is possible to use this design in the biomedical pressure range from 0 to 300 mmHg.

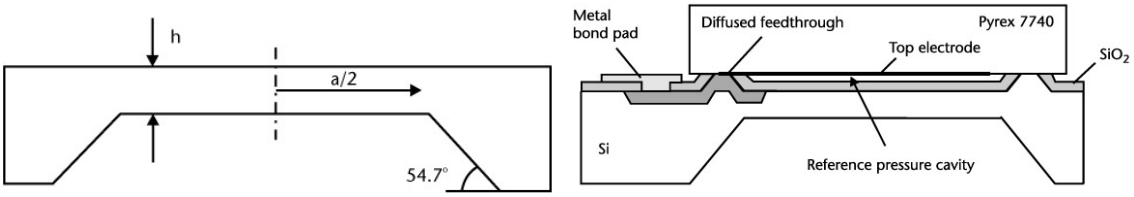

(a) Anisotropically etched silicon diaphragm *(b) Silicon/Pyrex capacitive pressure sensor*

Figure 4.2: *Examples of structures resulted using silicon based process to fabricate capacitive pressure sensors [18]*

Table 4.2: *Materials and processing methods for touch mode capacitive pressure sensors [29]*

Diaphragm material	Substrate material	Assembly technology
Single crystal silicon	Glass	Anodic bonding
Single crystal silicon	Silicon	Fusion bonding
Poly-silicon	silicon	Surface-micromachining
Silicon nitride	Silicon	Surface-micromachining
Polymeric materials	Silicon	Surface-micromachining
Metal	Glass/Ceramic	Eutectic bonding, soldering
Metal	Polymer	Polymeric seals
Ceramic (metallized)	Ceramic	Glass seal, metal seal
Polymeric materials (metallized)	Polymers	Polymeric seals, glues

4.2 Polymers processes

Nowadays, polymers have been used in the fabrication of MEMS principally due to their low cost, chemical inertness, low electrical and thermal conductivity. In addition, it is possible to modify their surface and most of them are biocompatible [34]. Polymer processes are described and later some polymers used in MEMS technology are presented.

4.2.1 Injection molding

Even though injection molding has been used for the manufacturing of macroscale products such as CDs and DVDs, nowadays this technology has been used in the production of microscale components [34]. This process begins with the production of a mold with microstructures, this can be done by using for example LIGA process, silicon micromachining techniques and SU-8 photolithography [34]. The process of injection molding is depicted in Figure 4.3 (a). As can be seen in this Figure, the mold needs to have a cavity where the polymer is injected into the mold. The mold is heated at a temperature greater than the glass transition temperature (T_g) of the polymer and the polymer is heated in the injection unit to obtain a viscous melt which can be injected into the mold. Then the cavity where the polymer is located

is cooled below the T_g and then is demolded [34].

4.2.2 Hot embossing

Hot embossing uses a mold or master and a film of thermoplastic polymer. In this process, the film is pressed against the master and then the film and the master are heated above T_g [34]. Thus the polymer takes the form of the mold inserts. Finally, the master and thermoplastic are cooled and then separated [34]. This process is depicted in Figure 4.3 (b).

4.2.3 Casting

Casting is a process where materials like thermoplastics polymers in liquid state are deposited into a mold, thus, when the polymer is solidified, takes the form of it, this process is depicted in Figure 4.3 (c) [34]. Further, reaction casting is a process where materials other than thermoplastics are used, for example the elastomer Polydimethylsiloxane (PDMS). In this process the material is not melted and comes at two separated solutions, when mixing those parts with heat or UV light produce the cross-linking of the polymer, increasing in this way its viscosity [34].

4.2.4 Stereolithography

This technology was developed in 1980 for rapid prototyping for fluid dynamics testing and visualization for automotive and aeronautical applications. In order to construct the object, it needs to be deconstructed into a series of 2D layers which are later reproduced by polymerization of a resin using a laser. The process is depicted on Figure 4.3 (d). The laser beam is focused onto a region of a photosensitive prepolymer solution. The light induces polymerization of the solution, so each 2D layer is formed by scanning the laser across the surface of the solution. When a layer is formed fresh liquid is spread on the top of it and the process is repeated [34].

4.2.5 Ink-jet printing

Ink-jet printing use microscale droplets which are propelled through a narrow nozzle [34]. This technique has been used for reproduction of text, however nowadays instead of using ink, polymer liquids has been used [34]. This technique has been used with biopolymers such as DNA, proteins and cells [34]. Considering that these bipolymers are sensitive to temperature and lose their properties when exposed to other solvents, hydrogels have been used to enclose these proteins as shown on Figure 4.3 (e). In this manner, their functionality is not lost [34].

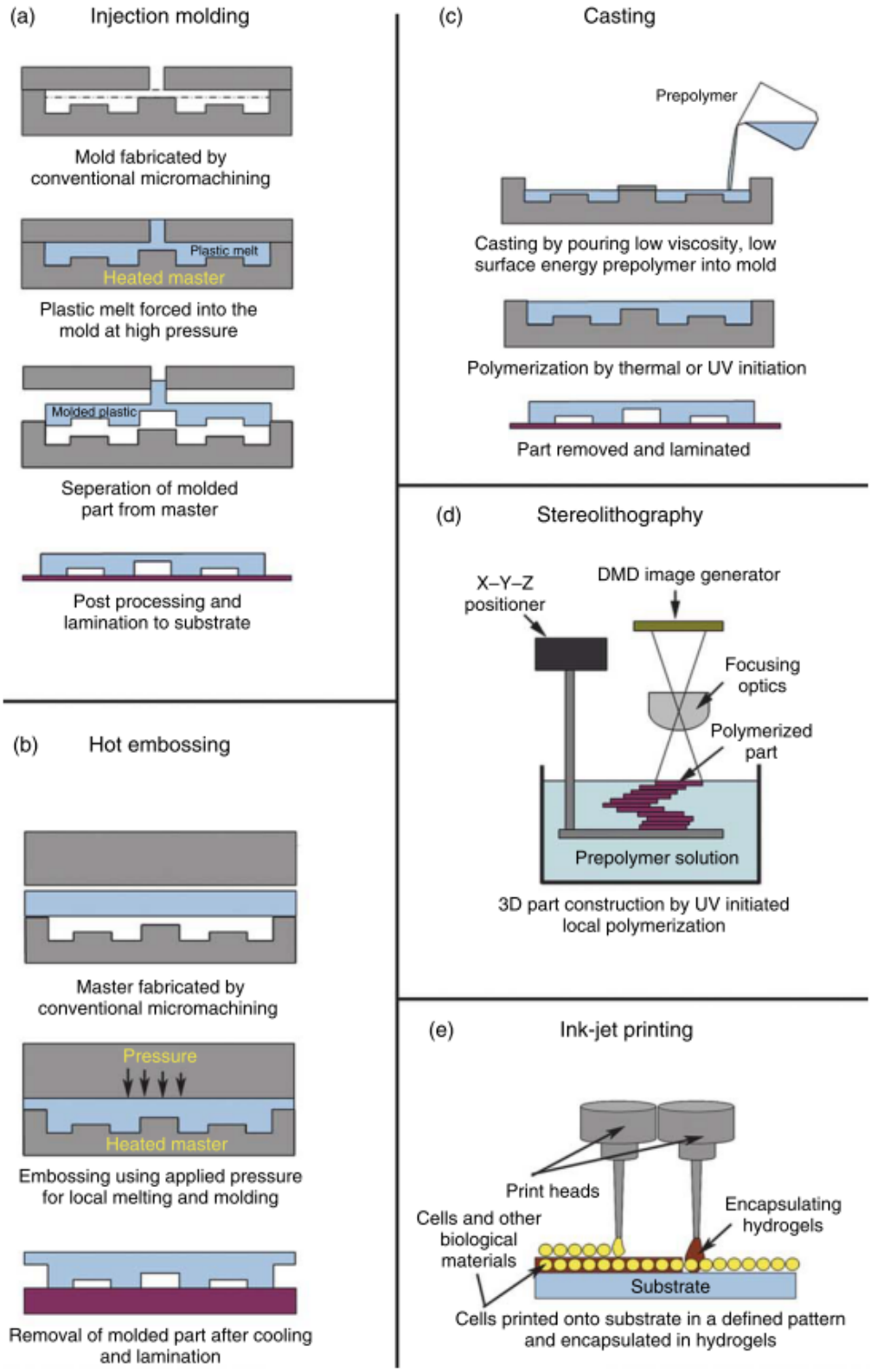

Figure 4.3: *Injection molding, hot embossing, casting, stereolithography and inkjet printing process flow [34]*

4.3 Polymers

4.3.1 Polydimethylsiloxane PDMS

Polydimethylsiloxane (PDMS) is a silicon elastomer which has been use for protection of electronic components against environmental influences and mechanical shocks and as dielectric isolator [36]. Furthermore, now PDMS is the most extensively used polymer in MEMS, particularly in microfluidic devices and bioMEMS [34].

The chemical formula of PDMS is $-[(CH_3)_2Si\text{-}O\text{-}]_n$ [37]. PDMS contains a Si-O backbone, organic groups are frequently attached to the Si-C bond and due to the low rigidity of the backbone, the methyl groups are exposed which produce low intermolecular interactions and low surface tension [34]. The number of repeating units in the polymer chain and the degree of cross-linking makes possible to produce fluids, emulsions, lubricants, resins, elastomers and rubbers [34].

Some PDMS properties are listed in Table 4.3:

Table 4.3: *PDMS properties*

PDMS properties
Thermal stability
Low temperature performance and minimal temperature effect
Good resistance to UV radiation
High permeability to gases
Good damping behavior
Antifriction and lubricity
Hydrophobic and physiologically inert
Shear stability
Weak intermolecular forces
Excellent dielectric strength

Furthermore, PDMS has proven to be biocompatible and has useful properties such as optical transparency and flexibility [38]. The mechanical properties of PDMS depends on the mixing ratio between the base polymer and curing agent [38].

Moreover, it is possible to cast PDMS to obtain replicas with the desired shape given by the mold [39]. This process is usually used to fabricate microfluid channels for microfluidic devices [39].

As mentioned before the surface of PDMS is hydrophobic and is inert due to the exposed methyl groups. For that reason, it is difficult to bond PDMS to PDMS and to other substrates [34]. A normally used method to become the surface of PDMS hydrophilic is to oxidize the surface by plasma oxidation, this converts the methyl groups into hydroxyl groups. Thus, with this method it is possible to bond two oxidized layers of PDMS in an irreversible seal [34].

4.3.2 SU-8

SU-8 is a negative photoresist developed by IBM for LIGA applications [34]. After its development, photoresists are used as structural layer for MEMS and microfluidic devices [34].

The main component is EPON resin SU-8 which is dissolved in an organic solvent γ-butyrolacton. The viscosity of SU-8 is determined by the ratio of the solvent to the resin [34, 39].The thickness of the resist layer is dependent on this ratio and on the spinning speed [34]. SU-8 can be used to obtain 20 to 1500 μm deep structures with aspect ratio greater than 10:1 by photolitrography, even though it is difficult to achieve [40]. The UV absorption of the resist depends on the photoinitiator content in the resin [40]. The photoinitiator is a photo Lewis acid generator which constitute the 10% of the mass percentage of the resin [34]. In addition, SU-8 resist has a higher absorption rate at wavelengths less than 350 nm [40].

4.3.3 Parylene

Parylene has been used for fabrication of MEMS devices, like acceleration and pressure sensors, as well as for fabrication of microfluidics channels and valves [39]. The properties that makes Parylene a good choice for MEMS devices is that films made of these polymers have low intrinsic stress, chemical inertness, etch selectivity and can be deposited at room temperature [39]. In addition, Parylene N has frequency invariable dielectric constant [39].

Parylene is a general name for a polymer series where the basic polymer is called Parylene N, which is a poly-para-xylynene [39]. Parylene is a thermalset polymer and is the only that can be deposited by chemical vapor deposition (CVD) [39]. Further, Parylene C, the second member of the series, is a Parylene N modified polymer where the chlorine atom is substituted by an atom of the aromatic hydrogens [39]. Parylene C polymer has low permeability to moisture and corrosive gases [39].

5. PRESSURE SENSORS FOR PRESSURE GARMENTS

Most of the methods used to measure the pressure applied to the skin by pressure garments is to measure the interface pressure. In these methods the sensors are placed between the skin and the pressure garment [13].

Many groups have intended to develop an interface pressure sensor capable of measure accurately small pressures applied by pressure garments. In the International consensus meeting held in Vienna in 2005, a group of medical experts and representatives from the industry gathered to create a series of recommendations for the use of the suitable methods for measuring the interface pressure and estimate the tension applied by compression treatments [16].

Besides the general desirable characteristics of sensors such as, reliability, low hysteresis, linearity and accuracy, they defined that an ideal interface pressure sensor should have the following characteristics: should be small, thin and flexible, present continuous output, the measurement should not be affected by curved surfaces, moisture and temperature, and should not irritate the skin when using it for long periods of time [11, 16, 41]. Additionally, it would be preferable for the system to be able to measure pressure on several anatomical sites at the same time [16].

5.1 Subdermal pressure measurement

Subdermal pressure is the pressure beneath the skin, Brace and Guyton defined it as: "The total tissue pressure in the subcutaneous tissue is determined by the sum of: (i) the pressure due to the radial tension of the skin, and (ii) any external pressure" (cited in [13]), thus the subcutaneous pressure is modified by external pressure applied to the skin, like the one applied by pressure garments [13].

An invasive method used to measure subdermal pressure was developed by Giele *et al.* [13] in 1997. This group developed this invasive method for two reasons. The first reason was that the interface techniques are an indirect measurement since these do not measure the subdermal pressure directly. The second reason was that in these techniques the garment tension is increased because of the placement of the sensor between the skin and the garment.

This group used a 19G needle connected to a continuous low flow pressure transducer. To calculate the pressure applied by a pressure garment the pressure was

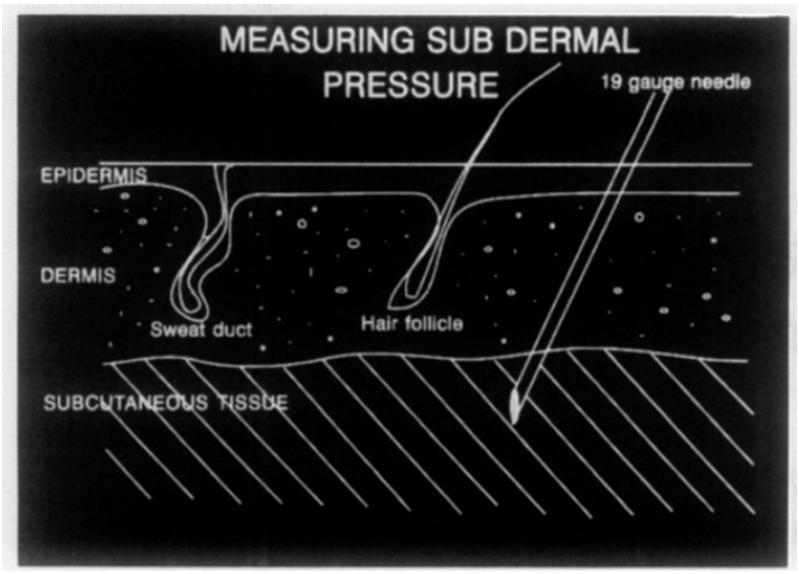

Figure 5.1: *Diagram of the measurement of the subdermal pressure using a 19G needle [13]*

recorded first without the garment and secondly using it. To measure the subdermal pressure, the needle was inserted into the skin and the pressure reading was obtained. A diagram of this is showed on Figure 5.1.

Further, to compare subdermal pressures and interface pressures, they performed measurements using a pneumatic sensor [13]. The pneumatic sensors consisted of an air cell connected to an air reservoir [42]. The operation principle of these sensors is that the cell is filled with air at known pressure and in order to inflate the cell the pressure must be slightly greater than the pressure applied to the sensor. When the pressure in the cell is greater than the pressure applied, the volume of air in the cell increases suddenly, this cause an abrupt change in the rate of pressure increase and corresponds to the pressure applied to the sensor. [42].

In their results, they found that the pressure applied by the pressure garment was transmitted subdermally. They found that the results of the interface methods dependeds on the nature of the tissue. When the measurement was performed over soft tissues, interface method recorded greater pressures than with the direct method. On the other hand, smaller pressures were recorded in bony tissues. Thus, the interface methods tend to exaggerate or minimize the pressures [13]. According to Lai *et al.* [41], this technique was not adopted in clinical and research studies because of it invasive character, however interface techniques have been developed.

5.2 Interface pressure measurement

The earliest approach to measure interface pressure used the electro-pneumatic principle and was developed by the American aviation industry in 1946 to measure

pressure beneath anti-G-suits. The electro-pneumatic principle is similar to the pneumatic principle, except that has an electric contact inside the cell. The electric contact is broken when the applied pressure and the pressure inside the cell are in equilibrium. [42].

The system in the anti-G-suits consisted of a flat capsule connected to a manometer and a syringe. In this system, a pressurized fluid is injected into the capsule, then, the external pressure applied to the capsule is equal to the pressure needed for the fluid to flow into it. Consequently, the fluid would switch the contacts located in the walls of the capsule resulting in a light indication [14].

In 1980, Robertson *et al.* [14] used a 28 mm electropneumatic sensor similar to the one developed in 1946, for the study of the effects of pressure garments on the treatment of hypertrophic scars. Figure 5.2 shows the system, when the electric contact is broken the light indicator switch [43]. Using this system, in order to reduce error, baselines readings were taken before and after the measurements. They found that constant baselines were achieved on circumferences of the size of a non flexed proximal interphalangeal joint [14]. This means that the sensor is not able to give a reliable reading in flexed joints and with smaller sizes than the fingers.

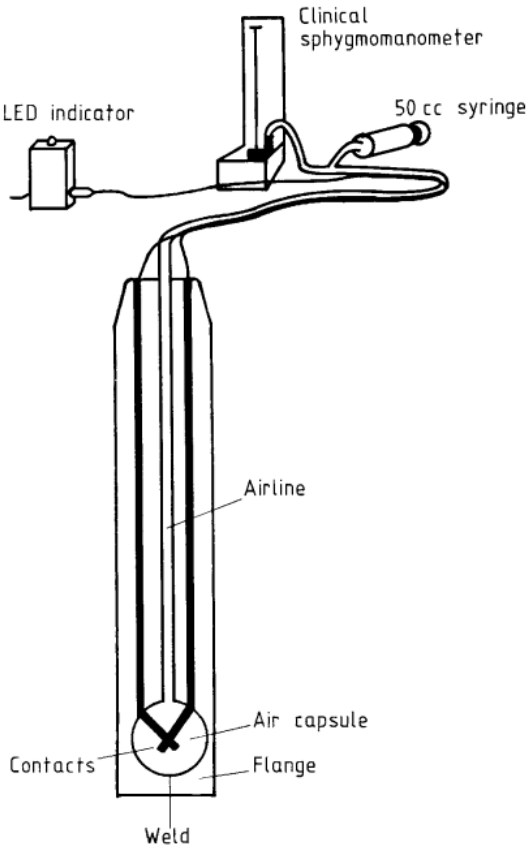

Figure 5.2: *Robertson's 28 mm electropneumatic sensor system [43]*

5.3 Commercially available sensors

At the eighties and early nineties many groups developed electropneumatic and pneumatic pressure sensors [12]. There are a few commercially available pneumatic sensors used for measure interface pressure clinically, see Table 5.1. According to Partsch *et al.* [16] some of the advantages of pneumatic pressure sensors for measuring interface pressure are that these transducers are thin, flexible, easy to use and cheap. On the other hand, these devices are sensitive to temperature and for dynamic measurements additional equipment is needed. Even though fluid filled or pneumatic sensors are flexible and dynamic measurements are possible they have problems during motion and their size increase when filled, increasing the measurement errors [16].

Table 5.1: *Pneumatic, pneumatic-electric and pneumatic-piezoelectric pressure sensors used to measure interface pressure. Modified from [16]*

Pneumatic, pneumatic-electric and pneumatic-piezoelectric pressure sensors (some commercially available)
Oxford Pressure Monitor (Talley Ltd, Ramsey, Hampshire, UK)
Talley Pressure Evaluator (Talley Ltd)
MST MKIII Salzmann (Salzmann Medico, St Gallen, Switzerland)
Digital Interface Pressure Evaluator (Next Generation Co., Temecula CA, USA)
Scimedics Pressure Evaluator Pad (Vista Medical, Winnipeg, MB, Canada)
Kikuhime (Meditrade, Soro, Denmark)
Juzo Tester (Elcat, Wolfratshausen, Germany)
Sigat Tester (Ganzoni-Sigvaris, St. Gallen, Switzerland)
PicoPress (Microlab Ellettronica Sas, Italy)

Some other groups have developed interface pressure sensors making use of piezoelectric and piezoresistive phenomena, as well some others have developed capacitive pressure sensors, see Table 5.2. Resistance sensors are thin and can be used for dynamic measurements, however are sensitive to curvature, temperature and are not useful for long term measurements [16].

Table 5.2: *Piezoelectric, resistive and capacitive interface pressure sensors. Modified from [16]*

Piezoelectric Fluid-filled, fluid-filled-resistive interface pressure sensors
MCDM-I (Mammendorfer Inst. Physik, Munich, Germany)
Strathclyde Pressure Monitor
FlexiForce (Tekscan)
Skip Air pack Analyzer (AMI Co., Japan)
Resistive and strain gauge interface pressure sensors
FSR, FSA (Vista Medical, Winnipeg, MB, Canada)
Fscan, Iscan (Tekscan, South Boston, MA, USA)
Rincoe SFS (Rincoe and Associates, Golden, CO, USA)
MCDM (Mammendorfer Inst. Physik, Munich, Germany)
Fontanometer (Gaeltec Ltd, Dunvegan, Isle of Skye, Scotland)
Diastron (Diastron Ltd, Andover, Hampshire, UK)
Capacitive interface pressure sensors
Kulite XTM190 (Kulite Semiconductor Products, Leonia, NJ, USA)
Precision (Precision Measurement Co., USA)
Xsensor (Crown Therapeutics, Belleville, IL, USA)
Pliance (Novel, Munich, Germany)

5.3.1 Comparison of commercially available interface pressure sensors

Commercial pneumatic sensors

Three examples of commercially available pneumatic sensors are Kikuhime, SIGat (Sigvaris interface-pressure gauge advanced tester) and PicoPress, all of them have been tested by different research groups.

Van den Kerckhove *et al.* [12] studied the reproducibility of repeated measurements using the Kikuhime pressure sensor, shown in Figure 5.3. Their results show good reproducibility, accuracy, linearity and intra-observer reliability and reproducibility. They also found that the pressure applied by the garment can be overestimated since the pressure sensor placed between the skin and the garment increase the tension of the latter [12].

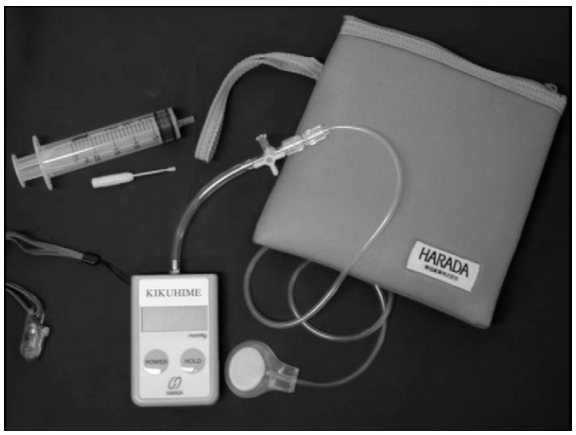

Figure 5.3: *Kikuhime pressure sensor [12]*

SIGat instrument was used by Blätter *et al.* [44] and by Gaied *et. al.* [45] to measure the force applied by medical compression stockings. SIGat system is able to measure interface pressure in static and dynamic conditions. The sensor consists of a flat plastic bag (dimensions 6×5×0.03 cm) which is inflated with air under constant flow, diagram shown in Figure 5.4 (a). The system includes a electronic measurement device to process the measurement data, in these device the pressure curve versus time is displayed and shows two slopes, depicted in Figure 5.4 (b), the first slope represents the moment when the pressure on the bag is less than the interface pressure, and the second slope shows the time where the pressure on the bag is greater than the interface pressure. Therefore, the change in slope means the pressure generated by the pressure garment, P_0 on Figure 5.4 (b) [44].

In their results using SIGat system, Blätter's group found good values of accuracy and reproducibility [44] and Gaied *et al.* [45] found that the sensor measurements have variations in curvature geometries.

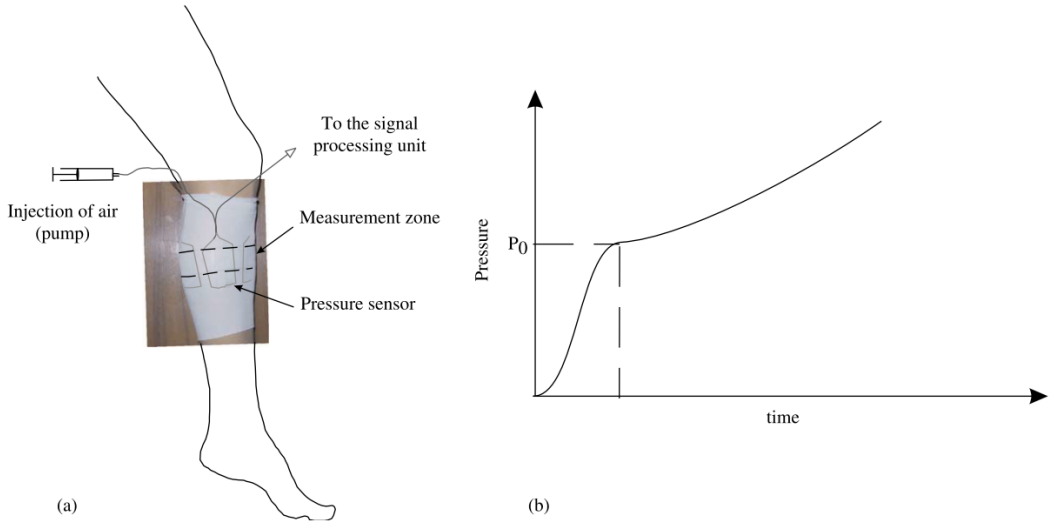

Figure 5.4: *(a) Diagram of SIGat system, (b) Pressure curve vs time [45]*

Mosti [46] studied the reproducibility and accuracy of the PicoPress system in laboratory and in in-vivo test. PicoPress system consist of a flat probe with thickness of 0.2 mm, a diameter of 5 cm and surface of 19.62 cm^2. In this system, the probe is inflated with air with an electrically controlled syringe [46]. In the laboratory test, Mosti found good linearity and accuracy when tested with a sphygmomanometer (device used to measure blood pressure). In the in-vivo test the system was compared with Kikuhime and SIGat, according to their results, see Figure 5.5, SIGat shown better values of accuracy, linearity and reproducibility [46].

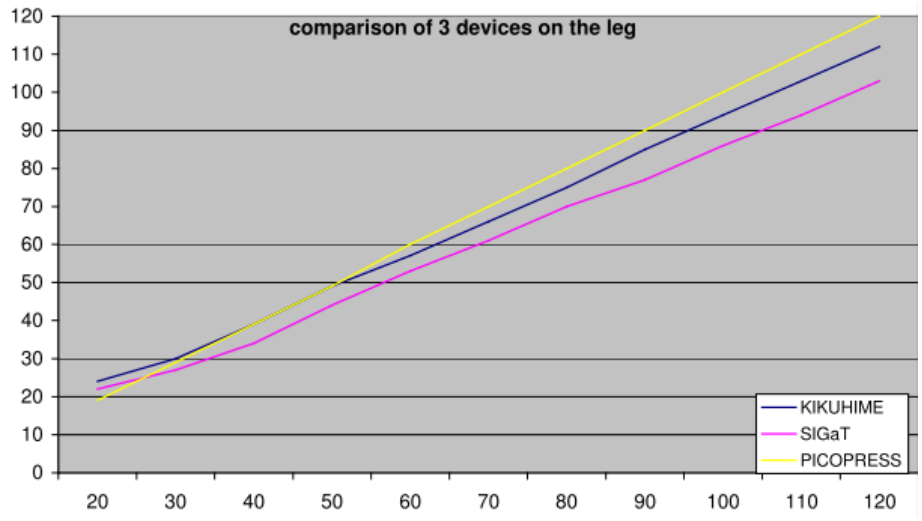

Figure 5.5: *Comparison results of Kikihime, SIGat and PicoPress sensors (average of three measurements). The sensors were fixed on the leg and a manometer superimposed on the sensors exerted pressure from 20 to 120 mmHg [46]*

Commercial piezoresistive sensors

At the end of the nineties, Tekscan developed a piezoresistive sensor called "FlexiForce" [12]. The sensor uses a pressure sensitive ink. The electrical resistance of the ink changes with applied force and the resistance variation is inversely proportional to the applied force. Further, the sensor is constructed by applying a layer of silver, used as conductive material, and a layer of ink in two separate layers of polyester film. Then, this polyester films are put together to form the sensor [11].

Ferguson-Pell *et al.* [11] evaluated the performance of the FlexiForce sensor to measure interface pressure on bandages, compression stockings and pressure garments. Because pressure garments and bandages apply pressure between 20-30 mmHg, sensors operating in the range of 0-464.9171 mmHg were used for this study. The maximum pressure employed was 50 mmHg and the active area of the sensor was 7.122×10^{-5} m^2. [11].

Ferguson-Pell *et al.* [11] tested the sensor for drift, repeatability, linearity and hysteresis. For these tests, they used a tilt table to apply pressure to the sensor. For testing the behavior of the sensor under curvature surfaces they taped the sensor inside a pipe and used an inflated condom connected to a sphygmomanometer to apply force to the sensor. From this study, they found that the curvature changed the sensitivity and the offset of the output sensor, see Figure 5.6. They found that with a radius less than 32.5 mm the offset increased while the sensitivity decreased, suggesting that to get correct measurements the optimum radius of curvature should be greater than 32 mm.

Further, this group obtained good results from the drift, repeatability, linearity and hysteresis, tests which correlated well with the values given by Tekscan. Their results of linearity and hysteresis test are depicted in Figure 5.7. From the drift test, they found different results from readings immediately after applying the loading and from the readings taken after 10 min. Thus, it can be inferred that the sensor is appropriate for static measurements. Additionally, they found that the sensitivity, see Figure 5.7 (a), decreased at smaller forces (<10 mmHg) and was greater at higher forces (10 mmHg to 50 mmHg) [11].

Even though Piezoresistive sensors are accurate, they are sensitive to temperature and their sensitivity decrease in pressures lower than 10 mmHg. On the other hand, capacitive sensors have shown good qualities like high sensitivity and flexibility. Additionally, their temperature dependency and power consumption are lower in comparison with piezoresistive sensors [41].

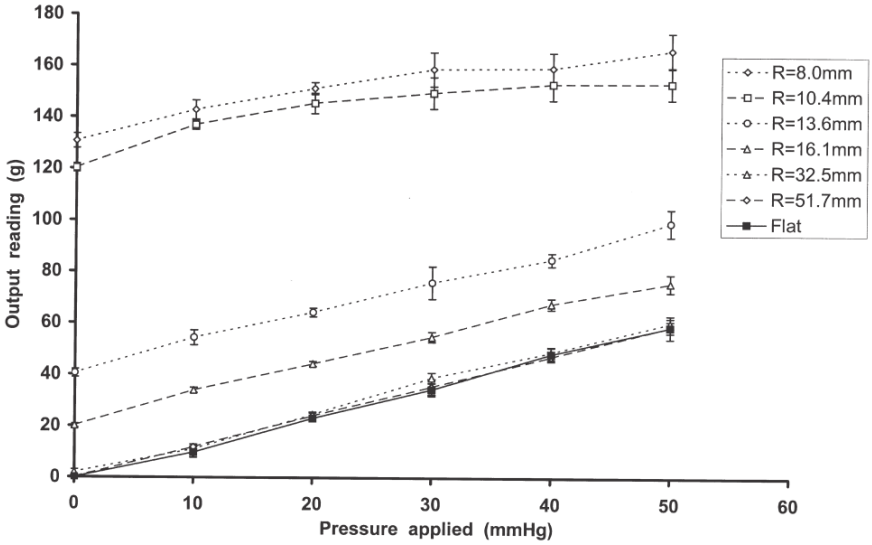

Figure 5.6: *Flexiforce sensor response with different radii of curvature, the bars indicate standard deviation [11]*

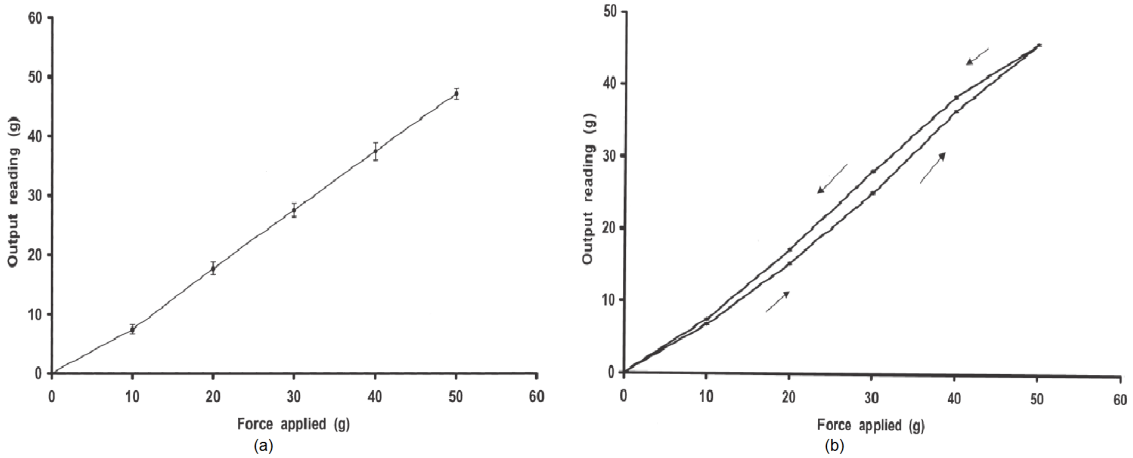

Figure 5.7: *(a) Results from linearity test, (b) results from hysteresis test [11]*

Commercial capacitive sensors

Lai *et al.* [41] studied the performance of a capacitive sensor when measuring interface pressure on pressure garments. They used a commercially available system called Pliance X (Germany-Novel Electronics), shown in Figure 5.8. It consists of a capacitive sensor, an electronic analyzer and software. With this system it is possible to connect several sensors to the system to perform different measurements. The system used a capacitive sensor with 10 mm of diameter and with less than 1 mm thickness [41]. However, it was not possible to find more information about the structure and material of this sensor because the company keeps that information.

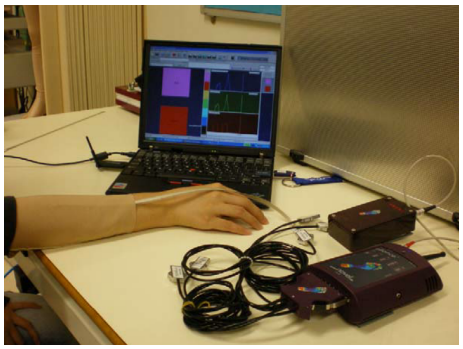

Figure 5.8: *Pliance X system [41]*

This group evaluated the sensor by laboratory and clinical tests. In the laboratory test, they evaluated the linearity and repeatability of the sensor using a system that consisted of a plastic disc, placed under the sensor to ensure that the pressure was transferred only to the sensor, and standard weights used to applied pressure to the sensor. They also measured the effect of the human skin elasticity on the sensor reading using a sphygmomanometer. Additionally, for the clinical trials, human subjects with hypertrophic scars were recruited. For this study pressure garments and pressure paddings with 3 mm thickness were used in order to increase the pressure applied by the garment [41].

In the laboratory tests, their results showed good linearity and reliability. In Table 5.3 are shown their results and in Figure 5.9 is shown the sensor output. The pressure error was less than 1 mmHg with weights from 5 to 50 g but the variability was greater with smaller values of pressure [41]. Thus, similar to the FlexiForce results, the variability increases at pressure smaller than 10 mmHg.

The clinical tests shown that when adding paddings and consequently increasing the pressure, the system was able to discriminate between different values of pressures. Additionally, they found that measured pressures were higher in young scars compared with mature scars, a comparison is shown on Figure 5.10. This differences might be due to the fact that hypertrophic scars become thinner and softer [41].

Table 5.3: *Results of linearity test of Pliance X system [41]*

Standard weight (g)	Applied pressure (mmHg)	Sensor value mean (mmHg)	Standard deviation	Coefficient of variation (%)
5	4.215	4.059	0.343	8.450
10	9.393	9.717	0.648	6.669
20	18.276	18.512	0.641	3.463
30	28.139	28.646	0.643	2.245
40	37.513	38.114	0.418	1.097
50	46.396	46.662	0.748	1.603

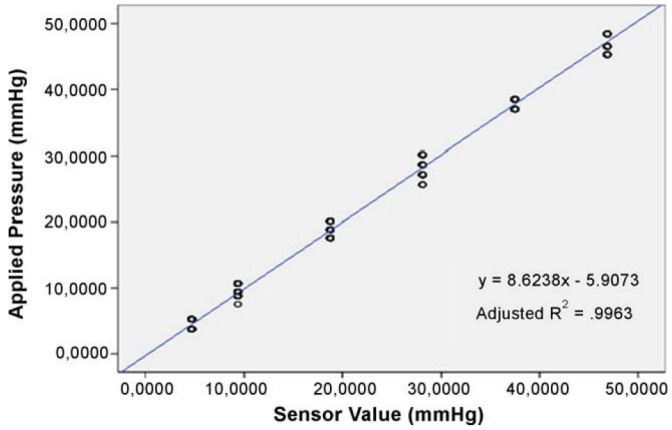

Figure 5.9: *Applied pressure versus sensor output [41]*

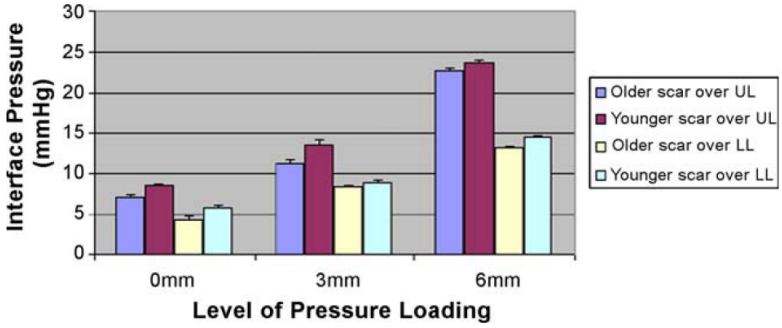

Figure 5.10: *Comparison between younger and older scars [41]*

6. PASSIVE RESONANCE SENSORS

Passive resonance sensors have many applications in biomedical engineering, such as, monitoring transcutaneous pressure, intracranial pressure and pressure monitoring of abdominal aortic aneurysm [47]. In this chapter the structure and operation principle of passive sensors is described. Next, recent works with passive resonance sensors are presented and finally a comparision between the characteristics of the different sensors is given.

6.1 Sensor structures

The main advantages of passive sensors are that they enable the possibility of wireless measurement and this eliminates the necessity of power supplies for the sensor. LC circuits, which consists of an inductor connected in parallel with a capacitor as shown in Figure 6.1, has been used for the design of passive resonance sensors [19]. In this configuration the device is composed of a coil and a capacitive sensor that form the LC circuit, also called tank circuit [19]. The operation principle is that when pressure is applied to a variable capacitive, the resonant frequency of the LC circuit changes [18]. However, other configurations exists where also the inductance can be variable. By using this configuration with a variable capacitor the device can be energized by coupling inductively an antenna as shown in Figure 6.2. In this way the change in resonant frequency can be detected by different techniques such as phase dip technique (see Appendix A), phase locked loop, techniques based on absorption of electromagnetic energy and others.

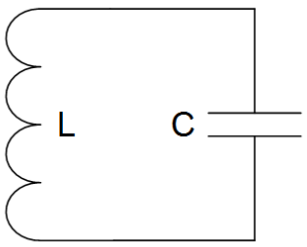

Figure 6.1: *LC circuit*

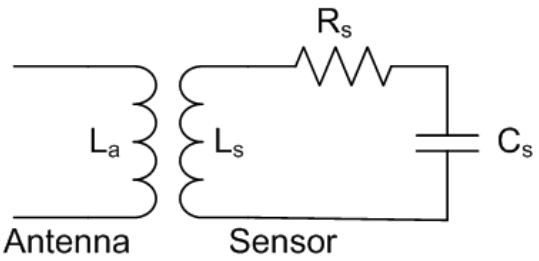

Figure 6.2: *Schematic of sensor coupled with an antenna*

First demostration of remote monitoring using LC circuit

In 1967 Collins developed an implantable passive sensor for monitoring the intraocular pressure in glaucoma patients [48]. Glaucoma is a disease characterized by the increase of the intraocular pressure which can damage the optic nerve and cause blindness [49]. The operation principle of the sensor developed by Collins consisted in the measurement of the change in volume of a gas bubble which was embedded between two planar coils. When pressure was applied, the change in distance between the coils modified the resonant frequency of the circuit.

The sensor design was composed of a pair of diaphragms made of polyester (polyethylene terephthalate polyester) connected to a pair of spiral coils, both structures were encased in a glass tube, see Figure 6.3 (a). The pair of spiral coils was connected to form a single inductor whose inductance changed with the separation distance between them , see Figure 6.3 (b) [48].

The sensor was interrogated remotely using a grid dip oscilloscope which swept a range of frequencies. The resonant frequency of the sensor was determined by detecting the resonant peak during the sweep. This was achieved by calculating the first derivative of the signal, which made possible to detect the zero-crossing using a tunnel diode amplitude comparator. Greater sensitivities were achieved by decreasing the spacing between the coils and diaphragm thickness. However, when implanted the resonant frequency of the device was lowered by the capacity between the tissue and the glass thickness. Additionally, the sensitivity of the sensor depended on the flexural stiffness of the diaphragm and capsule (glass) which flexural stiffness was controlled by the air inside it [48].

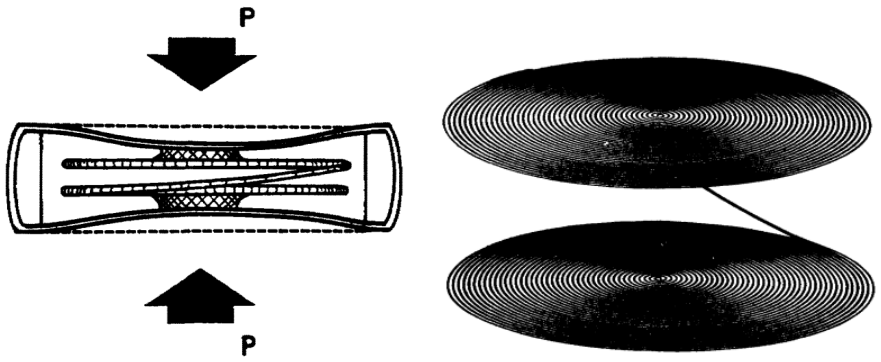

(a) Pair of spiral coils encased in a glass tube *(b) Pair of spiral coils*

Figure 6.3: *Design of the sensor developed by Collins [48]*

6.1.1 Recent works with passive pressure sensors

Flexible wireless pressure sensor for biomedical applications

Fonseca *et al.* [50] developed two types of implantable passive pressure sensors. In order to achieve easy implantation using a catheter, the sensors were intended to be flexible enough for this purpose. The first sensor type was a semi-hermetic sensor for acute use and the second had a hermetic design intended for chronic use, Figure 6.4 and Figure 6.5. The design of both sensors consisted of a cavity enclosed by parallel structures that formed capacitance plates, which were interconnected with an inductance. The deflection caused by applying pressure to one or both of the plates produced a change in the value of the capacitor. Consequently, the applied pressure could be calculated by measuring the change in resonant frequency of the LC circuit using an external magnetic loop.

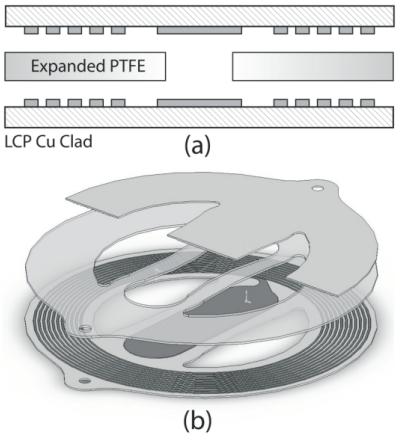

Figure 6.4: *Sensor for acute use, (a) Cross-sectional view, (b) Overview of LCP sensor structure [50]*

The materials used in the sensors intended for acute use were laminated sheets

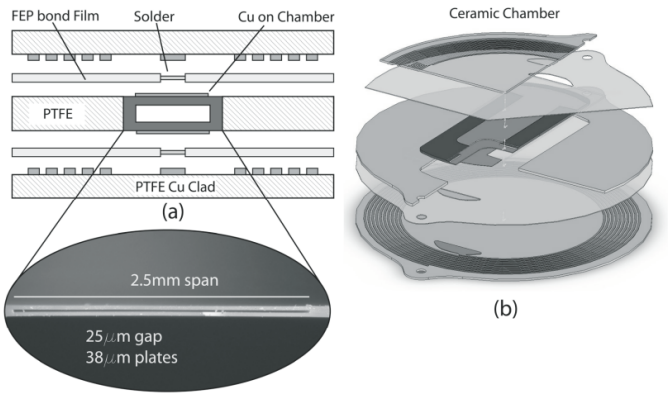

Figure 6.5: *Sensor for chronic use, (a) Cross-sectional view, (b) Overview of PTFE/Ceramic sensor structure [50]*

of copper-clad liquid crystal polymer (LCP) and for the based bonding inner layers expanded polytetrafluoroethylene (PTFE)(Teflon). The inductor structure was patterned into the LCP by lithography and wet-chemical etching. To obtain accurate dimensions of the inner layer, laser-cut was used [50].

For the sensors for chronic use, the methods and materials used for fabrication were copper-clad and non-clad PTFE layers, and the inner layers were made of Fluorinated Ethylene Propylene copolymer (FEP). These sensors contain a hermetic ceramic chamber to be used as pressure reference. For the fabrication of this chamber sintering of zirconia powders was employed. To form the inner layer of the chamber and inner layers of PTFE and FEP laser cut was used. Both types of sensors are self-packaged structures and can be modeled as a lumped LCR circuit.

Coils were employed to read the device. The readout device sent a burst of RF energy at the resonant frequency of the sensor and consequently started to oscillate during a time and decayed exponentially to zero. A phase-locked-loop was used to sense the sensor frequency response.

Wireless passive pressure sensor for high-temperature applications

In another work, Fonseca *et. al* [51] studied passive pressure sensors intended to be used at high temperatures. The use of wireless reading makes these sensors suitable to be used in hazardous environments. For fabrication of sensors, it is difficult to use different materials than silicon, because other materials manufacturing methods are not as well developed as silicon processes. For that reason, in this article ceramic materials were used, since there is a developed ceramic packaging procedure, called low-temperature cofireable ceramic (LTCC) that can be employed to construct these sensors.

The design of the sensor consisted of two electrodes enclosing two ceramic diaphragms and a vacuum-sealed cavity, Figure 6.6. This formed a capacitor which

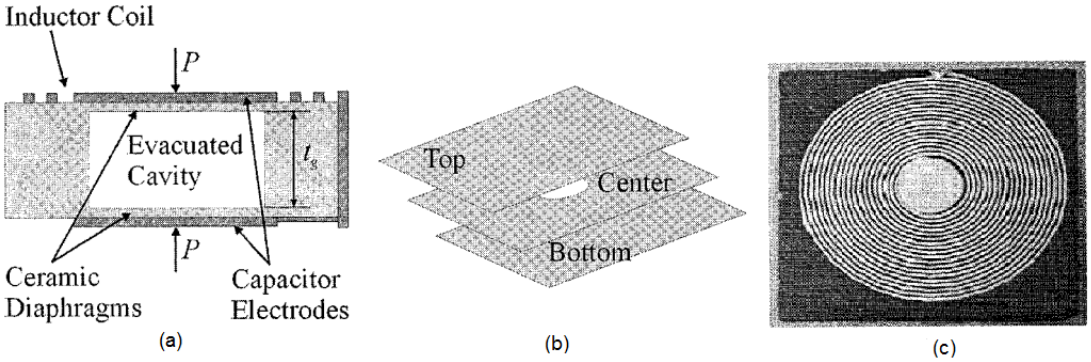

Figure 6.6: *(a) Cross-sectional view of sensor structure, (b) three layers of the sensor, (c) top view photograph of the sensor [51]*

was connected to a planar spiral inductor coil. When pressure was applied to one of the electrodes the distance between the diaphragms decreases, changing the capacitor value. The model of this sensor is an LC resonator circuit, so the change in impedance and phase response can be measured with an external coil. Thus, the sensors were interrogated using phase-dip technique. The ceramic material consisted of alumina and glass particles suspended in an organic binder (Young's modulus 152 GPa), and the conductor material was Dupont 6160 silver ink.

Intraocular pressure sensor for glaucoma application

Recently Chen *et. al* [47] developed and studied an implantable pressure sensor for continuing monitoring glaucoma patients. The sensor was interrogated wirelessly, so non-contact measurement was achieved. From a previous work of this group, they found that to increase the quality factor Q and the coupling factor k, the size of their LC sensor should be larger. Thus, to follow the requirements of small size needed to achieve minimally invasive implantation and to increase k^2Q factor, the design of the sensor consisted of a flexible coil disk. The sensor capacitor was formed of a pair of pressure-sensitive parallel plates fixed to a deformable diaphragm chamber, Figure 6.7. The coil was supported by a flexible/foldable disk, as mentioned before, this enables the use of a greater coil size. As mentioned before, a pressure applied to the diaphragm changes the value of the capacitance. This sensor also incorporates an air/gas cavity to provide a pressure reference.

The flexible coil disk was made of parylene C (poly-chloro-p-xylylene) which has a Young's modulus of approximately 4 GPa. The diameter of the coil disk was 4 mm to fit the normal diameter of the iris. For this application, the implantation of the sensor in the anterior chamber of the eye had the advantage of facilitating the alignment of the sensor and reader coils [47].

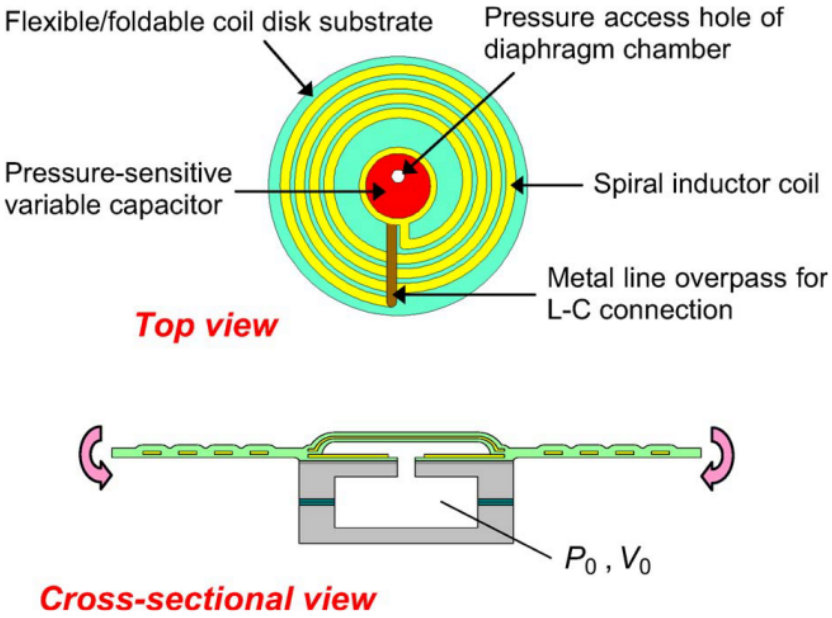

Figure 6.7: *Top view and cross-sectional view of Chen's pressure sensor design [47]*

Alternative approach for passive pressure sensor

Further, Baldi *et al.* [52] studied an alternative approach for passive pressure sensor. Rather on using a LC resonator, this group studied a sensor design that consisted in a single pressure-sensitive inductor. By using a single component for the sensor, the packaging and encapsulation was simplified.

The sensor looked like a capacitor; the analog of the upper electrode was a flexible membrane holding in its center a piece of ferrite core and the analog of the bottom electrode was a planar coil. To separate these structures and form a cavity, spacers made of glass were used. This sensor structure is depicted in Figure 6.8. In order to achieve good sensitivity, the material used for the flexible membrane was silicone rubber, which has a Young's modulus of 1.18 MPa and can elongate more than 750%, thus can produce large deflections when applying low pressures to it [52].

The operation principle of the sensors is that when pressure is applied to the membrane, the ferrite gets closer to the coils, producing a higher value of inductance and decreasing the resonant frequency of the sensor. Thus, the change in impedance caused by change in the resonant frequency can be calculated from an external coil using the phase dip technique, see Figure 6.9 (a). The pressure applied can be obtained from the magnitude of the phase dip at the resonant frequency [52]. Finally, figure 6.9 (b) shows the change in resonant frequency at different pressures [52].

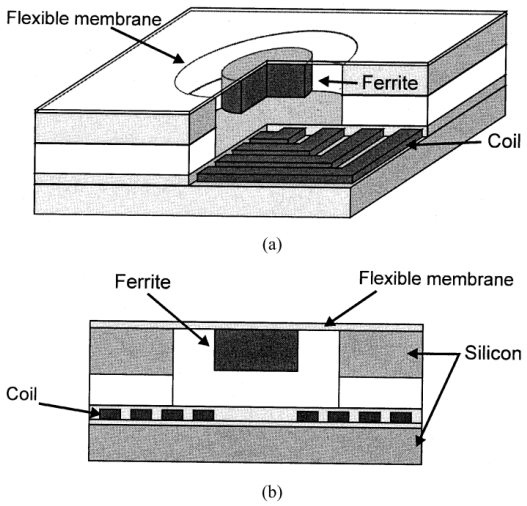

Figure 6.8: *(a) Overview of the sensor structure, (b) cross-sectional view of the sensor structure [52]*

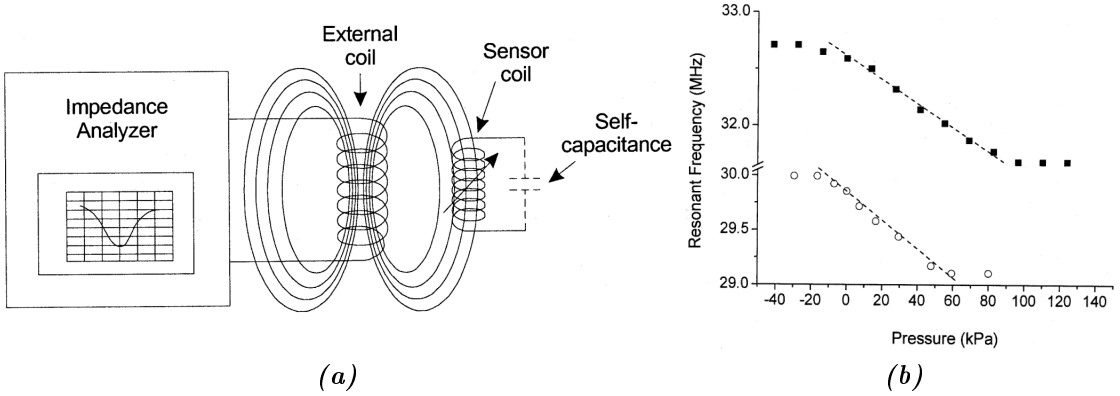

Figure 6.9: *(a) Scheme of the measurement technique, (b) Resonant frequency vs. pressure, black squares represent the measured data and the circles represent the estimated response of the sensor [52]*

Comparison of different sensor structures

Before different passive resonance sensors were described. These sensors were developed for different applications and pressure ranges. Next, a comparison of their characteristics is presented on Table 6.1.

Table 6.1: *Comparison of different passive resonant sensors*

Sensor	Application	Sensitivity	Pressure range	Resonance frequency	Reading method
Collin´s sensor [48], year 1967	Glaucoma application	1 MHz/mmHg	0-100 mmHg	≈120 MHz	absorption of electro-magnetic energy
Baldi *et al.* sensor [52], year 2003	Biomedical applications	1.28 kHz/mmHg	-75 mmHg-600 mmHg	≈32.5 MHz	phase dip technique
Fonseca *et al.* [50] sensor, two configura-tions:for acute and chronic use with different substrate materials, year 2006	measurement of pressure into the aorta	Sensor for acute use from -1 to 20 kHz/mmHg Sensor for chronic use -0.5 to -1.5 kHz/mmHg	12 to 37 mmHg in vivo mea-surement with acute sensor	between 30-50 MHz with different substrate materials	phase locked loop
Fonseca *et al.* [51], year 2002	Applications for high tempera-tures	0.188 kHz/mmHg	0-5250 mmHg	≈17 MHz	phase dip technique
Chen *et al.* [47], year 2010	Glaucoma application	243 kHz/mmHg	0-100 mmHg	≈350 MHz	phase dip technique

7. SENSOR MODELS

This chapter describes the models constructed in COMSOL Multiphysics. These models were built to study the behaviour of the sensors. First, the structure and operation principle of the sensor chosen for this work are introduced. Then, the three and two dimensional models of the sensors are described.

7.1 Structure and operational principle of the sensor

For this work the sensor was chosen to be a passive resonance sensor. The structure of the sensor consists of a membrane with an electrode located on the top of a printed circuit board (PCB). The PCB consists of a square coil, two electrode plates and a capacitance connected in parallel with the coil. The electrode located in the membrane and the electrodes located in the circuit board form a capacitor. This capacitor is connected in parallel with the capacitance of the PCB. Finally, the formed capacitor and the coil of the PCB form a LC circuit. The structure of the sensor is shown in Figure 7.1.

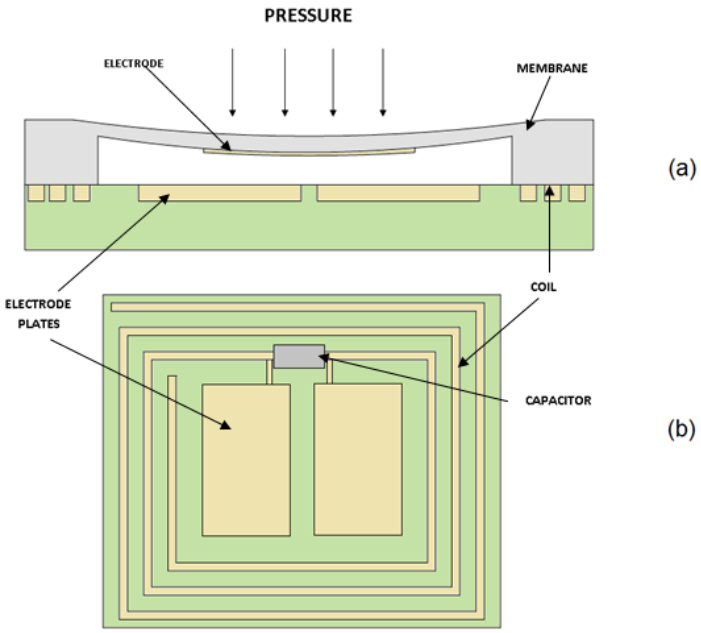

Figure 7.1: *(a) cross-sectional view of the sensor showing the deflection of the membrane with pressure, (b) top view of the circuit board*

The operation principle of the sensor is that when pressure is applied to the membrane, the electrode in the membrane gets closer to the electrodes located in the circuit board. Thus, the capacitance between the two electrodes on the PCB and the electrode of the membrane changes depending on the amount of pressure applied to the membrane.

7.2 Three-dimensional model

A model of the sensor was developed using COMSOL Multiphysics modelling software version 4.1 in order to study the effect of different membrane dimensions on the sensor behavior. COMSOL Multiphysics uses finite element analysis (FEA) to solve partial differential equations (PDEs) that describes the physics of the model.

The constructed model was three dimensional and was set to be an stationary state study. The model consisted of different physics interfaces i.e. electrostatics, solid mechanics and moving mesh feature.

The deflection of the membrane is modelled by the solid mechanics interface and the capacitance is calculated using electrostatics physics interface. These physics interfaces are described briefly in Appendix B and C. Moving mesh was used to deform the mesh according to the displacement of the membrane.

Three different materials were defined with their physical properties relevant to the physics of the model. These properties are shown in Table 7.1.

Table 7.1: *Materials properties*

Material properties used in the COMSOL Multiphysics model	
Material	Properties
PDMS	Young´s modulus 1.85MPa, Poisson ratio 0.4999
Structural steel	Young´s modulus 200GPa, Poisson ratio 0.33
Air	Relative permittivity 1

The model of the sensor consists of three electrodes and a PDMS membrane, shown in Figure 7.2. Two electrodes are located in the PCB and the third electrode is located on the PDMS membrane.

In order to simulate the capacitance between the electrodes, a box with the dimensions of the gap between the electrodes is set as air, see Figure 7.2. The electrode in the membrane is set at 0 volt potential and only one of the electrodes of the PCB is set at 1 Volt potential. This is done because in the real PCB the electrodes are at different potential, forming two capacitors in series as shown in the electrical representation of the sensor, see Figure 7.3.

The resonance frequency was calculated by using the modeled capacitance (C_s),

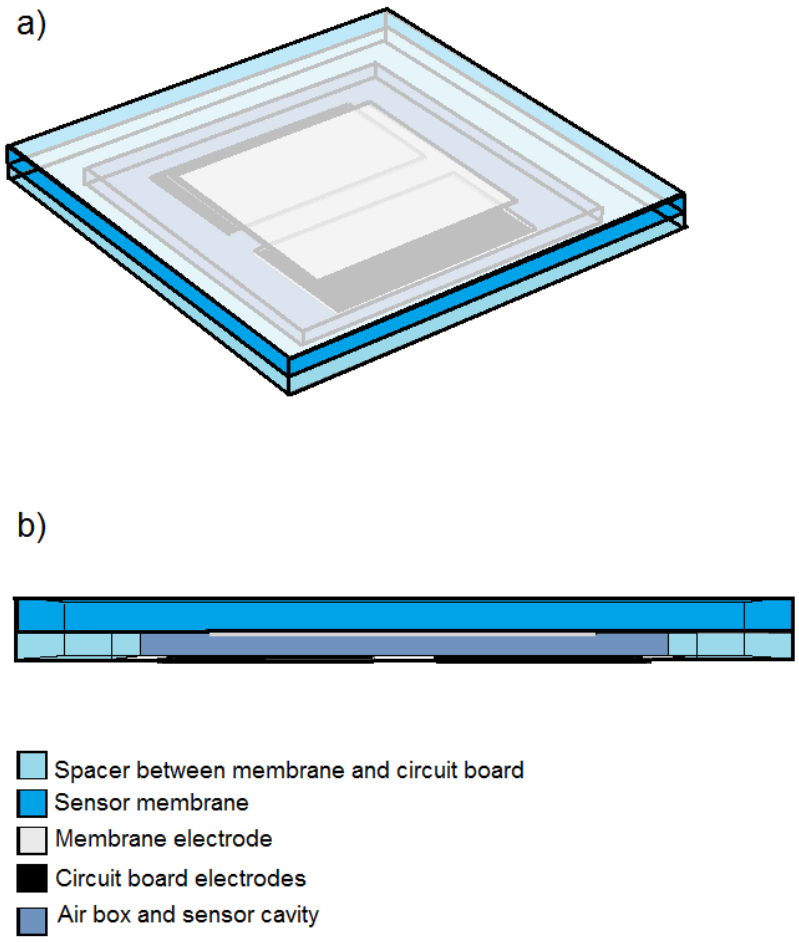

Figure 7.2: *Sensor geometry and construction, a) top view of the sensor showing the blocks used in the model, b) transversal view of the sensor geometry*

the value of the capacitor located in the PCB (27 or 22 pF) and the fixed value of inductance that is 0.222 μH.

$$f = \frac{1}{\sqrt{(C_s/2 + C_{PCB}) \times L} \times 2\pi} \tag{7.1}$$

where f is resonance frequency , L is the inductance and the C_{PCB} is the capacitor located in the PCB.

Next, an example of the displacement of the membrane due to pressure is shown in Figure 7.4 and in Figure 7.5 is shown the electric field between the electrodes. It can be seen in these Figures that the membrane deforms in a way that the electrode is also deformed. The electrode does not move paralell to the electrodes located in

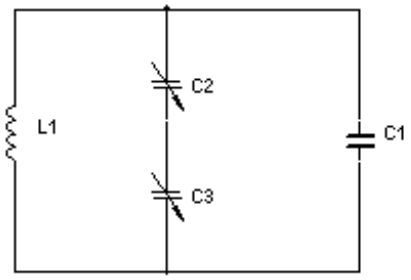

Figure 7.3: *Electrical representation of the sensor. L1 represents the coil and C1 the capacitor located on the PCB. C2 and C3 represent the capacitors formed by the electrodes located in the PCB and the membrane electrode*

the PCB and thus the electric field is not uniform.

Finally, Figure 7.6 shows another view of the deflection of the membrane due to pressure. From this Figure it can be observed that the displacement of the membrane is greater at the center of the membrane.

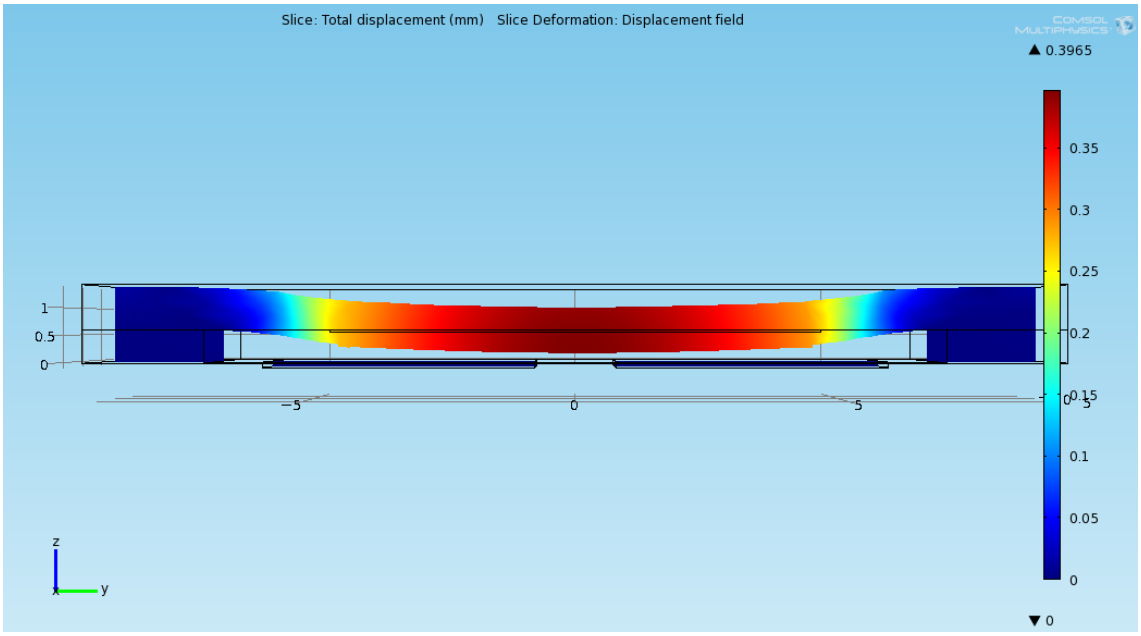

Figure 7.4: *Cross-sectional view of the membrane displacement due to pressure*

Different geometries were modeled using this three dimensional model, however only two of them were constructed as prototypes. The geometry of the modelled constructed sensors are shown in Figure 7.7 and Figure 7.8. The distance between the membrane electrode and the PCB electrodes in the first design is 0.57 mm and in the second design is 0.55 mm.

For the first design, the range of pressure was from 0 to 50 mmHg and for the second design in the range of 0 to 65 mmHg. The calculated capacitance and

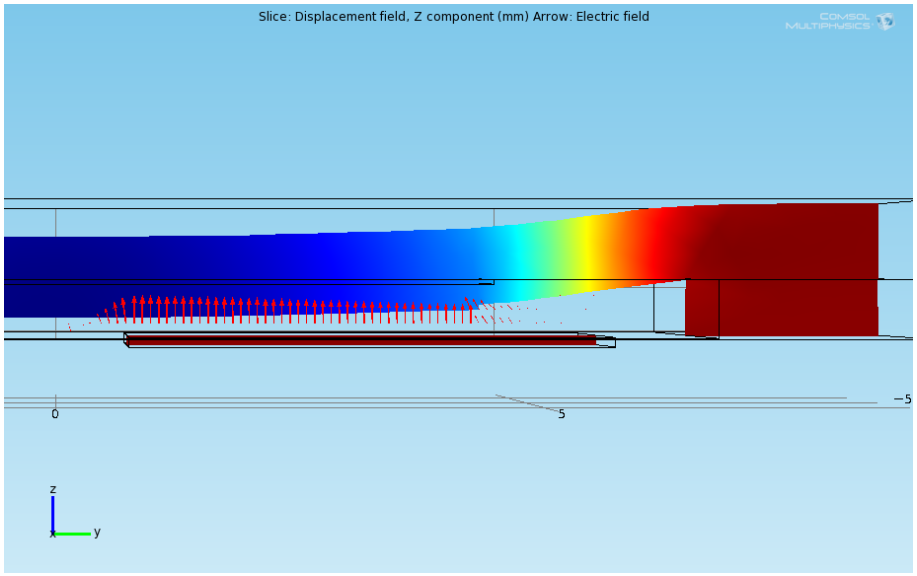

Figure 7.5: *Cross-sectional view of the electric field between the electrodes*

frequency as a function of pressure of both modelled sensors are shown in Figure 7.9. In the Figure 7.9(a) the latest results of the model were removed because showed a large variation and was difficult to observe the results at smaller pressures. The removed values for frequency was 56 MHz and for capacitance was 9.38 pF. The reason of these variations could be that the displacement of the membrane cross or touch the electrodes of the PCB and this is not taken into account in the model. Thus, might be that this capacitance calculation is not correct when the deformation of the membrane is too large. Another explanation might be that the deformation of the mesh is not of good quality, thus gives wrong results. It is important to mention that even though the distance between electrodes is smaller in the second design, the initial capacitance in the results is lower than in the first design. This can be due to the difference between the number of mesh elements between the two models. Also, because in the first design the electrode thickness is 30 μm and in the second is 50 μm the size of the mesh is different in the two electrodes.

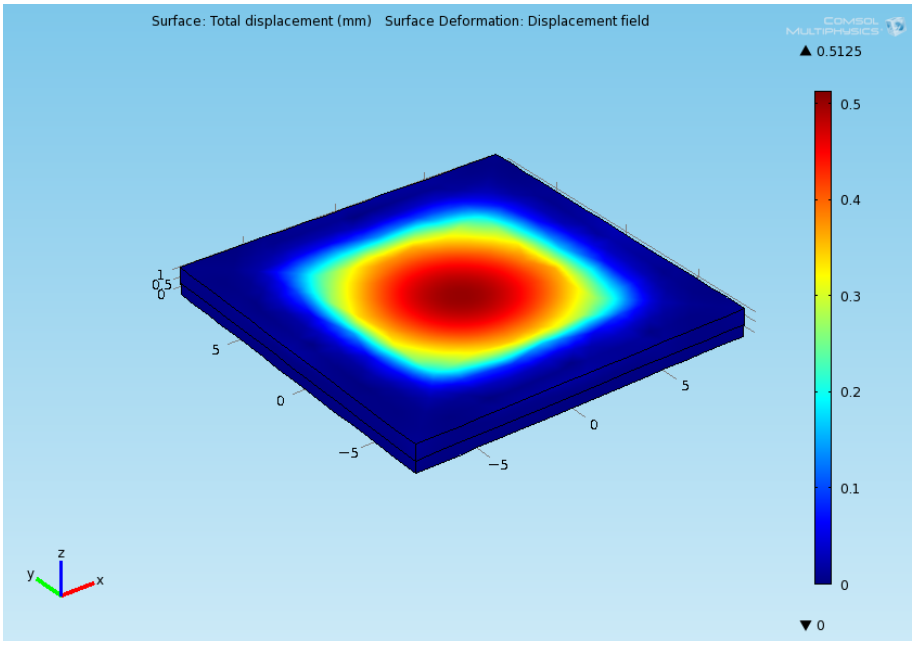

Figure 7.6: *Three dimensional view of the displacement of the membrane due to pressure*

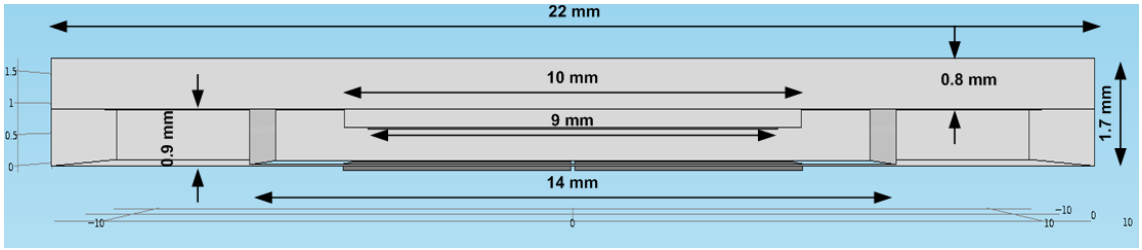

Figure 7.7: *Geometry of the first design*

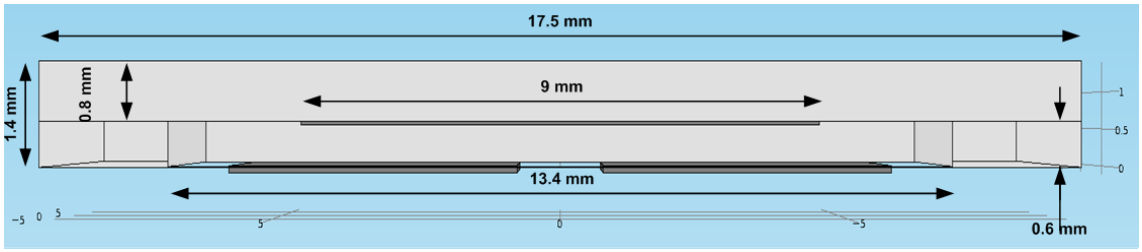

Figure 7.8: *Geometry of the second design*

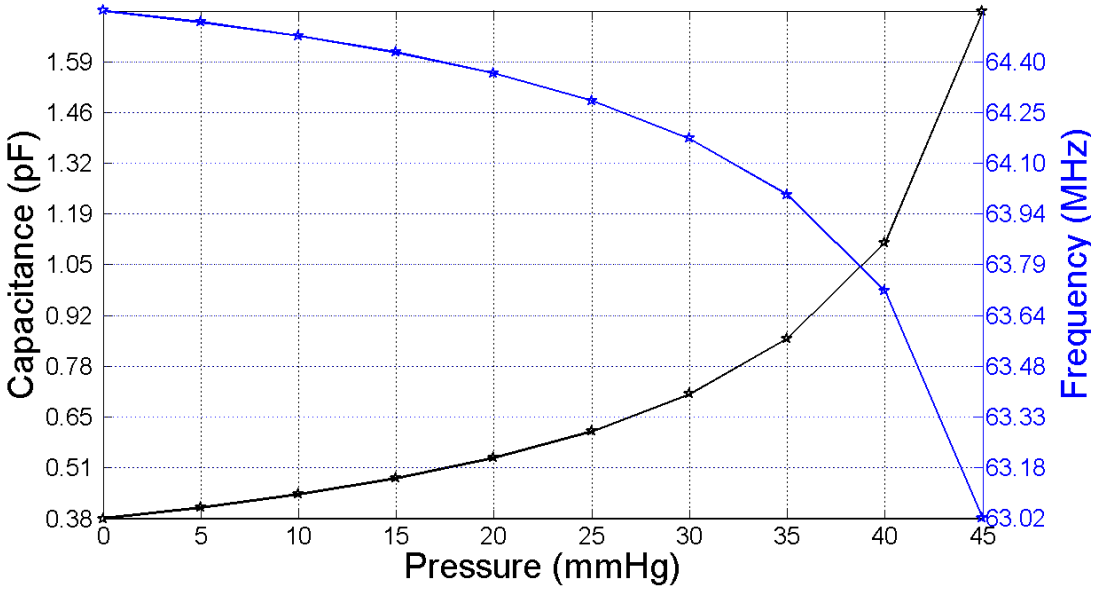

(a) Results of capacitance and frequency of the first designed sensor

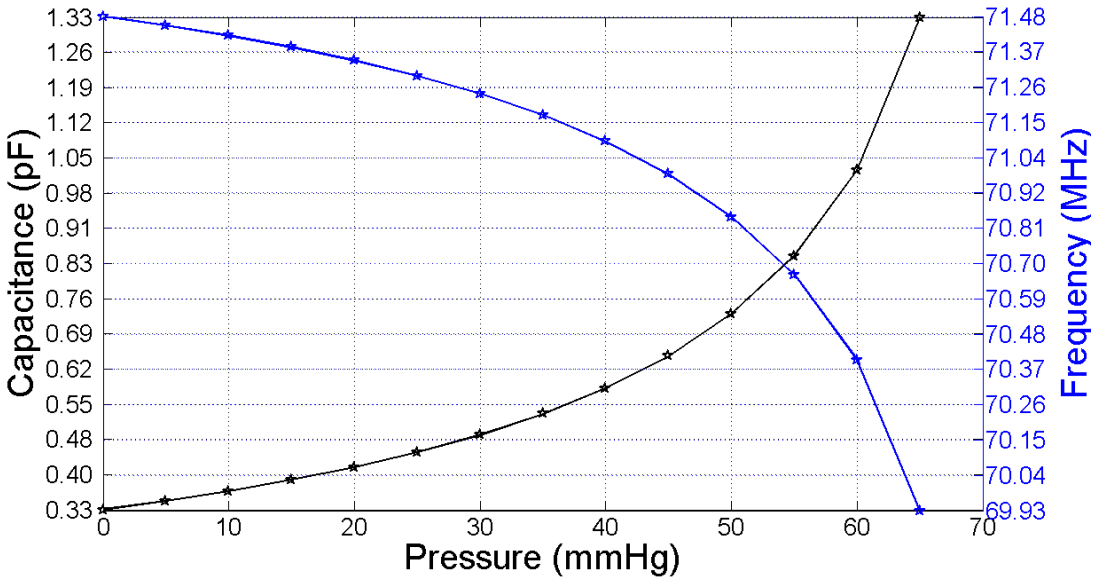

(b) Results of capacitance and frequency of the second designed sensor

Figure 7.9: *Calculated capacitance and frequency with the three-dimensional model*

7.3 Two-dimensional model

In order to model the last design with a bossed membrane a two dimensional model was constructed. For this model, only the mechanics interface was used. The reason for using only mechanics interface is that since the membrane is a bossed structure, the thickness of the boss in this design is 11.7 times the thickness of the membrane, and thus it can be assumed that the electrode in the boss moves parallel to the electrodes located in the circuit board when pressure is applied to the membrane. In this case the capacitance can be calculated with the equation of parallel plate capacitor:

$$C = \frac{\epsilon_r \epsilon_0 A}{d} \tag{7.2}$$

where C is the capacitance, ϵ_r and ϵ_0 are the relative permittivity of the material and the vacuum permittivity respectively, A is the area of the overlap of the electrodes and d is the distance between the parallel electrodes. Thus, using the mechanics interface the displacement of the center of the boss was computed and then using the equation of parallel plate capacitor the change in capacitance due to pressure was calculated.

The geometry of this model is shown in Figure 7.10, the thickness of the membrane is 100 μm, the thickness of the boss is 1.17 mm, the thickness of the boss electrode is 0.03 mm and the distance between the boss electrode and the circuit board electrodes (not modelled) is 0.4 mm.

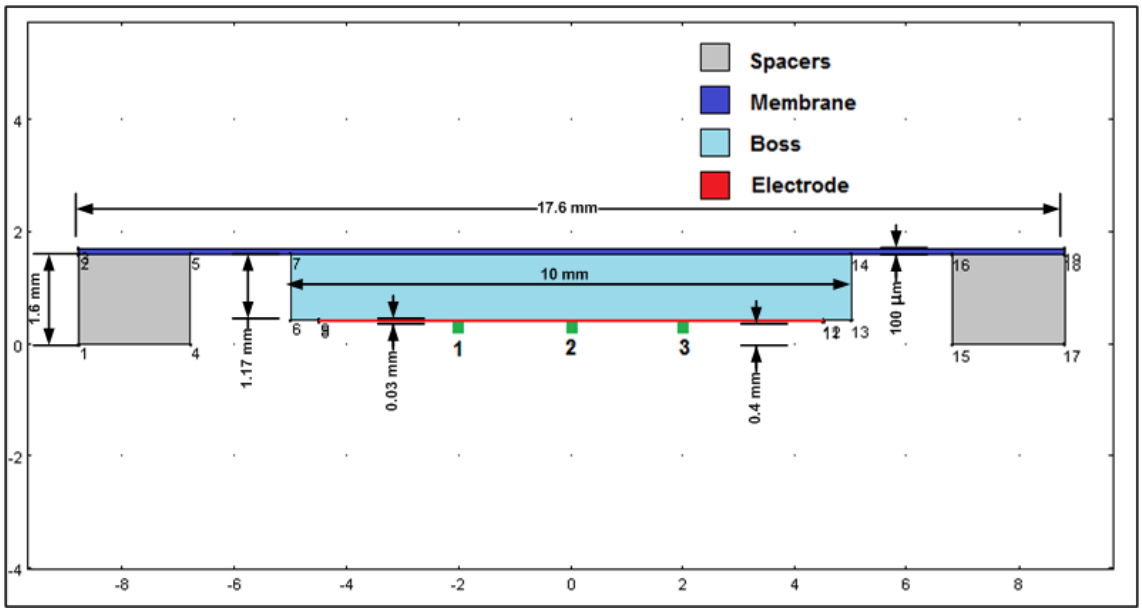

Figure 7.10: *Geometry of the two-dimensional model . The green points located in the membrane are used to study the displacement of the membrane*

The material for the electrode was structural steel with a Young's modulus of

200 GPa and a Poisson's ratio of 0.33. The material for the boss and spacer was PDMS with a Young's modulus of 1.85 MPa and a Poisson's ratio of 0.4999. For the membrane the Young's modulus and Poisson's ratio were assumed to be 200 GPa and 0.33, respectively. These values were estimated because the material used for the membrane for the prototype was transparency film and the mechanical values of this material were not possible to obtain.

In the Figure 7.11 the displacement of the membrane at a pressure of 65 mmHg is shown with a scale factor of 4, the color legend shows that the maximum deflection is 0.1618 mm. It is important to notice that the spacers do not show any displacement. In addition, the deflection of three points located in the membrane electrode, see the points in green in Figure 7.10, are shown in Figure 7.12. In this Figure it is observe that the membrane is bending, since there is a difference in the displacement of the points located in the membrane (see Figure 7.10). Finally, the resulted capacitance and frequency are shown in Figure 7.13. This linear result was expected, since the change in distance between the electrodes is small.

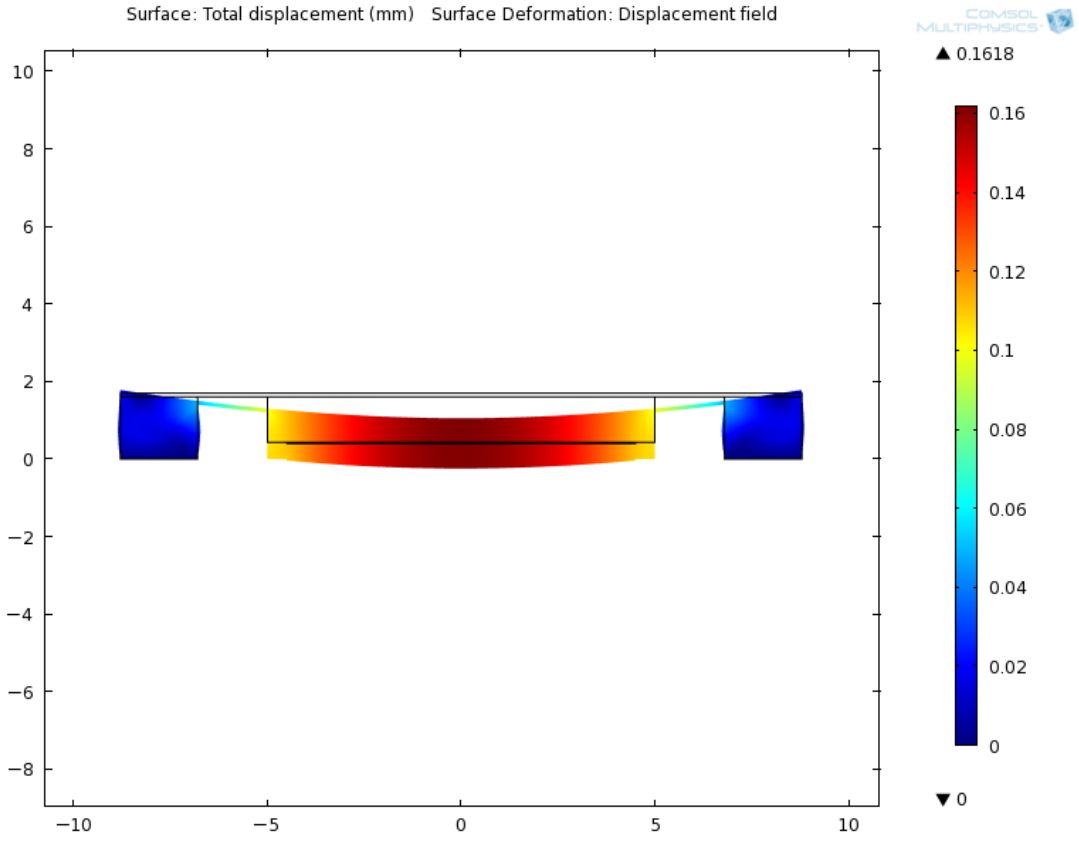

Figure 7.11: *Displacement of the membrane at 65 mmHg with a Young's Modulus value of 200 GPa and a scale factor of 4*

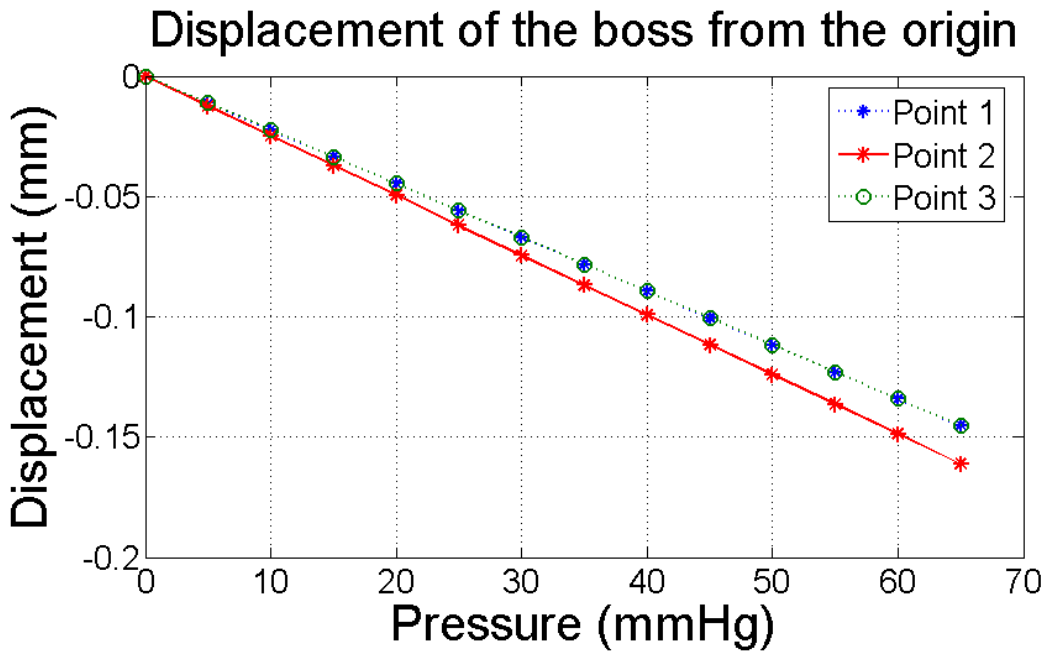

Figure 7.12: *Displacement from the origin of the three green points located in the electrode of the membrane*

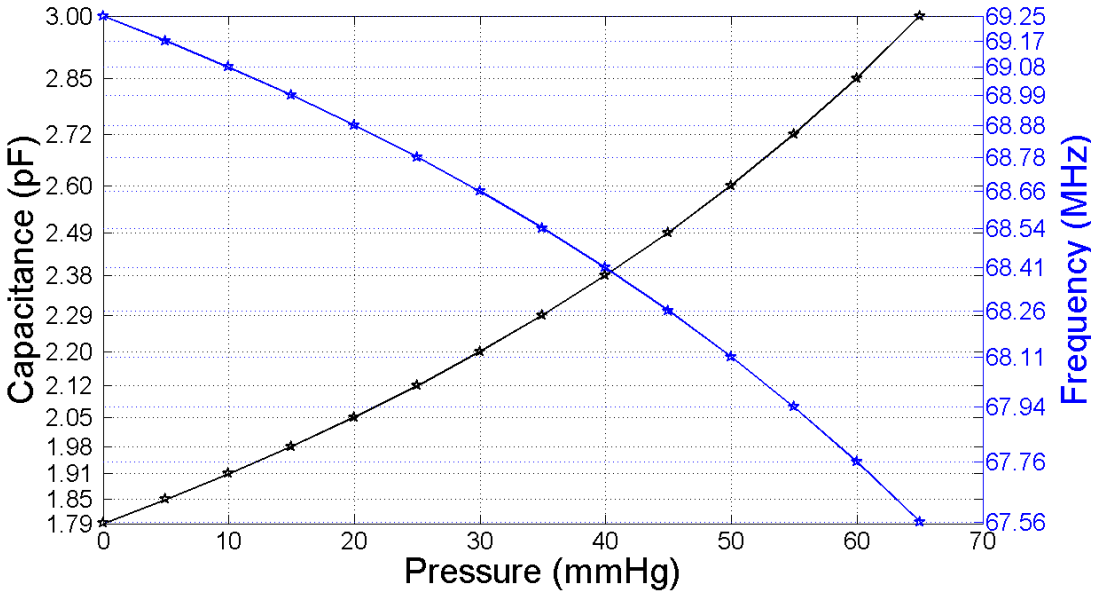

Figure 7.13: *Calculated capacitance and calculated frequency change using the equation of the parallel plate capacitor*

8. CONSTRUCTION OF PRESSURE SENSORS PROTOTYPES

The constructed sensors consisted of a PDMS membrane with an electrode and a printed circuit board which is composed of a coil, two electrode plates and a capacitor of 27 or 22 picofarads, see Figure 8.1. The operational principle of the sensor is that when the membrane is deflected due to the pressure applied to it, the electrode located at the membrane gets closer to the electrodes located on the circuit board and thus the capacitance increases. In the circuit board, the capacitance and the coil forms an LC circuit, so, when the capacitance change, a resonance frequency shift is produced. The shift in resonance frequency is detected by an inductively coupled external coil and by detecting the drop of the equivalent impedance phase, see Appendix A.

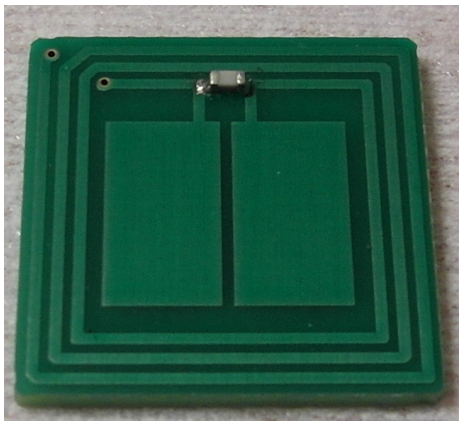

Figure 8.1: *Printed circuit board*

8.1 Construction procedure

In this section the procedure for the preparation of the prototypes is explained. First, the preparation of the PDMS membrane is described and then the procedure for the preparation of the electrode and gluing is explicated. Finally, the construction of the bossed membrane using transparency film is described.

8.1.1 Preparation of PDMS membrane

To prepare the PDMS polymer, a polymer Sylgard 184 silicone elastomer curing agent and Sylgard 184 silicone elastomer base were used. First, the curing agent and the elastomer base were mixed with a proportion of 10:1 of elastomer base to curing agent. Thus, for example, 1 gram of curing agent was weighted and then 10 grams of elastomer base was added and mixed. The two parts were mixed using a plastic spoon during approximately 5 minutes in a plastic cup. To remove the bubbles formed in the polymer solution a vacuum chamber was used. The polymer solution was introduced into the vacuum chamber, and then the air was removed. This step was repeated several times, until almost all the bubbles were removed.

To prepare the membrane, the polymer was poured into a mould. Then, the mold was introduced into the vacuum chamber to remove the bubbles formed during the pouring of the polymer. When almost all the bubbles were removed the mold with the polymer was removed from the vacuum chamber. A small piece of transparency film was used as lid. First, a little amount of polymer was poured into the transparency film, and again was put inside the vacuum chamber to remove the bubbles. Then, the transparency film was carefully put like a lid in the mold. Finally, some weight was put on the top of the film and mold and these were introduced into an oven at 65 °C for two hours. After two hours, the membrane was removed from the mold.

8.1.2 Preparation of the metal sheet and gluing to the PDMS membrane

The electrodes were formed by cutting small pieces of metal sheet. The cutting was done with scissors. First, a small square was drawn using a pencil and a ruler to form a 9 mm square length. Then, using scissors the square was cut and then it was measured to ensure the correct length. To reduce the curvature formed in the small metal square after cutting with scissors some weight was added, however some curvature remained.

The electrode was glued to the membrane using uncured PDMS. First, a small piece of transparency was cut in order to use it like an spatula. A small amount of uncured PDMS was picked using the transparency piece, and then it was spread into the square metal sheet. Using a pair of tweezers the metal sheet was carefully placed in the middle of the membrane. Then, a small weight was added to the electrode to press the metal sheet against the PDMS membrane and ensure the gluing. The gluing of the metal sheet and membrane was left overnight.

Figure 8.2(a) shows the PDMS membrane of the first design and Figure 8.2(b) of the second design with the metal sheet as electrode. Finally, the membrane

with the electrode was glued to the PCB using uncured PDMS. Using the piece of transparency as spatula, a small amount of uncured polymer was spread into the corners of the PCB. Using tweezers, the membrane was carefully placed on the top of the PCB. Pressure was added to the membrane in order to ensure the gluing of the membrane to the PCB, and then was left overnight.

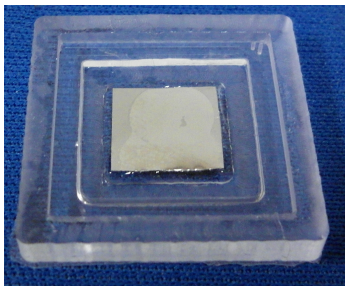

(a) First design

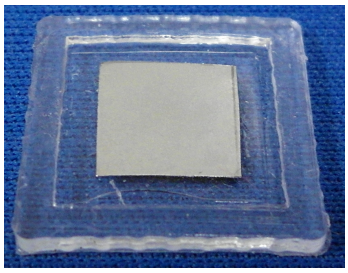

(b) Second design

Figure 8.2: *The PDMS membranes with electrodes*

8.1.3 Preparation of the bossed transparency membrane

First, a PDMS membrane was prepared following the same procedure described before. The mold used had a thicker portion on the center of the membrane as the mold used for the preparation of the membrane shown in Figure 8.2(a). Using the PDMS membrane and a scalpel the thicker portion of the membrane (located in the center) and the borders were cut. In this way, it were obtained a boss and a square spacer (hollowed square), see Figure 8.3(a).

Then, using a transparency sheet, a square of 17.6 mm length was cut using scissors. Then, the boss was glued in the middle of the transparency film square using uncured PDMS, as shown in Figure 8.3(b). To assemble the membrane, the hollowed square was glued with uncured PDMS to the transparency film with the boss. Finally, the preparation and gluing of the metal sheet and gluing of the membrane to the PCB was done as described before. Figure 8.3(c) shows the boss with electrode without the spacers.

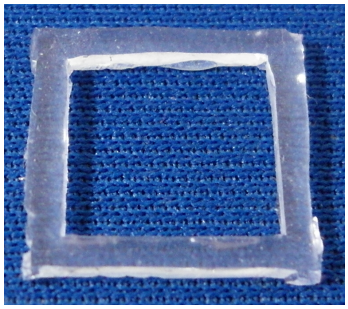

(a) Spacers, hollowed PDMS square

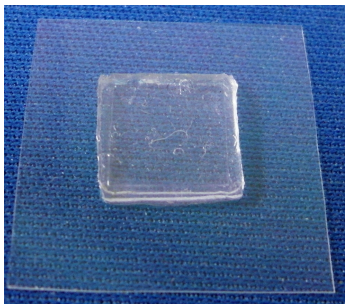

(b) Boss and transparency film

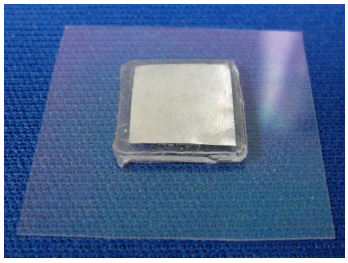

(c) Boss with electrode

Figure 8.3: *Different parts of the transparency film membrane*

8.2 First sensor design

The first membrane design had the dimensions depicted in the Figure 8.4:

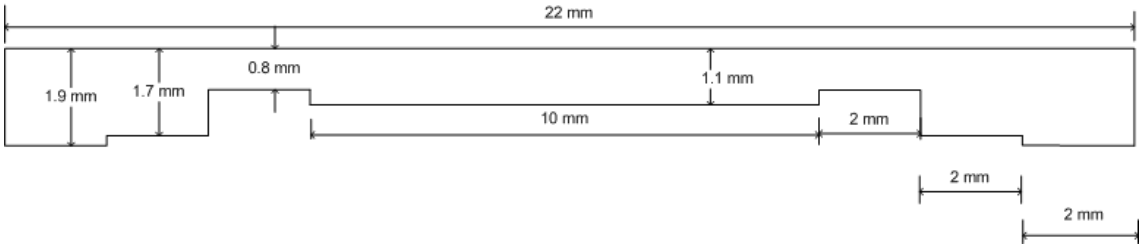

Figure 8.4: *The first design of membrane geometry*

The membrane was thicker in the center with a thickness of 1.1 mm. The PDMS membrane had also another space with the dimensions of the circuit board, in order to place it inside the membrane. The circuit board and the membrane were glued using uncured PDMS. The electrode was a 9 mm square steel sheet with thickness of approximately 30 μm. The electrode was also glued to the membrane using uncured PDMS. A picture of the final sensor is shown in Figure 8.5.

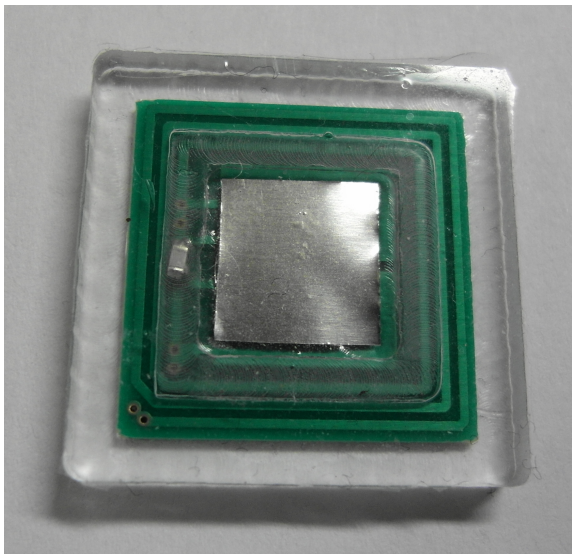

Figure 8.5: *Constructed sensor, first design*

8.3 Second sensor design

The second constructed sensors consisted of a PDMS membrane with an electrode and a circuit board which is composed of a coil, two electrode plates and a capacitor of 22 picofarads.

The second membrane design had the dimensions depicted in Figure 8.6:

The circuit board and the membrane were glued using uncured PDMS. The electrode was a 9 mm square steel sheet with thickness of approximately 50 μm. The

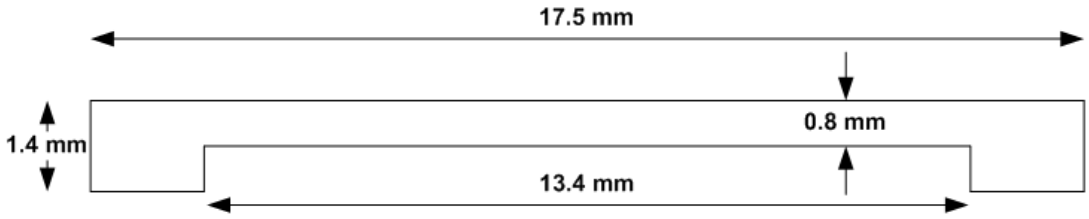

Figure 8.6: *Second design of the membrane geometry*

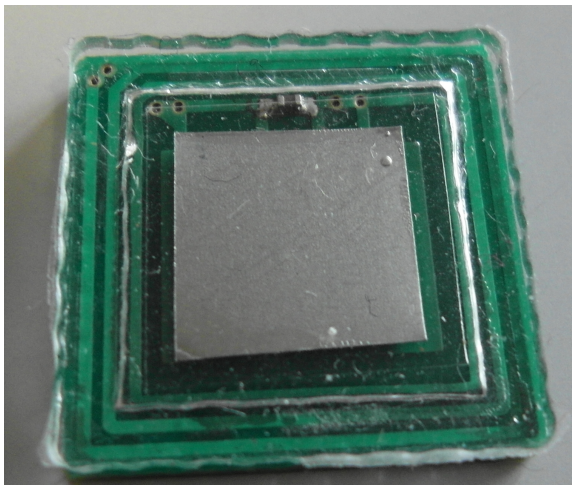

Figure 8.7: *Constructed sensor, second design*

electrode was also glued to the membrane using uncured PDMS. A picture of the final sensor is shown in Figure 8.7

8.4 Third sensor design

The third membrane design consists of a bossed membrane. The circuit board was composed of a coil, two electrodes plates and a capacitor of 27 picofarads. The third membrane design had the dimensions depicted in the Figure 8.8:

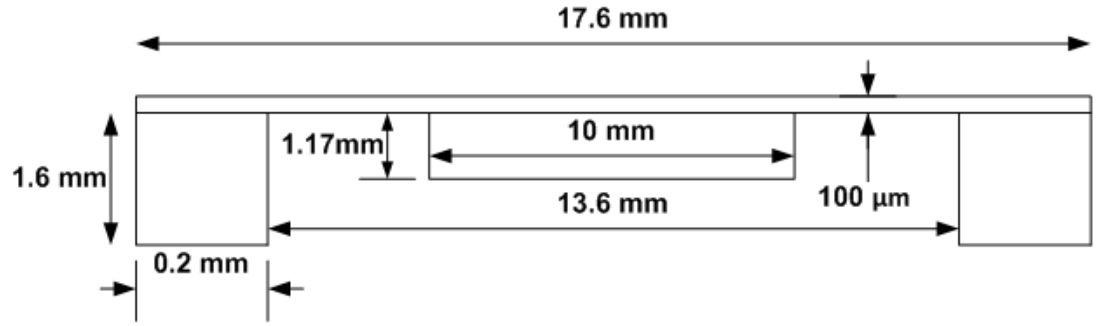

Figure 8.8: *Third design of the membrane geometry*

This membrane is composed of a transparency sheet with a PDMS boss in the

center. The bossed was glued to the transparency sheet using uncured PDMS. The electrode was 9 mm square steel sheet with a 30 μm thickness. A hollowed square made of PDMS was used as spacer in order to form the cavity between the bossed membrane and the circuit board. A picture of the final sensor is shown in Figure 8.9

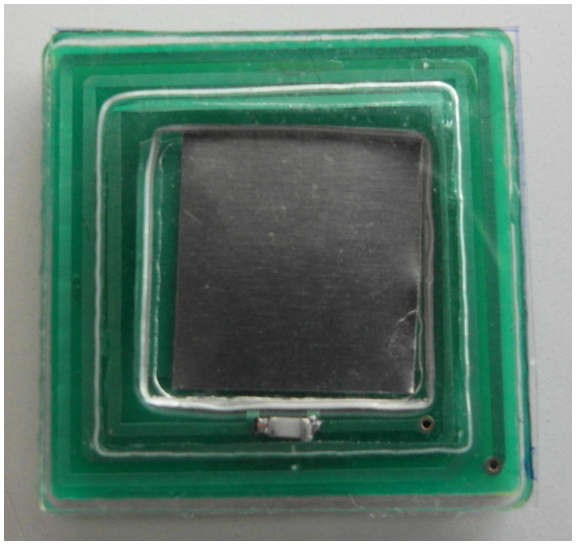

Figure 8.9: *Constructed sensor, third design*

9. MEASUREMENTS WITH THE CONSTRUCTED SENSORS

The resonance frequency shift due to pressure applied to the pressure sensors was measured. Pressure was applied to the prototypes in steps of 5 mmHg from 0 to 50 for the first design and to 65 mmHg for the second and third design. The resonance frequency was measured using a reading device with a coil. The coil of the reading device and the coil of the sensor are inductively coupled and thus the resonance frequency can be detected.

The measurements were performed using a pressure regulator and a measurement configuration to exert pressure over the sensor, this shown in Figure 9.1. This configuration consists of a jar, a rubber membrane (rubber glove), a plastic recipient and duct tape, this used to fix the jar to the recipient. Further, the jar is connected to the pressure regulator by a plastic tube and the rubber membrane is placed in the jar as a lid and is tensioned. Then, the sensor is placed between the plastic recipient and the rubber membrane, so when the pressure inside the jar increases, the rubber membrane deforms exerting pressure over the membrane of the sensor.

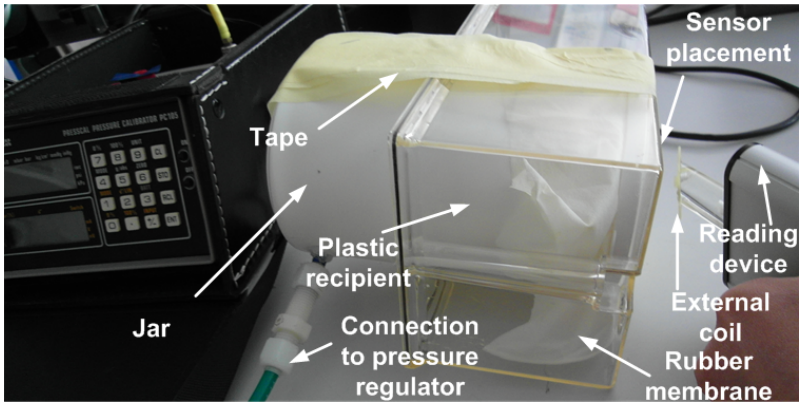

Figure 9.1: *Measurement configuration*

The reading device measures the impedance phase in resonance frequency of the sensor and sends the data to a computer to calculate the resonance frequency. Additionally, a distance compensation developed by Salpavaara *et al.* [53] is used. This distance compensation uses the fact that there is a linear relation between the frequency and height of the phase peak [53].

Further, to measure the sensor, first a calibration reading is needed. For that the

reading device was placed close to the sensor without pressure and moved away in order to obtain a calibration signal, similar to the one shown in Figure 9.2, used later in calculations for distance compensation. In this Figure, it can be seen results of different inductive couplings between the coils of the reading device and the sensor. The height of the dip changes depending on the distance of separation of the two coils. After this, the measurement was performed placing the reading device at a similar distance to the sensor by applying pressure in the ranges of 0 to 50 mmHg for the first designed sensor and 0 to 65 mmHg for the second and third designed sensors with 5 mmHg steps.

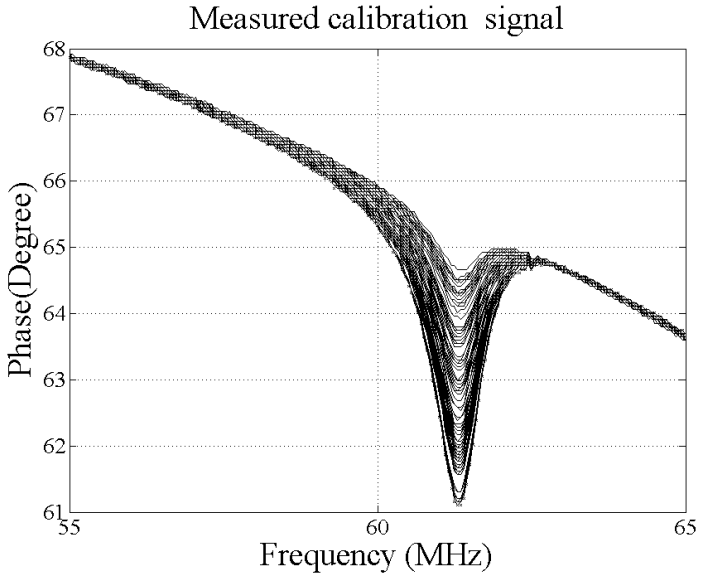

Figure 9.2: *The calibration data. Figure shows the effects of different inductive couplings between the coil of the reading device and the sensor at different distances*

Next, the data obtained is processed to obtain the shift of the resonance frequency due to pressure. Examples of a measured signal and the detected frequency with distance compensation are shown in Figure 9.3. In the Figure 9.3(a), the data measured at an arbitrary applied pressure to the sensor is shown. Even though the reading device was hold at the same distance, there were some changes in the height of the phase dip. In Figure 9.3(b), the sampled detected frequency with distance compensation at that arbitrary applied pressure is shown. The mean of these distance compensated detected frequencies is calculated to obtain a frequency value for that particular pressure load.

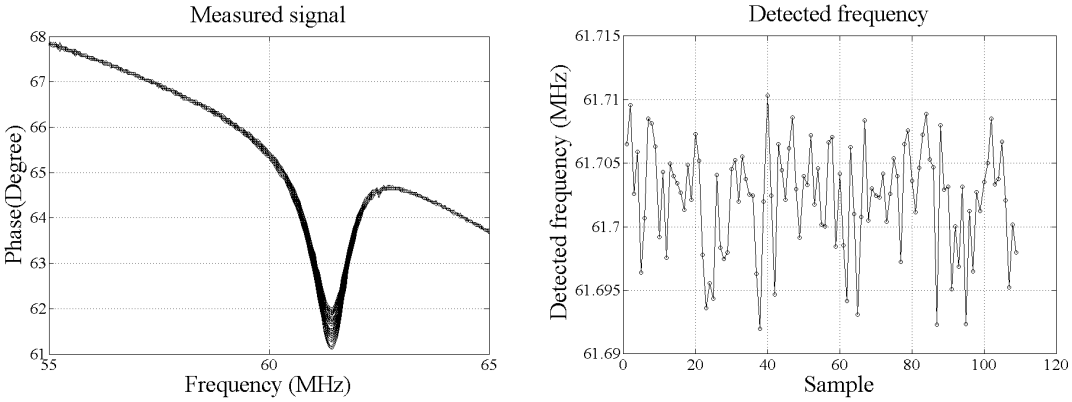

(a) Measured signal

(b) Detected frequency with distance compensation

Figure 9.3: *Processed measured data*

9.1 Measurement with the first sensor design

Five pieces of the first designed sensor were constructed in order to compare them. However, only in four of these it was possible to obtain results since their resonance frequency was in the range of the reading device (10 - 80MHz). From the fifth sensor it was not possible to obtain a signal, thus it was assumed that the sensor was out of the range of the reading device.

The results of the measurements are shown in Figure 9.4. The results from the constructed sensor one, two and three are between similar ranges, around 60 MHz to 61.7 MHz. The result of the sensor four is very different from the other results, its sensitivity is very small. The reason for this could be that the electrode got stuck on the PCB.

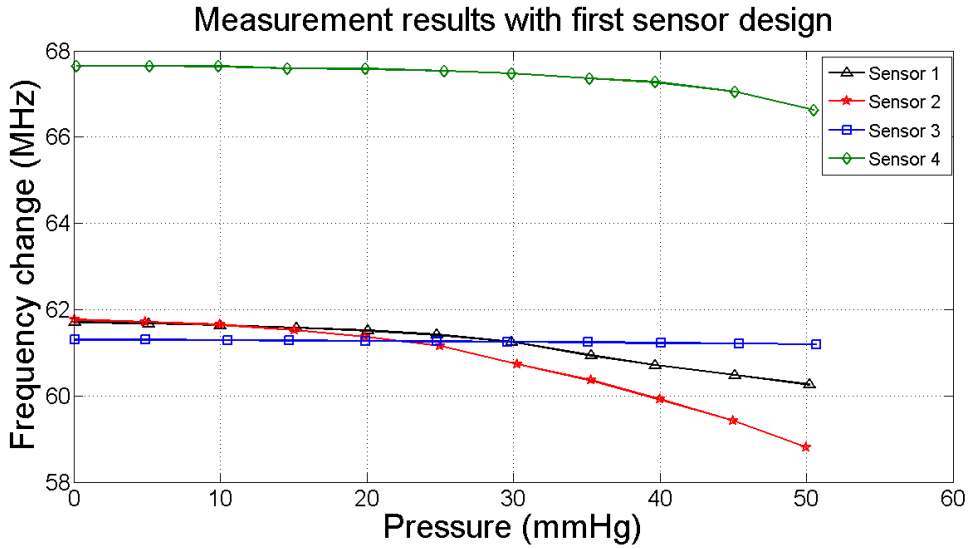

Figure 9.4: *Measurement results with the first sensor design*

9.2 Measurement with the second sensor design

Three sensors of the second design were constructed. The measurement results are shown in Figure 9.5. The frequency range of these constructed sensors was approximately 66 MHz to 75.5 MHz. The sensor 3 shows very low sensitivity. The reason for this might be that the electrode got stuck to the PCB.

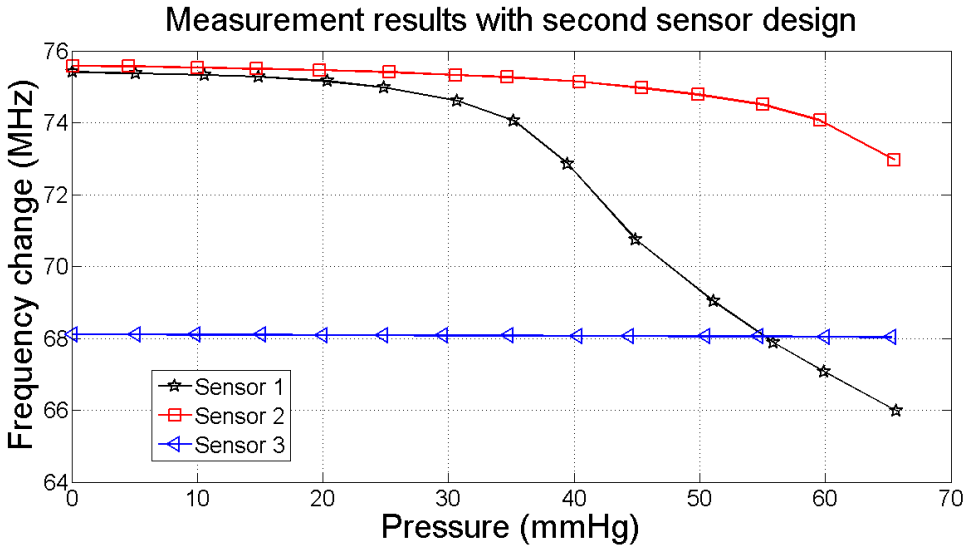

Figure 9.5: *Measurement results with the second sensor design*

9.3 Measurement with the third sensor design

Finally, only two pieces of the third designed sensor were constructed. The measurement results are shown in Figure 9.6. The range of these sensors was approximately 62.2 MHz to 61.8 MHz.

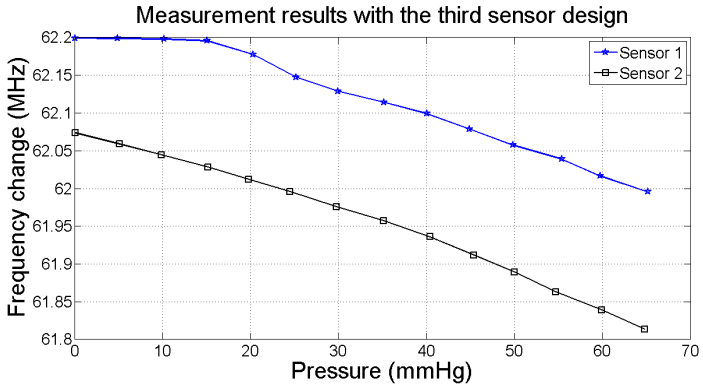

Figure 9.6: *Measurement results with the third sensor design*

10. COMPARISION OF SENSORS

A comparison between the constructed sensors is presented. The Figure 10.1 shows a comparison between the results of the first prototypes of the first design. The removed DC levels for each sensor were 61.7022 MHz for the sensor 1, 61.7595 MHz for sensor 2, 67.6521 MHz for sensor 3 and 61.3038 MHz for sensor 4.

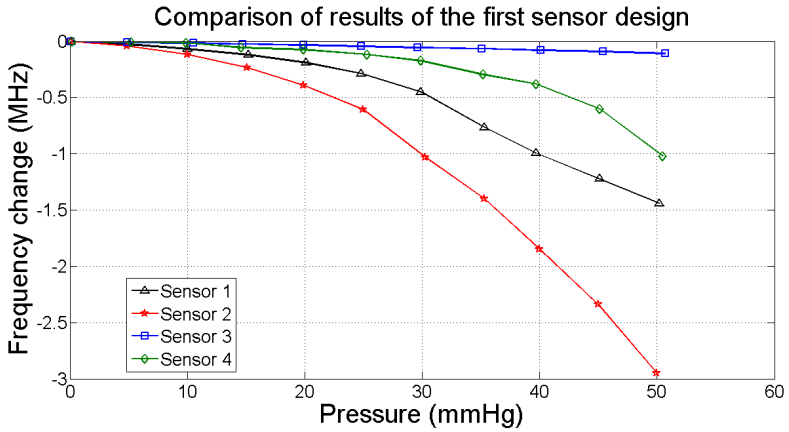

Figure 10.1: *Comparison between the measurement results of the first sensor design*

The results are clearly nonlinear and the sensitivity seems to differ. In the range 20 to 30 mmHg the sensitivity was approximately 26.7 kHz/mmHg, 61.6 kHz/mmHg, 2.2 kHz/mmHg and 10 kHz/mmHg for the sensor one, two, three and four respectively.

The differences in the results between the constructed sensors of the first design could be due to several reasons. The first reason is the misalignment of the electrode in the membrane. The metal sheet was glued to the PDMS membrane using uncured PDMS. Because the polymer was in a liquid form, the electrode moved from the align position when it was left to glue overnight. Even though weight was added to the electrode to ensure the gluing to the PDMS membrane, the polymer in a liquid form produced the slip of the electrode. The second reason is the poor adhesion between the electrode and the PDMS membrane. When the square electrode was cut from a metal sheet, which had a curvature, a small curvature remained in the electrode. This curvature avoided the gluing of the metal to the PDMS, because the corners of the metal square were bending. Also, as mentioned before, it is difficult to bond PDMS to other substrates due to its inertness. Finally, the third reason is the differences during the process of casting the PDMS membrane. In this process

because only one mold was used, the fabrication of the membranes was done during different times. Furthermore, the mixing of the base polymer and curing agent was done also during different times. The amount of curing agent and base polymer was added to a plastic cup by hand using a normal syringe and a plastic spoon. The different quantities were weighted with a weighing scale. For that reason, might be that the amount of curing agent differed in each mixing causing different mechanical properties in the final membrane.

The Figure 10.2 shows the comparison between the results of the constructed sensor of the second design. The removed DC levels for each sensor were 75.4003 MHz for sensor 1, 75.5760 MHz for sensor 2 and 68.1148 MHz for sensor 3.

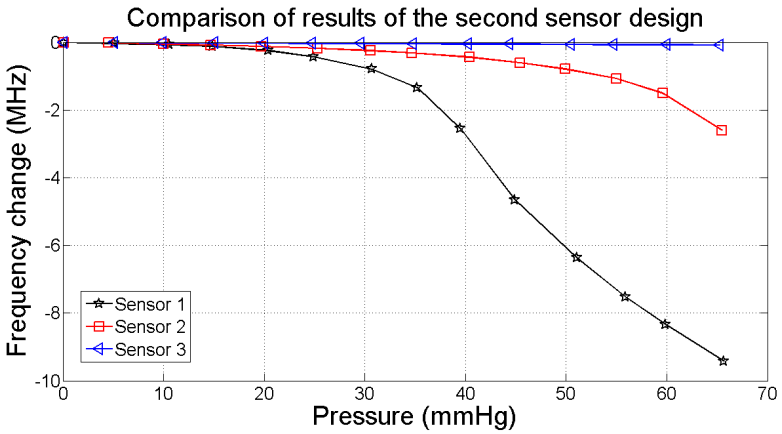

Figure 10.2: *Comparison between the measurement results of the second sensor design*

The results are not linear as it can be observed from the figures and the sensitivity seems to differ in the results, for example in the range from 30 to 50 mmHg the sensitivity was approximately 0.28 and 0.02 MHz/mmHg and 0.0013 MHz/mmHg for the sensor 1, 2 and 3 respectively.

The differences in the results between the constructed sensors of the second design could be the poor adhesion of the metal layer to the PDMS membrane, the misalignment of the electrode and some differences in the casting process since only one mold was used.

The Figure 10.3 shows the comparison between the results of the constructed sensor of the third design. The removed DC levels were 62.1991 MHz for sensor 1 and 62.0737 MHz for the sensor 2. The results seem linear and the nonlinearity was calculated approximately to be between 0.14 to 0.09 MHz and the relative nonlinearity was calculated to be between 37.04% to 69.82% full scale output. The estimated sensitivity was approximately between 3.1 to 4 kHz/mmHg.

The results of the third design are very similar between the two constructed sensors. However, still some differences can be found and again these could be due to the poor adhesion and misalignment of the metal layer to the PDMS membrane.

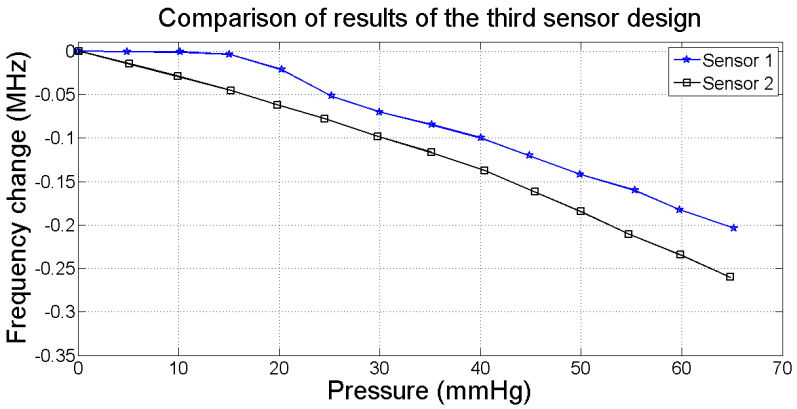

Figure 10.3: *Comparison between the measurement results of the third sensor design*

10.1 Comparison between measurement results and model results

A comparison of the modeled results with the measured results of the prototypes of the first design is presented in the Figure 10.4. In this figure it can be seen that the behavior between the model and the measured results is similar at smaller pressures, however at higher pressures the behavior changes. It is believed that the cause of these differences could be that the membrane electrode in the prototypes touches the circuit board electrodes. In this case the change in capacitance depends on the increment of the area touching the electrodes. The model does not take this into account. In the model, when the membrane displacement is greater than the distance between the electrodes, the membrane goes through the circuit board electrodes. Thus, this can explain the great drops in frequencies at the last pressures in the model results of the first design, see Figure 10.4. Also, when the deformation of the membrane is large, the quality of the mesh decreases producing warnings of inverted mesh element. This apparently is a limitation of the moving mesh feature. Thus, the results given by the model at greater deformations (higher pressures) might not be entirely correct.

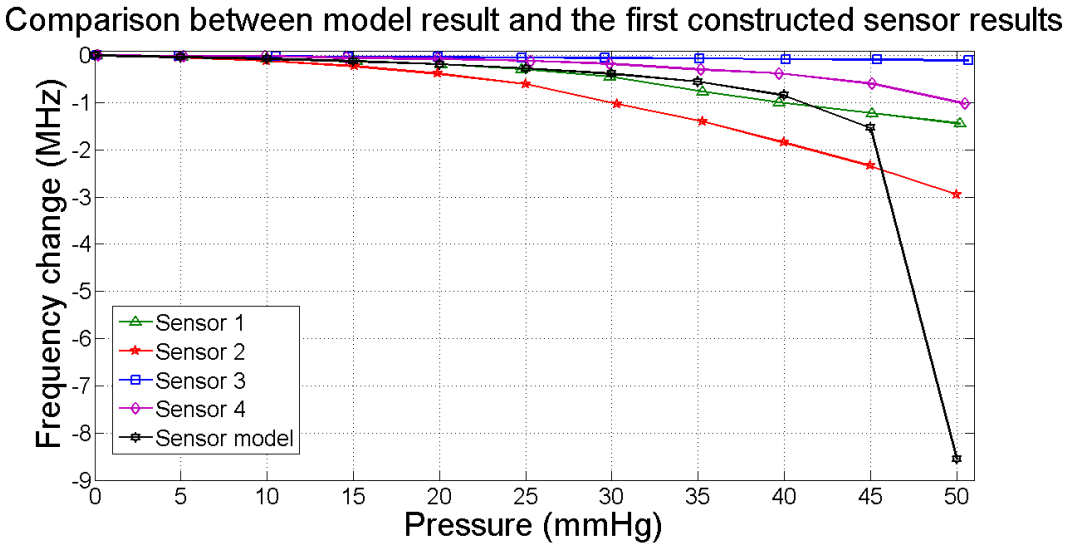

Figure 10.4: *Comparison between the measured results of the first sensor design and the results of the 3D model*

To study the behavior of the model to different Young's modulus (E) values and to the misalignment of the electrode (5°), different simulations were done. These simulations results are shown in the Figure 10.5. The values of the Young's modulus were changed to be ±10% of the PDMS Young's modulus value, i.e. 1.85 MPa. The removed DC level of the simulation results is 64.55 MHz.

As expected, in the Figure 10.5 the same large drops in frequency at higher

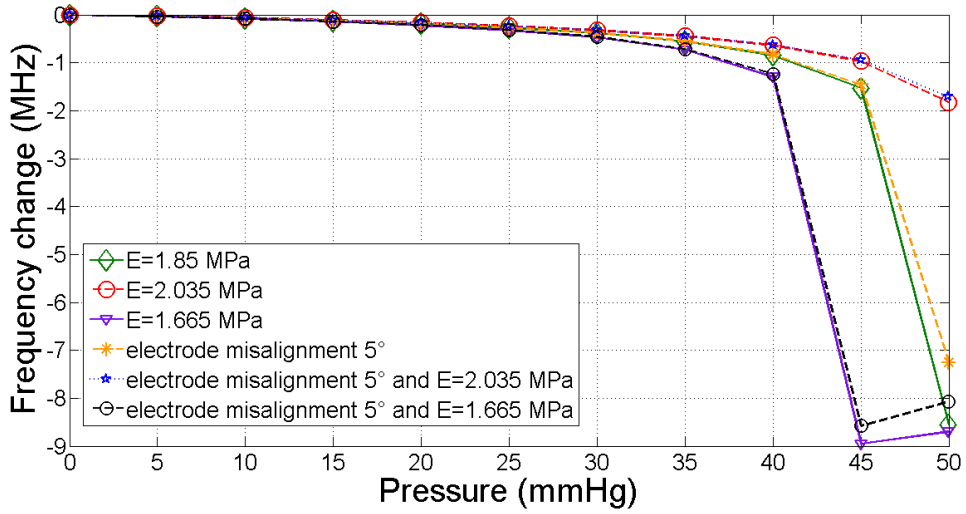

Figure 10.5: *Different simulation results with different Young's modulus values and with misalignment of the electrode*

pressures were obtained. For that reason, in the Figure 10.6 the last results values were removed for better observation of the behavior of the sensor model. In this figure it is observed that the variation in Young's modulus has a greater impact in the results than the misalignment of the electrode.

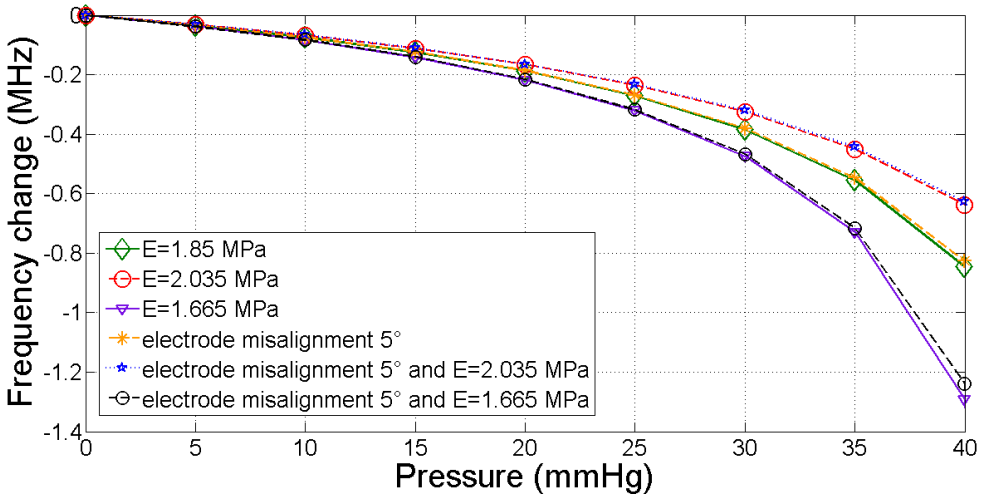

Figure 10.6: *Different simulation results with different Young's modulus values and with misalignment of the electrode without the large drops of frequency*

These modified simulations could be used to explain the differences between the measured results of the constructed prototypes of the first design. In the Figure 10.7, the measured results of the prototypes and the results of the modified simulations are shown together. Thus, discarding the last results of the simulation at higher pressures, see Figure 10.8, the different mechanical properties and the misalignment

of the electrode can explain the different sensitivities found in the measured results. For example, with a Young's modulus value of 2.035 MPa the sensitivity is lower than with a Young's modulus value of 1.665 MPa.

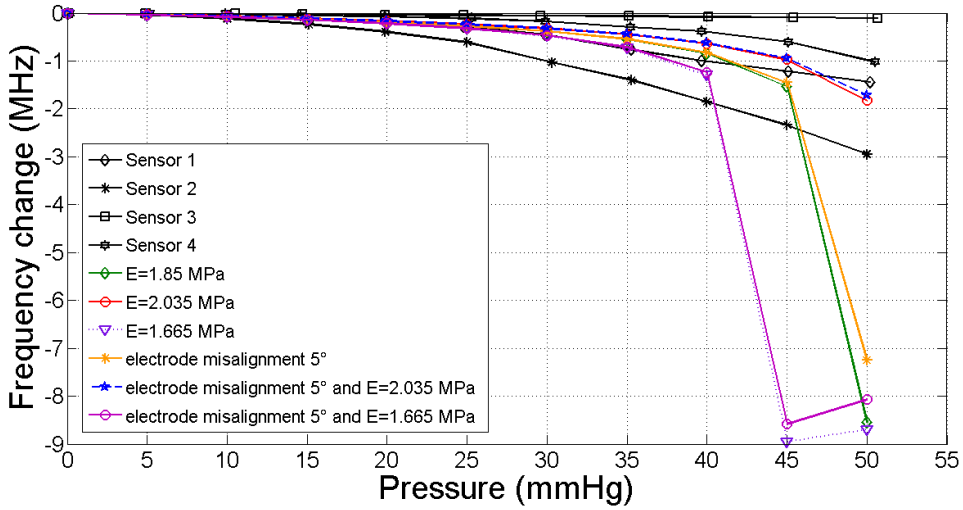

Figure 10.7: *Measured results with constructed sensors of the first design and modified simulations results*

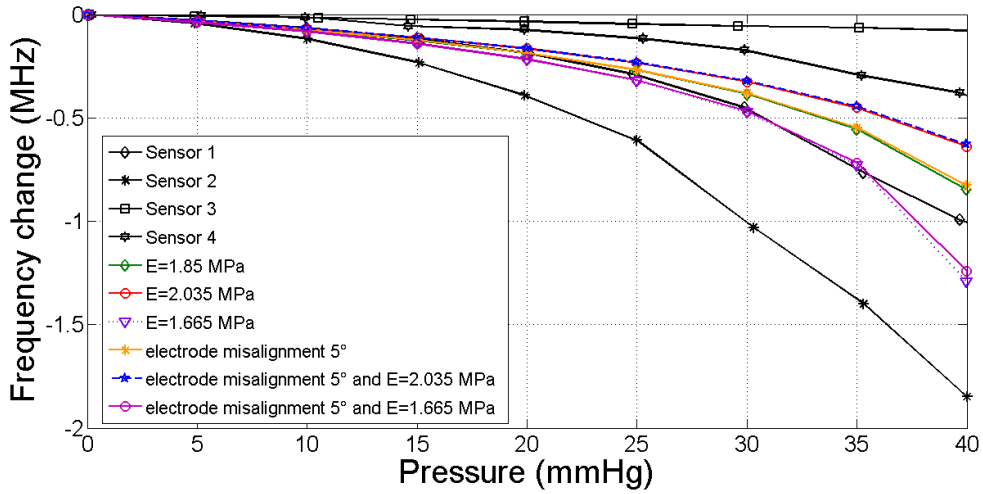

Figure 10.8: *Measured results with constructed sensors of the first design and modified simulations results without the large drops in frequency*

In the Figure 10.9 a comparison between the model results and the second constructed sensors results is presented. In this model, there were not found large drops of frequency as in the model of the first design. In this model it was possible to add more elements to the mesh. Consequently it is possible that the mesh quality is higher in this model than in the model of the first design. However, inverted mesh warnings were got in this simulation for the last results. This could be due to the large deformation of the membrane. For example, Figure 10.10 different simulation results with different Young's modulus values and with misalignment of the electrode are shown. It can be seen that a large drop of frequency is found in the last results of the simulation with Young's modulus value of 1.665 MPa. It is known that with a lower Young's modulus value the deformation of the membrane is higher. Thus, the large drop in frequency could be explained with the mesh quality limitation of the moving mesh feature at large deformation as mentioned before. The odd result in the model can be also explained as before, when the deflection of the membrane is greater that the distance of separation between the membrane electrode and PCB electrodes, the membrane electrode cross the electrodes in the PCB. Furthermore, in these results it can be observed that the misalignment of the electrode has a greater impact in the simulation results than in the model results of the first design.

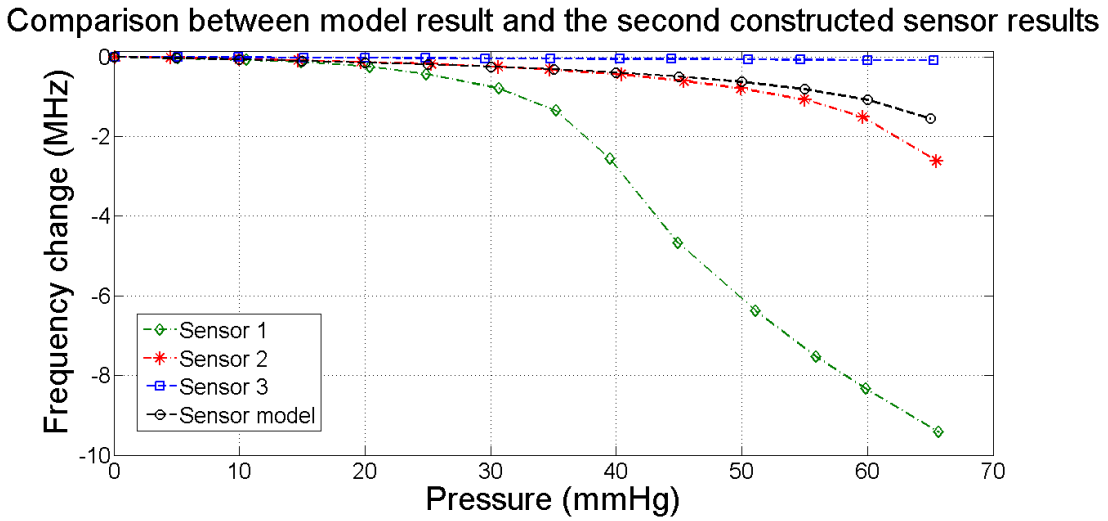

Figure 10.9: *Comparison between the measured results of the second sensor design and the results of the 3D model*

Finally, the Figure 10.11 shows the measurement results with the constructed sensors of the second design and the modified simulation results. The removed DC level in the simulation results is 71.478 MHz.

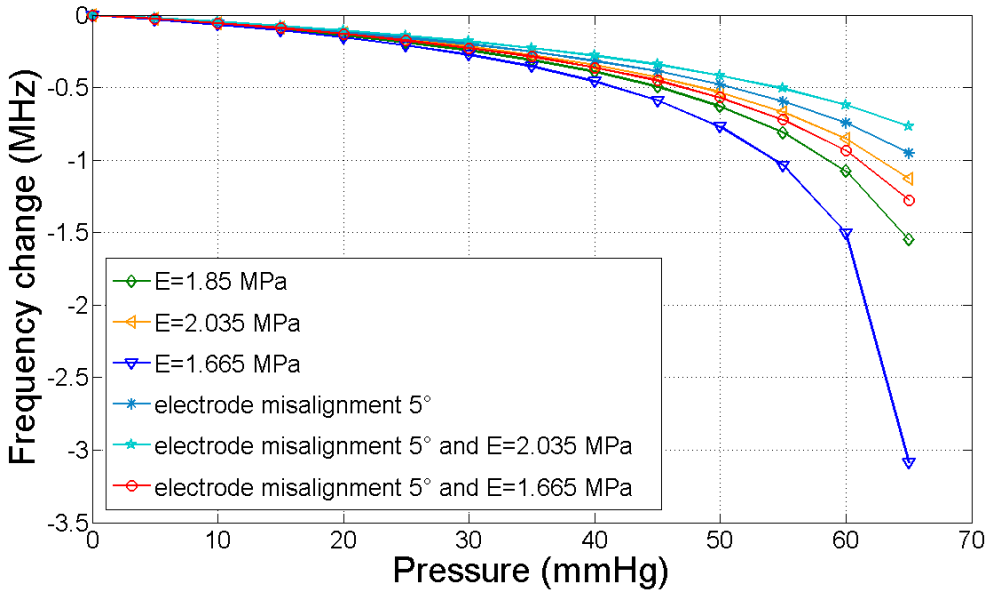

Figure 10.10: *Different simulation results with different Young's modulus values and with misalignment of the electrode*

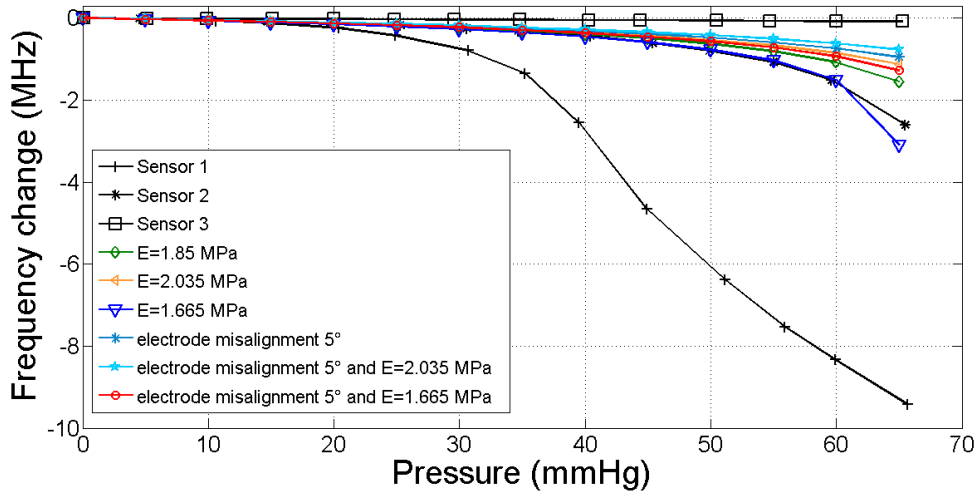

Figure 10.11: *Measured results with constructed sensors of the second design and modified simulations results*

The Figure 10.12 shows the comparison between the results of the constructed sensor of the third design and the two-dimensional model results. The model was constructed to study the behavior of the bossed membrane. It is important to mention that it was not possible to find the mechanical properties of the transparency film, ie. Young's modulus and Poisson's ratio. These values were estimated to be the same as structural steel, Young's modulus 200 GPa and Poisson's ratio 0.33.

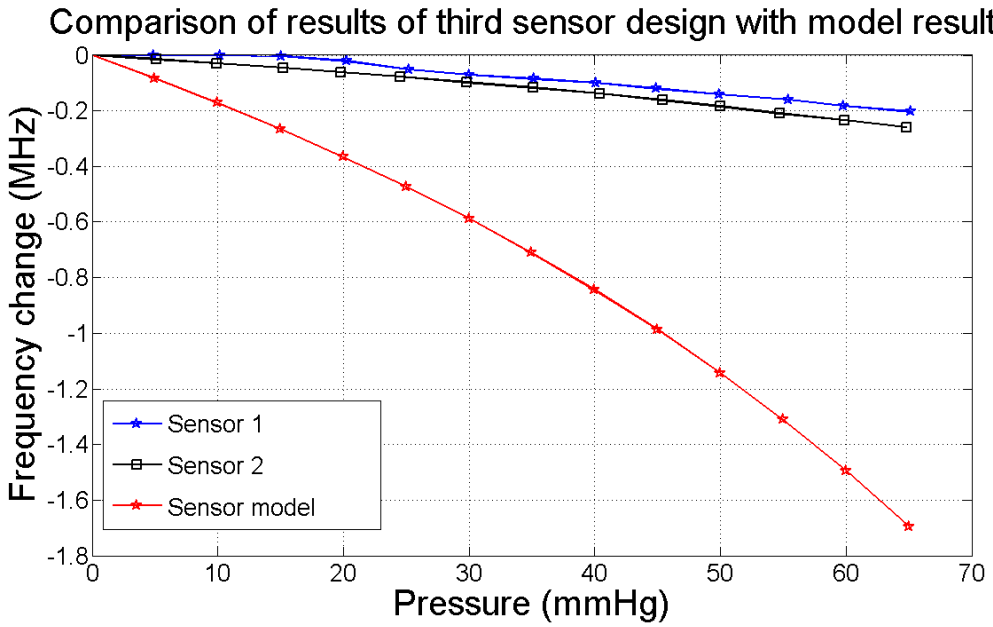

Figure 10.12: *Comparison between the measured results of third sensor design and model*

The results between the model and the measured results differ. The reason for this could be that the capacitance values of the model were calculated using the equation of the parallel plate capacitor and in this equation is assumed that the electrodes move parallel to each other. In the model the membrane is bending and thus the electrode in the membrane is not moving parallel to the PCB electrodes. Also, another reason for the great difference between the model and the measured results is that in the prototypes the spacers are moving and in the model these do not show any displacement.

11. CONCLUSION

This work started with an investigation in types and applications of pressure garments. It was found that pressure is used for the treatment of hypertrophic scars, wounds, venous insufficiency, lymphoedema and other illnesses. Next, it was outline the importance of measuring the interface pressure between the pressure garment and the skin to prove the benefits of the pressure treatment, and to control the amount of pressure applied to the skin.

Then, a study of pressure sensors types was presented. It was found that the capacitive pressure sensors offer good properties for biomedical applications. Also, different structures of capacitive pressure sensors are possible, i.e. flat, bossed, sandwich and touch mode design. Further, for the fabrication of MEMS capacitive sensors, it was found that the most common silicon processes used are anisotropic wet etching, anodic bonding and DRIE.

An investigation in commercially available interface pressure sensors was done. It was found that there are several interface pressure sensors available with different operational principles, for example there are electropneumatic, piezoresistive and capacitive interface pressure sensors.

Next, the passive resonance pressure sensor was presented and a comparison between structures and applications of recent works done with these sensors was performed. It was found that these sensors have biomedical applications due to its less invasiveness.

A three-dimensional model of a capacitive pressure sensor was constructed in COMSOL Multiphysics. Many simulations were performed testing different dimensions in order to enhance the behavior of the sensor. However, because the manufacturing of the mold was restricted and the dimensions of the circuit board are fixed, it was not possible to reduce the dimensions of the membrane as desired. However, when the model results were compared with the constructed prototypes, their behavior was similar.

In each of the designs the results of the constructed sensors varied between them. The reason for this is that the sensors were handmade. As mentioned before, the differences in the process of casting can contribute to the differences. In this work the process of casting was not automatized and was subject to many artifacts. For example, the mixing of curing agent and base polymer was made by hand (using

a plastic spoon and a syringe) and the amount of each substance differs in each sample. Another contribution to the artifacts is the difficulty of the removal of all the bubbles that are formed during the mixing of the curing agent and the base polymer and in the placement of the lid used to applied pressure to the mold. In order to avoid the artifacts produced by using a handmade method, other methods such as injection molding, hot embossing and even stereolithography could be used to manufacture the PDMS membrane. Also, by using these methods, the dimensions of the sensor could be reduced.

Other differences in the results of the constructed sensors could be due to differences between the electrodes since the metal layer was cut by hand using scissors. Also, there were some misalignments of the electrode in the membrane. Furthermore, the poor adhesion of the metal layer to the PDMS membrane is another reason for the variation in the results. To overcome this, the metallization of the membrane could be performed by other technique, such as electroplating or treatment of the PDMS membrane by plasma oxidation.

To prove that the differences between the constructed prototypes could be due to differences in mechanical properties and to misalignments of the membrane electrode, simulations with modified values were performed. Modifications of $\pm$ 10% of the Young's modulus value of the PDMS (1.85 MPa) and 5° misalignment of the electrode were set. The results of these simulations proved that the sensitivity of the sensors is greater at smaller values and thus depends on the Young's modulus value. Also, it was found that the misalignment had a greater impact in the results of the model of the second design than in the model of the first design. When these simulation results were compared with the results of the prototypes it was found that the reason for the different sensitivities might be that the Young's modulus is higher or lower than the reported value for PDMS.

In the results of the model at higher pressures there were high changes of capacitive values. One reason for this is that the deflection of the membrane is greater than the distance between the electrodes, thus, the membrane electrode touches or passes the electrodes of the PCB. This, behavior is not understood by the model, and thus the capacitance is not calculated correctly. Another reason for the odd results of the model at higher pressures is the quality of the mesh. With the available computational power it was not possible to use as many elements in the mesh as wanted, thus this compromised the results. Also, the moving mesh feature has limitations when the deformation is large.

Further, the results of the model differ from the results especially at greater pressures where the deflection of the membrane is greater. In the constructed sensors, at these greater pressures the membrane electrode might touch the circuit board. In this case the change in capacitance depends more in the increasing touching area

and not in the decreasing distance between the electrodes.

Even though the results of each design differ from each other, with the development of the model it could be possible to construct a sensor with smaller dimensions and geometries if better process methods are available.

The third design sensor using the transparency film obtained more similar results between the constructed sensors and with these sensors was possible to obtain more linear results. The reason for this is the incorporation of a boss with a thickness that was 11.7 greater than the thickness of the membrane and the use of transparency film, which has an estimated high Young's modulus. Thus, with the boss the deflection of the central part of the membrane is almost the same, consequently the electrode located at the boss moves almost parallel to the circuit board electrodes. Also, the deflection of the membrane is small, thus enhancing the linear behavior. Furthermore, in these sensors the displacement of the membrane contributed to the deflection of the membrane. This could be one of the reasons for the great difference between the model and the measured results, since in the model the spacers are not moving.

Further, the use of transparency film contributes to the similarity in the results. The reason for this is that the stress is greater at the corners than in the center of the membrane and since this was made with transparency film, the mechanical characteristics are equal in each sensor. On the other hand, in the first and second design, the mechanical characteristics of the membrane depend on the process of casting. Even though the Young's modulus of the transparency film is not known, it was inferred that this value is greater than the value of PDMS. Thus, by taking advantage of this and its small thickness (100μm), transparency film can be used for the development of smaller pressure sensors and with the use of a thick boss it is possible to measure small values of pressures.

In the future, the PCB could be enhanced by using a flexible and biocompatible material, such as PDMS. It is known that with the correct treatment of PDMS (plasma oxidation) two PDMS layers can be bonded. Thus, it could be possible to metallize a layer of PDMS with electroplating for example, to construct the coil, and then bond a PDMS layer in the top of it. With this, it could be also possible to use a circular membrane instead of a square membrane.

Finally, in the future the sensor membrane could be made of a material with a high Young's modulus and a boss. Using this and developing a flexible PCB could be possible to reduce the size and enhance the behavior of the sensor. Thus, the sensor could be used to measure small values of pressure between curved surfaces, such as arms or fingers, and pressure garments.

REFERENCES

[1] F. S. Ng-Yip, "Medical clothing a tutorial paper on pressure garments," *International Journal of Clothing Science and Technology*, vol. 5, no. 1, pp. 17–24, 1993.

[2] S.F.Ng and C. Hui, "Pressure model of elastic fabric for producing pressure garments," *Textile Research Journal*, vol. 71, no. 3, pp. 275–279, 2001.

[3] RAL Institute, "Medical compression hosiery," *Quality Assurance RAL-GZ 387/1*, 2008.

[4] EWMA, "Understanding compression therapy," *EWMA Position Documents*, 2003.

[5] A. Coull and M. C. (Ed.), "Best practice statement compression hosiery," *Wounds UK*.

[6] L. Macintyre and M. Baird, "Pressure garments for use in the treatment of hypertrophic scars–a review of the problems associated with their use," *Burns*, vol. 32, no. 1, pp. 10 – 15, 2006.

[7] R. A. Weiss, N. S. Sadick, M. P. Goldman, and M. A. Weiss, "Post-sclerotherapy compression: Controlled comparative study of duration of compression and its effects on clinical outcome," *Dermatologic surgery*, vol. 25, no. 2, pp. 105–108, 1999.

[8] G. Motykie, J. Caprini, J. Arcelus, J. Reyna, E. Overom, and D. Mokhtee, "Evaluation of therapeutic compression stockings in the treatment of chronic venous insufficiency," *Dermatologic surgery*, vol. 25, no. 2, p. 116, 120.

[9] F. Amsler and W. Blättler, "Compression therapy for occupational leg symptoms and chronic venous disorders - a meta-analysis of randomised controlled trials," *European Journal of Vascular and Endovascular Surgery*, vol. 35, no. 3, pp. 366 – 372, 2008.

[10] R. Liu, Y. L. Kwok, Y. Li, T. T. Lao, and X. Zhang, "Quantitative assessment of relationship between pressure performances and material mechanical properties of medical graduated compression stockings," *Journal of Applied Polymer Science*, vol. 104, no. 1, p. 601, 610.

[11] M. Ferguson-Pell, S. Hagisawa, and D. Bain, "Evaluation of a sensor for low interface pressure applications," *Medical Engineering & Physics*, vol. 22, no. 9, pp. 657 – 663, 2000.

[12] E. V. den Kerckhove, S. Fieuws, P. Massagé, R. Hierner, W. Boeckx, J.-P. Deleuze, J. Laperre, and M. Anthonissen, "Reproducibility of repeated measurements with the kikuhime pressure sensor under pressure garments in burn scar treatment," *Burns*, vol. 33, no. 5, pp. 572 – 578, 2007.

[13] H. P. Giele, K. Liddiard, K. Currie, and F. M. Wood, "Direct measurement of cutaneous pressures generated by pressure garments," *Burns*, vol. 23, no. 2, pp. 137 – 141, 1997.

[14] J. Robertson, J. Hodgson, and J. Druett, "Pressure therapy for hypertrophic scarring preliminary communication," *Journal of the Royal Society of Medicine*, vol. 73, pp. 348 – 354, 1980.

[15] J. M. Zurada, D. Kriegel, and I. C. Davis, "Topical treatments for hypertrophic scars," *Journal of the American Academy of Dermatology*, vol. 55, no. 6, pp. 1024 – 1031, 2006.

[16] H. Partsch, M. Clark, S. Bassez, J.-P. Benigni, F. Becker, V. Blazek, J. Caprini, A. Cornu-Thénard, J. Hafner, M. Flour, M. Jünger, C. Moffatt, and M. Neumann, "Measurement of lower leg compression in vivo: recommendations for the performance of measurements of interface pressure and stiffness," *Dermal Surg*, vol. 32, pp. 244 – 233, 2006.

[17] G. Harman, R. Sommer, and P. Engeler, "Pressure sensors," in *Sensor Technology Handbook* (J. S. Wilson, ed.), pp. 411 – 456, Burlington: Newnes, 2005.

[18] S. Beeby, G. Ensell, M. Kraft, and N. White, *MEMS mechanical sensors*. Microelectromechanical systems series, Artech House, 2004.

[19] A. DeHennis and J. Chae, "Pressure sensors," in *Comprehensive Microsystems* (Y. Gianchandani, O. Tabata, , and H. Zappe, eds.), pp. 101 – 133, Oxford: Elsevier, 2008.

[20] J. W. Garder, *Microsensors principles and applications*. John Wiley Sons Ltd, 1994.

[21] M. J. S. Smith, L. Bowman, and J. D. Meindl, "Analysis, design, and performance of a capacitive pressure sensor ic," *Biomedical Engineering, IEEE Transactions on*, vol. BME-33, no. 2, pp. 163 –174, 1986.

[22] P. M. Elwenspoek and R. Wiegerink, *Mechanical microsensors*. Microtechnology and MEMS, ISSN 1615-8326, Berlin, Germany: Springer Verlag, 2001.

[23] R. Puers, "Capacitive sensors: When and how to use them," *Sensors and Actuators A: Physical*, vol. 37-38, pp. 93 – 105, 1993. Proceedings of Eurosensors VI.

[24] Y. Shkel and N. Ferrier, "Electrostriction enhancement of solid-state capacitance sensing," *Mechatronics, IEEE/ASME Transactions on*, vol. 8, no. 3, pp. 318 –325, 2003.

[25] A. Ettouhami, N. Zahid, and M. Elbelkacemi, "A novel capacitive pressure sensor structure with high sensitivity and quasi-linear response," *Comptes Rendus Mecanique*, vol. 332, no. 2, pp. 141 – 146, 2004.

[26] M.-X. Zhou, Q.-A. Huang, M. Qin, and W. Zhou, "A novel capacitive pressure sensor based on sandwich structures," *Microelectromechanical Systems, Journal of*, vol. 14, no. 6, pp. 1272 – 1282, 2005.

[27] C.-C. Chiang, C.-C. K. Lin, and M.-S. Ju, "An implantable capacitive pressure sensor for biomedical applications," *Sensors and Actuators A: Physical*, vol. 134, no. 2, pp. 382 – 388, 2007.

[28] M.-X. Zhou, Q.-A. Huang, and M. Qin, "Modeling, design and fabrication of a triple-layered capacitive pressure sensor," *Sensors and Actuators A: Physical*, vol. 117, no. 1, pp. 71 – 81, 2005.

[29] W. H. Ko and Q. Wang, "Touch mode capacitive pressure sensors," *Sensors and Actuators A: Physical*, vol. 75, no. 3, pp. 242 – 251, 1999.

[30] Y. Satoshi, S. Takanao, N. Oki, N. Hitoshi, and S. Masahiro, "Touch mode capacitive pressure sensor," *Fujikura Technical Review*, 2003.

[31] T. Pedersen, G. Fragiacomo, O. Hansen, and E. Thomsen, "Highly sensitive micromachined capacitive pressure sensor with reduced hysteresis and low parasitic capacitance," *Sensors and Actuators A: Physical*, vol. 154, no. 1, pp. 35 – 41, 2009.

[32] S. D. Senturia, *Microsystem Design*. United States of America: Springer Science+Business Media, 2001.

[33] G. J. W, "Microsensors principles and applications," 1994.

[34] P. R. Selvaganapathy, "Polymers," in *Comprehensive Microsystems* (Y. Gianchandani, O. Tabata, , and H. Zappe, eds.), pp. 75 – 105, Oxford: Elsevier, 2008.

[35] Y. Lee and K. Wise, "A batch-fabricated silicon capacitive pressure transducer with low temperature sensitivity," *Electron Devices, IEEE Transactions on*, vol. 29, pp. 42 – 48, jan 1982.

[36] F. Schneider, J. Draheim, R. Kamberger, and U. Wallrabe, "Process and material properties of polydimethylsiloxane (pdms) for optical mems," *Sensors and Actuators A: Physical*, vol. 151, no. 2, pp. 95 – 99, 2009.

[37] J. E. Mark, "Polymer data handbook, 2nd ed," *Journal of the American Chemical Society*, vol. 131, no. 44, p. 16330, 2009.

[38] T. K. Kim, J. K. Kim, and O. C. Jeong, "Measurement of nonlinear mechanical properties of pdms elastomer," *Microelectronic Engineering*, vol. In Press, Corrected Proof, pp. –, 2011.

[39] C. Liu, "Recent developments in polymer mems," *Advanced Materials*, vol. 19, no. 22, pp. 3783–3790, 2007.

[40] J. D. Williams and W. Wang, "Study on the postbaking process and the effects on uv lithography of high aspect ratio su-8 microstructures," *Journal of Microlithography Microfabrication and Microsystems*, vol. 3, no. 4, p. 563, 2004.

[41] C. H. Lai and C. W. Li-Tsang, "Validation of the pliance x system in measuring interface pressure generated by pressure garment," *Burns*, vol. 35, no. 6, pp. 845 – 851, 2009.

[42] D. E. Gyi, J. M. Porter, and N. K. Robertson, "Seat pressure measurement technologies: considerations for their evaluation," *Applied Ergonomics*, vol. 29, no. 2, pp. 85 – 91, 1998.

[43] J. C. Robertson, J. Shah, H. Amos, J. E. Druett, and J. Gisby, "An interface pressure sensor for routine clinical use," *Engineering in Medicine 1971-1988*, vol. 9, no. 9, pp. 151–156, 1980.

[44] W. Blätter, B. Uhl, and J. F. Bringer, "Determinants of pressure exerted by medical compression stockings," *Schattauer GmbH*, vol. 36, pp. 237 – 244, 2007.

[45] I. Gaied, S. Drapier, and B. Lun, "Experimental assessment and analytical 2d predictions of the stocking pressures induced on a model leg by medical compressive stockings," *Journal of Biomechanics*, vol. 39, no. 16, pp. 3017 – 3025, 2006.

[46] G. Mosti, "The importance of measuring the sub bandage pressure and the presentation of a new measuring device," *Traduzione Acta Vulnologica.*

[47] P.-J. Chen, S. Saati, R. Varma, M. Humayun, and Y.-C. Tai, "Wireless intraocular pressure sensing using microfabricated minimally invasive flexible-coiled lc sensor implant," *Microelectromechanical Systems, Journal of*, vol. 19, no. 4, pp. 721 –734, 2010.

[48] C. C. Collins, "Miniature passive pressure transensor for implanting in the eye," *Biomedical Engineering, IEEE Transactions on*, vol. BME-14, no. 2, pp. 74 –83, 1967.

[49] T. J. C., "High eye pressure and glaucoma." http://www.glaucoma.org/gleams/high-eye-pressure-and-glaucoma.php, May 2011.

[50] M. Fonseca, M. G. Allen, J. Kroh, and J. White, "Flexible wireless passive pressure sensor for biomedical applications," *Actuators and Microsystems Workshop*, pp. 37 – 42, 2006.

[51] M. Fonseca, J. M. English, M. von Arx, and M. B. Allen, ". wireless micromachined ceramic pressure sensor for high-temperature applications," *Journal of microelectromechanical systems*, vol. 11, no. 4, pp. 337 – 343, 2002.

[52] A. Baldi, W. Choi, and B. Ziaie, "A self-resonant frequency-modulated micromachined passive pressure transensor," *Sensors Journal, IEEE*, vol. 3, no. 6, pp. 728 – 733, 2003.

[53] T. Salpavaara, J. Verho, P. Kumpulainen, and J. Lekkala, "Wireless interrogation techniques for sensors utilizing inductively coupled resonance circuits," *Procedia Engineering*, vol. 5, pp. 216 – 219, 2010. Eurosensor XXIV Conference, Eurosensor XXIV Conference.

[54] M. Sadd, *Elasticity: theory, applications, and numerics*. Elsevier/AP, 2009.

A. APPENDIX

A.1 Phase dip technique

Phase dip technique is commonly used to interrogate passive resonance sensors. Commonly, a passive resonance sensors consists of a parallel inductor and capacitor. Then, it is possible to detect the resonance frequency by coupling an inductor to the LC circuit by the phase dip technique. This technique detects the dip in the phase of the equivalent impedance of the LC circuit [19]. Thus, performing a frequency scan and detecting this phase dip it is possible to detect the resonance frequency of the sensor. Furthermore, in passive pressure sensors when a pressure is applied the resonance frequency is modified due to changes in its capacitance or inductance elements. Measuring the change in the resonance frequency the pressure applied to the sensor can be determined [47].

The resonant frequency of a LC circuit is [47]:

$$f_s = \frac{1}{2\pi}\sqrt{\frac{1}{L_s C_s} - \frac{R_s^2}{L_s^2}} \cong \frac{1}{2\pi\sqrt{L_s C_s}} \text{ if } R_s^2 \ll \frac{L_s}{C_s} \tag{A.1}$$

Where L_s, C_s and R_s are the inductance, capacitance and resistance of the sensor respectively. When an external coil forms an inductive coupling link with the sensor, the equivalent impedance is determined as follows:

$$Z_{eq} = \frac{V}{I} = j2\pi f L_r \left[1 + k^2 \frac{\left(\frac{f}{f_s}\right)^2}{1 - \left(\frac{f}{f_s}\right)^2 + \frac{1}{Q_s} j \frac{f}{f_s}}\right] \tag{A.2}$$

$$Q_s = \frac{\omega_f L_s}{R_s} \tag{A.3}$$

$$k = \frac{L_m}{\sqrt{L_r L_s}} \tag{A.4}$$

where L_m is the mutual inductance and L_r is the reading inductance.

At resonance, the equivalent impedance becomes

$$Z_{eq} = j2\pi f_s L_s \left(1 + jk^2 Q_s\right)) \tag{A.5}$$

With a phase dip of

$$\Delta_\phi \cong \arctan\left(k^2 Q_s\right) \tag{A.6}$$

Thus, detecting the phase-dip the resonant frequency of the sensors can be measured.

B. APPENDIX

B.1 Electrostatics physics interface

According to the documentation of COMSOL Multiphysics, electrostatics physics interface uses the Poisson's equation:

$$-\nabla \cdot (\epsilon_0 \epsilon_r \nabla V) = \rho \tag{B.1}$$

where ∇ is the divergence operator, V is the electric potential, ϵ_0 and ϵ_r are the vacuum and relative permittivity, respectively, and ρ is the space charge density.

Further, the electric field $\mathbf{E}$ is equal to

$$\mathbf{E} = -\nabla V \tag{B.2}$$

to relate the electric displacement $\mathbf{D}$ and the electric field $\mathbf{E}$ with the properties of the medium it is use

$$\mathbf{D} = \epsilon_0 \epsilon_r \mathbf{E} \tag{B.3}$$

The capacitance in calculated in COMSOL Multiphysics as follows:

$$C = \frac{2}{U^2} \int_{\Omega_d} W_e d\Omega_d \tag{B.4}$$

U is the potential difference between the plates or electrodes, W_e is the electric energy density and Ω_d is the gap between the electrodes.

C. APPENDIX

C.1 Solid mechanics interface theory

When a body is deformed the deformation can be quantified by calculating the displacements of materials points in the deformed body [54]. The strain tensor relates the displacement field at all the points with the deformation of the body [54]. Normal strain and shear strain describes small deformation in a body, these equations are shown here

$$\begin{aligned} \epsilon_x &= \frac{\partial u_x}{\partial x}, \quad \gamma_{xy} = \frac{\partial u_x}{\partial y} + \frac{\partial u_y}{\partial x} \\ \epsilon_y &= \frac{\partial u_y}{\partial y}, \quad \gamma_{yz} = \frac{\partial u_y}{\partial z} + \frac{\partial u_z}{\partial y} \\ \epsilon_z &= \frac{\partial u_z}{\partial z}, \quad \gamma_{zx} = \frac{\partial u_z}{\partial x} + \frac{\partial u_x}{\partial z} \end{aligned} \tag{C.1}$$

where u,v,w are the Cartesian components of the displacement vector , ϵ and γ are the normal and shear strain respectively [54].

Normal strain is defined as the change in length per unit length and shear strain is the change in angle between two orthogonal directions [54].

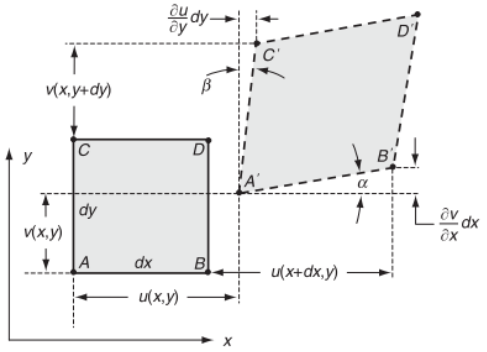

Figure C.1

The relation between strain and displacement can be written in a strain tensor e_{ij}, this is expressed in component form as:

$$\begin{aligned} e_x &= \frac{\partial u}{\partial x}, & e_y &= \frac{\partial v}{\partial y}, & e_z &= \frac{\partial w}{\partial z} \\ e_{xy} &= \frac{1}{2}\left(\frac{\partial u}{\partial y} + \frac{\partial v}{\partial x}\right), & e_{yz} &= \frac{1}{2}\left(\frac{\partial v}{\partial z} + \frac{\partial w}{\partial y}\right), & e_{zx} &= \frac{1}{2}\left(\frac{\partial w}{\partial x} + \frac{\partial u}{\partial z}\right) \end{aligned} \tag{C.2}$$

And also can be expressed in a compact form as:

$$e_x = \frac{1}{2}\left(u_{i,j} + u_{j,i}\right) \tag{C.3}$$

where $u_{i,j}$ is the displacement gradient tensor

$$u_{i,j} = \begin{bmatrix} \frac{\partial u}{\partial x} & \frac{\partial u}{\partial y} & \frac{\partial u}{\partial z} \\ \frac{\partial v}{\partial x} & \frac{\partial v}{\partial y} & \frac{\partial v}{\partial z} \\ \frac{\partial w}{\partial x} & \frac{\partial w}{\partial y} & \frac{\partial w}{\partial z} \end{bmatrix} \tag{C.4}$$

In COMSOL Multiphysics this is expressed in a vector/matrix notation as shown here:

$$\epsilon = \frac{1}{2}\left[\nabla \mathbf{u} + (\nabla \mathbf{u})^{\top}\right] \tag{C.5}$$

where ϵ is the strain matrix, $\nabla \mathbf{u}$ is the displacement gradient matrix and $(\nabla \mathbf{u})^{\top}$ it is the transpose [54].

When an external force is applied to a body, internal forces are induced and are distributed continuously inside the structure [54]. These forces are categorized as body and surface forces. Body forces are the ones which are proportional to the mass of the body and are a reaction to an external agent, for example gravitational-weight forces and inertial forces [54].

Further, the total resultant body force $\mathbf{F}_R$ is defined as the volume integral over the entire body of the body force density $\mathbf{F}(\mathbf{x})$ which is the force per unit volume.

$$\mathbf{F}_R = \iiint_V \mathbf{F}\left(\mathbf{x}\right) dV \tag{C.6}$$

On the other hand, surface forces are the forces that results from the physical contact between the surfaces of different bodies. For example in the next figure a surface force is applied to a body and to study the resultant surface force a surface area called S is created.

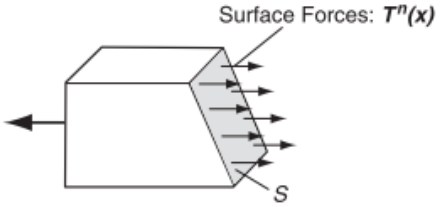

Figure C.2

The resultant surface force over the area S is the integral of the surface force

density function $\mathbf{T}^n(\mathbf{x})$ also called traction vector.

$$\mathbf{F}_s = \iint_S \mathbf{T}^n(\mathbf{x})\, dS \tag{C.7}$$

The stress or traction vector is defined as

$$\mathbf{T}^n(\mathbf{x}, \mathbf{n}) = \lim_{\delta A \to 0} \frac{\delta \mathbf{F}}{\delta A} \tag{C.8}$$

where $\delta\mathbf{F}$ is the surface force acting on a small area δA which has a unit normal vector $\mathbf{n}$ [54].

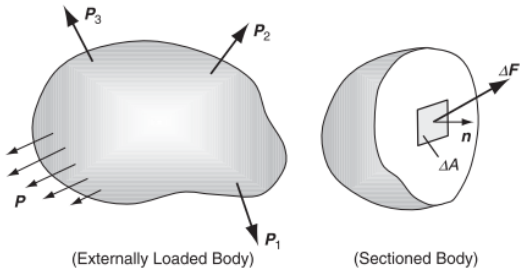

Figure C.3

The relation between the traction vector and stress tensor also called Cauchy stress tensor is

$$\begin{aligned} \mathbf{T}^{\mathbf{n}} = \quad & (\sigma_x n_x + \tau_{yx} n_y + \tau_{zx} n_z)\, \mathbf{e}_1 + \\ & (\tau_{xy} n_x + \sigma_y n_y + \tau_{zy} n_z)\, \mathbf{e}_2 + \\ & (\tau_{xz} n_x + \tau_{yz} n_y + \sigma_z n_z)\, \mathbf{e}_3 \end{aligned} \tag{C.9}$$

where n is the unit vector

$$\mathbf{n} = n_x \mathbf{e}_1 + n_y \mathbf{e}_2 + n_z \mathbf{e}_3 \tag{C.10}$$

n_x, n_y, n_z are the direction cosines
This expression can be written also as

$$T_i^n = \sigma_{ji} n_j \text{ or } \mathbf{T}^{(\mathbf{n})} = \sigma \cdot \mathbf{n} \tag{C.11}$$

In COMSOL Multiphysics $\mathbf{T}^{(n)}$ is represented as $\mathbf{F}_A$

$$\sigma \cdot \mathbf{n} = \mathbf{F}_A \tag{C.12}$$

and with pressure as load type F_A is

$$\mathbf{F}_A = -p\mathbf{n} \tag{C.13}$$

where p is pressure in Pascals Further, when a body is in static equilibrium means that the summation of all the forces and moments is zero [54]. The static equilibrium equation is

$$\sigma_{ij,j} + F_i = 0 \text{ or } \nabla \cdot \boldsymbol{\sigma} + \mathbf{F} = 0 \tag{C.14}$$

Where F_i is the body force density and σ_{ij} is the Cauchy stress tensor which components in matrix format are:

$$\boldsymbol{\sigma} = [\boldsymbol{\sigma}] = \begin{bmatrix} \sigma_x & \tau_{xy} & \tau_{xz} \\ \tau_{yx} & \sigma_y & \tau_{yz} \\ \tau_{zs} & \tau_{zy} & \sigma_z \end{bmatrix} \tag{C.15}$$

Thus, the equilibrium equations in scalar notation are written as:

$$\begin{array}{l} \frac{\partial \sigma_x}{\partial x} + \frac{\partial \tau_{yx}}{\partial y} + \frac{\partial \tau_{zx}}{\partial z} + F_x = 0 \\ \frac{\partial \tau_{xy}}{\partial x} + \frac{\partial \sigma_y}{\partial y} + \frac{\partial \tau_{zy}}{\partial z} + F_y = 0 \\ \frac{\partial \tau_{xz}}{\partial x} + \frac{\partial \tau_{yz}}{\partial y} + \frac{\partial \sigma_z}{\partial z} + F_z = 0 \end{array} \tag{C.16}$$

In COMSOL Multiphysics, equilibrium equations use a vector/matrix notation form

$$\nabla \cdot \boldsymbol{\sigma} + \mathbf{F} = 0 \tag{C.17}$$

Furthermore, a three dimensional relation between stress tensor and strain tensor is

$$\begin{array}{l} \sigma_x = C_{11}e_x + C_{12}e_y + C_{13}e_z + 2C_{14}e_{xy} + 2C_{15}e_{yz} + 2C_{16}e_{zx} \\ \sigma_y = C_{21}e_x + C_{22}e_y + C_{23}e_z + 2C_{24}e_{xy} + 2C_{25}e_{yz} + 2C_{26}e_{zx} \\ \sigma_z = C_{31}e_x + C_{32}e_y + C_{33}e_z + 2C_{34}e_{xy} + 2C_{35}e_{yz} + 2C_{36}e_{zx} \\ \tau_{xy} = C_{41}e_x + C_{42}e_y + C_{43}e_z + 2C_{44}e_{xy} + 2C_{45}e_{yz} + 2C_{46}e_{zx} \\ \tau_{yz} = C_{51}e_x + C_{52}e_y + C_{53}e_z + 2C_{54}e_{xy} + 2C_{55}e_{yz} + 2C_{56}e_{zx} \\ \tau_{zx} = C_{61}e_x + C_{62}e_y + C_{63}e_z + 2C_{64}e_{xy} + 2C_{65}e_{yz} + 2C_{66}e_{zx} \end{array} \tag{C.18}$$

Or can be written as

$$\sigma_{ij} = C_{ijkl}e_{kl} \tag{C.19}$$

Where C_{ijkl} is the stiffness tensor which contains all the materials parameters needed to describe the material [54]. Taking into account that temperature changes deform the body, the total strain is constituted of mechanical and thermal effects as shown below

$$e_{ij} = e_{ij}^{(M)} + e_{ij}^{(T)} \tag{C.20}$$

The thermal strain can be written as

$$e_{ij}^{(T)} = \alpha_{ij} \left(T - T_0\right) \tag{C.21}$$

where T_0 is the reference or initial temperature, T is the final temperature and α_{ij} is the coefficient of thermal expansion tensor.

In COMSOL Multiphysics the total stress is described as

$$\mathbf{s} = \mathbf{s}_0 + \mathbf{C} : (\epsilon - \epsilon_0 - \alpha\theta) \tag{C.22}$$

where $\mathbf{s}$ is equal to $\boldsymbol{\sigma}$, $\mathbf{s}_0$ and ϵ_0 are the initial stresses and strains, θ is the change in temperature $\theta = (T - T_0)$ and $\mathbf{C} : \epsilon$ is the same as $C_{ijkl}\epsilon_{kl}$.